

# Tropical tropospheric ozone and carbon monoxide distributions: characteristics, origins and control factors, as seen by IAGOS and IASI

Maria Tsivlidou<sup>1</sup>, Bastien Sauvage<sup>1</sup>, Yasmine Bennouna<sup>1</sup>, Romain Blot<sup>1</sup>, Damien Boulanger<sup>2</sup>, Hannah Clark<sup>3</sup>, Eric Le Flochmoën<sup>1</sup>, Philippe Nédélec<sup>1</sup>, Valérie Thouret<sup>1</sup>, Pawel Wolff<sup>2</sup>, and Brice Barret<sup>1</sup>

<sup>1</sup>Laboratoire d'Aérologie (LAERO), Université Toulouse III – Paul Sabatier, CNRS, Toulouse, France

<sup>2</sup>Observatoire Midi-Pyrénées (OMP-SEDOO), Université Toulouse III - Paul Sabatier, CNRS, Toulouse, France

<sup>3</sup>IAGOS-AISBL, 98 Rue du Trône, Brussels, Belgium

**Correspondence:** Maria Tsivlidou (mtsivl@gmail.com)

**Abstract.** The characteristics and seasonal variability of the tropical tropospheric distributions of ozone (O<sub>3</sub>) and carbon monoxide (CO) were analysed based on in situ measurements provided by the In-service Aircraft for a Global Observing System (IAGOS) program since 1994 and 2002 respectively, combined with observations from the Infrared Atmospheric Sounding (IASI) instrument on board the Met-op A satellite since 2008. The SOFT-IO model, which couples back trajectories with CO emissions inventories, was used to explore the origins and sources of the tropical CO observed by IAGOS. The highest tropical O<sub>3</sub> and CO maxima occur over Northern ~~Hemisphere (NH)~~Tropical (NT) Africa in the low troposphere (LT) ~~(80 ppb; surface to 750 hPa) during the dry season (75 ppb of O<sub>3</sub> at 2.5 km~~ and 850 ppb ~~respectively at 2.5 of CO at 0.3 km over Lagos) during the dry season (in January).~~ Despite the active local fires, local anthropogenic (AN) emissions (~~60-58 %~~) are dominant for the CO, ~~and consequently the O<sub>3</sub> maxima.~~ The importance of the local AN emissions are highlighted over Central Africa, as they cause a persistent polluted surface layer during the transition seasons (40 % in October and 86 % in April). The second highest O<sub>3</sub> and CO maxima are observed over Asia. Local or regional Asian AN emissions cause the CO maximum in the LT ~~(at 0.5 km) in January, and the O<sub>3</sub> maximum in the free troposphere (at above 6 km) in the post-monsoon season (April).~~ South China is the only Asian site where O<sub>3</sub> peaks in the LT (75 ppb at 2.5 km), due to local fires (30 %) in addition to the local (52 %) and regional (15 %) AN emissions. The highest amount of transported CO ~~in the tropics~~ originates from Africa. The main transport pathway is from the dry-season African regions towards the wet-season ones. Contributions from ~~the NH Northern Hemisphere~~ Africa are found over Arabia and Eastern Africa (up to 70 %) ~~, and India (40 % in the mid (MT) and 60% in the upper (UT) troposphere) during the dry season . Transport towards NH South America is found and over South America all year long , with significant contributions in the MT and UT (30-40 in the mid (MT; 750-300 hPa) and upper troposphere (UT; 300-200 hPa)(18-38 % over Caracas on annual basis).~~ In contrast, the impact of the Asian emissions in the LT and MT is limited on a local or regional scale. Export of polluted Asian air masses is important in the UT during the Asian summer monsoon and post-monsoon seasons, when convection is active. The AN Asian contributions are mostly found over Arabia and Eastern Africa (up to 80 %) during the Asian summer monsoon. During the post-monsoon, CO impacted by the Indonesian

fires (resp. SouthEast Asian AN emissions) are transported towards Eastern Africa (64% and 16%) due to the Tropical Easterly Jet. The lowest O<sub>3</sub> and CO levels are observed over South America, due to less strong local emissions in comparison to Asia and Africa. The only important CO and O<sub>3</sub> enhancement is observed in the MT during the local fires (October), when O<sub>3</sub> and precursors impacted by the local AN and fire emissions are trapped in an anticyclone and transported towards ~~South~~ Southern Africa (5–10 ppb from ~~SH and NH~~ Northern and Southern Hemisphere South America respectively).

*Copyright statement.* TEXT

## 1 Introduction

30 Tropospheric ozone (O<sub>3</sub>) and carbon monoxide (CO) are key components in the atmosphere. O<sub>3</sub> has a significant impact on human health close to the surface (Curtis et al., 2006; Jerrett et al., 2009) and on climate by being a powerful greenhouse gas (Gauss et al., 2003; IPCC, 2021). O<sub>3</sub> is a secondary pollutant produced by photochemical oxidation of precursors such as CO and volatile organic compounds (VOCs) in the presence of nitrogen oxides (NO<sub>x</sub>) (Logan et al., 1981). Its distribution is controlled by: stratospheric transport (Stevenson et al., 2013); transport processes at intercontinental and hemispheric scale  
35 (Wild et al., 2004); emissions of precursors (natural and anthropogenic) and destruction processes (photochemical and depositional) (Monks et al., 2015). Due to its longer lifetime, CO is considered a powerful pollution tracer of combustion products at a hemispheric level (~~Edwards et al., 2006~~) (Logan et al., 1981). CO impacts the oxidation capacity of the atmosphere by being the major sink of OH radicals in non polluted atmosphere (Lelieveld et al., 2016), and the climate by producing greenhouse gases, such as CO<sub>2</sub> and O<sub>3</sub>, during its oxidation (Myhre et al., 2013). ~~The primary (resp. secondary) sources of CO include~~  
40 ~~anthropogenic~~ CO is primarily emitted by incomplete combustion, thus by anthropogenic (AN) and biomass burning emissions (resp. (BB) sources (Galanter et al., 2000; Granier et al., 2011), with contributions between 450–600 and 350–600 Tg CO yr<sup>-1</sup> respectively (Lamarque et al., 2010; van der Werf et al., 2006). Its secondary sources include oxidation of VOCs and methane (450–1200 and 600– 1000 Tg CO y<sup>-1</sup> resp.; (Stein et al., 2014)).

Recent studies (Gaudel et al., 2018, 2020; Zhang et al., 2016) have shown increasing tropospheric O<sub>3</sub> burden in the second  
45 half of the 20th century mostly due to increase of precursors in the tropical regions. ~~However,~~ Based on aircraft observations, Bourgeois et al. (2020) recently presented a global-scale distribution of O<sub>3</sub> in the remote troposphere. However, uncertainties still remain in the global O<sub>3</sub> distribution and sources of precursors ~~remain uncertain due to inadequate~~ due to paucity of observations in the ~~remote~~ free troposphere, especially over developing countries in the tropics (Gaudel et al., 2018; Tarasick et al., 2019).

50 The tropical region is of particular interest regarding tropospheric O<sub>3</sub> and CO. It combines: i) intense photochemistry due to high UV radiation and humidity, ii) large active natural sources of CO and other O<sub>3</sub> precursors through ~~biomass burning~~ BB (Ziemke et al., 2009), biogenic (Aghedo et al., 2007) and lightning emissions (Sauvage et al., 2007b, c), iii) increasing ~~anthropogenic emission~~ AN due to rapid industrialisation (Granier et al., 2011; Duncan et al., 2016), iv) large ozone net pro-

duction potential because deep convection can transport surface emissions to higher altitudes, where their lifetime is increased  
55 due to lack of surface deposition and dilution with unpolluted background (Pickering et al., 1995) and v) dynamic processes  
capable of redistributing chemical species in a regional and global scale (Zhang et al., 2016). Thus, the tropics are a region  
where O<sub>3</sub> production is favoured.

Satellite observations from the OMI and MLS sensors (Ziemke et al., 2019) and simulations from the GEOS-Chem chemical  
transport model (Zhang et al., 2016, 2021) display the highest O<sub>3</sub> burden increase in the tropical region - mostly over India,  
60 East Asia and SouthEast Asia. Most studies tend to confirm an increase of O<sub>3</sub> in the tropics but they are mostly based on  
model simulations, sparse ground observations or satellite data with little consistency, and it is not clear what can cause such  
~~O<sub>3</sub> an~~ increase. Indeed, ~~the~~ trends are attributed to different factors such as ~~biomass burning~~ ~~BB~~ (Heue et al., 2016), dynamics  
(Lu et al., 2019; Thompson et al., 2021) ~~or anthropogenic~~, ~~or AN~~ (Zhang et al., 2016; Gaudel et al., 2020). Thus, further  
investigation based on *in situ* observations is required in order to better constraint models ~~and~~, ~~validate~~ satellite retrievals, and  
65 reduce the uncertainties in the quantification of O<sub>3</sub> and CO trends and source attribution over the tropics.

Measurements of tropical O<sub>3</sub> and CO are available by satellite observations, but they have a coarse vertical resolution  
(e.g. Barret et al., 2008; Thompson et al., 2001). ~~Several~~ ~~On short time scales, several~~ field campaigns have been carried  
out in the tropics. ~~However, they provide sparse measurements in terms of temporal and spatial coverage. The~~, ~~yielding~~  
~~measurements of various species over Africa (from TROPOZ 1987 to CAFE-Africa), Asia (from INDOEX to EMerge-Asia),~~  
70 ~~South America (Cite-1/2/3, TROCCiNOX) and the tropical Pacific (from PEM-WEST-A/B to CAST/CONTRAST/ATTREX~~  
~~and Atom). These campaigns have provided invaluable insights on the atmospheric chemistry and dynamics of the tropical~~  
~~region. On greater timescales, the~~ Southern Hemisphere ADditional OZone Sounding (SHADOZ) program (Thompson et al.,  
2003a) provides long-term O<sub>3</sub> observations over the tropics using ozonesondes since 1998. ~~Even though these measurements~~  
~~These measurements have~~ offered a better understanding on ~~vertical distribution~~ ~~the vertical distribution and trends~~ of tropical  
75 O<sub>3</sub>, ~~they are mostly limited to remote observing sites such as Ascension and Reunion island, and they under-represent the~~  
~~tropical upper troposphere. In addition, it is difficult to provide additional constraints regarding the relation between O<sub>3</sub> and~~  
~~CO in the tropics, due to a lack of simultaneous CO in-situ observations.~~

~~The~~ (e.g. Thompson et al., 2021).

~~In a complementary way to these datasets, the~~ IAGOS (In-service Aircraft for a Global Observing System; ~~Marengo et al., 1998; Petzold~~  
80 ~~(Thouret et al., 2022)~~ ~~(Marengo et al., 1998; Petzold et al., 2015; Thouret et al., 2022)~~ program has provided ~~continuous and~~  
~~consistent O<sub>3</sub> (Thouret et al., 1998; Blot et al., 2021) and CO (Nédélec et al., 2015) observations and CO measurements~~ over  
the tropics ~~for the last 26 and 18 years respectively. It measures vertical profiles over remote (e.g. Madras) and megacities (e.g.~~  
~~Lagos, Hong Kong), since 1994 and 2002 respectively. Using equipped commercial aircraft, IAGOS samples vertical profiles~~  
~~at take off and landing,~~ along with the lower part of the upper tropical troposphere ~~at cruise altitude between 300 and 185 hPa~~  
85 ~~(U<sub>T,cruise</sub>)~~. Previous studies have documented the tropical composition over Africa (Sauvage et al., 2005, 2007a, d; Lannuque  
et al., 2021), South America (Yamasoe et al., 2015) and South Asia (Sahu et al., 2014; Sheel et al., 2014) ~~using IAGOS data~~.  
However, they are focused on specific regions of the tropics and have limited temporal coverage, especially for CO as fewer

measurements were available at this time. Thus, the O<sub>3</sub> and CO distributions and their interlocking in the entire tropics are still not well documented.

90 The SOFT-IO model (Sauvage et al., 2017) has been developed to supplement the analysis of the IAGOS dataset by estimating ~~anthropogenic (AN) and biomass burning (BB)~~ AN and BB contributions to the observed CO measurements. These measurements, along with the SOFT-IO output allow us to trace the CO origin ~~and establish connections with O<sub>3</sub> origin~~ over the tropics. Further, global distributions provided by Infrared Atmospheric Sounding Interferometer (IASI)-Software for a Fast Retrieval of IASI Data (SOFRID) (Barret et al., 2011; De Wachter et al., 2012) retrievals since 2008 complement the  
95 O<sub>3</sub> and CO distributions provided by IAGOS. They allow us to understand the spatial extent of pollution plumes, and explore intercontinental transport patterns.

In this article we take advantage of the unique IAGOS database to (i) document the characteristics and seasonal variability of these two atmospheric species over the whole tropical band for the last decade ~~for the first time~~, (ii) explore the origin of the observed CO anomalies, (iii) investigate transport processes driving the CO and O<sub>3</sub> distribution in the tropics.

100 The observational (IAGOS and IASI) and model based (SOFT-IO) datasets, and methodology are introduced in Sect. 2. In Section 3, the IAGOS observations are analysed to document O<sub>3</sub>/CO vertical profiles, along with the ~~UT~~ upper tropospheric composition over the tropics. In addition, the sources of observed CO are explored with SOFT-IO.

## 2 Data and Methods

### 2.1 IAGOS observations

105 The Research Infrastructure IAGOS (Petzold et al., 2015; Thouret et al., 2022) provides *in situ* measurements of trace gases (O<sub>3</sub>, CO, water vapour, NO<sub>y</sub> between 2001 and 2005 (e.g. Gressent et al., 2014), and more recently NO<sub>x</sub>, CH<sub>4</sub>, CO<sub>2</sub> and cloud particles, see <https://www.iagos.org/iagos-data/>) and meteorological parameters (temperature and winds), using equipped commercial aircraft. Full description of the instruments can be found in Nédélec et al. (2015). O<sub>3</sub> (resp. CO) is measured using a dual-beam ultraviolet absorption monitor (infrared analyser) with an ~~accuracy of overall uncertainty of ±2 ppb (resp. 5 ppb); a~~  
110 ~~precision of ppbv ±2 % (resp. ±5 ppbv ±5 %)~~ and a time resolution of 4 (resp. 30) seconds (~~Thouret et al., 1998; Nedelec et al., 2003~~)  
(Nédélec et al., 2015). IAGOS measures vertical profiles during ascend and descend phases, and the ~~upper troposphere (between~~  
~~9 and 12 km; 300–185 hPa)~~ UT<sub>cruise</sub> during cruise phases. Considering the aircraft speed (7–8 m s<sup>-1</sup> during ascent/descent; 900 km h<sup>-1</sup> during cruise), the time resolution of the instruments corresponds to a vertical resolution of 30 m (resp. 225 m), and a horizontal resolution of 1 km (resp. 7.5 km) for O<sub>3</sub> (resp. CO).

115 O<sub>3</sub> (resp. CO) observations have been collected since 1994 (resp. 2002) in the frame of the IAGOS Research Infrastructure and its predecessor MOZAIC (Marengo et al., 1998) program, based on the same instrument technologies. Good consistency in the measurements between the two programs (hereafter referred to as IAGOS) (Nédélec et al., 2015; Blot et al., 2021) leads to IAGOS temporal coverage of 26 (resp. almost 20) years for O<sub>3</sub> (resp. CO), depending on the availability of the flights. IAGOS data provides robust O<sub>3</sub> and CO climatologies, allowing studies of long-term trends (e.g. Cohen et al., 2018) along  
120 with validation of chemistry transport models (e.g. Sauvage et al., 2007b; Gressent et al., 2016) and satellite data retrievals

(e.g. De Wachter et al., 2012) on a global scale. To complement the IAGOS observations, we use the potential vorticity (PV) field, which is part of the ancillary data (<https://doi.org/10.25326/3>) from the IAGOS database. The PV is calculated from the European Centre for Medium-Range Weather Forecast's (ECMWF) operational fields (horizontal resolution 1°, time resolution 3 hours), interpolated along IAGOS trajectories.

### 125 2.1.1 Data treatment

The tropical zone can be defined in several ways, such as by meteorological characteristics (e.g. location of the subtropical jets), climatic elements (e.g. precipitation rates) or by the geographical extent. Following the latter way, in the Tropospheric Ozone Assessment Report, Phase II (TOAR-II; <https://igacproject.org/activities/TOAR/TOAR-II>) Ozone and Precursors in the Tropics working group, the tropics are defined between 20° S and 20° N. In our study, we consider the extended area between  
130 25° S and 25° N, in order to investigate interactions of pollution and the transport of air masses between the tropics and the subtropics. ~~IAGOS observations are used to document O<sub>3</sub>/CO vertical profiles and the (lower part of) UT.~~ Only tropospheric measurements are taken into account, by applying a PV filter of 2 PV units (pvu) for each measurement during cruise phase, and for the measurements between 20–25° N/S during ascend/descend. The UT<sub>cruise</sub> climatologies are derived by averaging the cruise data (~~300–185 hPa~~) on a 2 x 2.5° grid, for the period 1994–2020 (resp. 2002–2020) for O<sub>3</sub> (resp. CO). For the same  
135 time periods, the climatologies over the vertical are derived by averaging the data into 10 hPa pressure bins from the surface up to ~~the upper limit of the profile. The upper limit is based on 200 hPa. We also applied~~ a distance criteria of ~~a 300-km radius~~ around the IAGOS observational site, similar to Petetin et al. (2016). This way we reduce uncertainties due to possible horizontal heterogeneity in the measurements, as the aircraft keeps moving in the horizontal plane during ascent and descent. ~~The cut-off radius is set in alignment to a coarser global model resolution, in order to limit the potential heterogeneity inside a~~  
140 ~~single grid box.~~

~~To~~ Table 1 shows the total number of profiles taken into account for this study for each site for the whole IAGOS period. The temporal availability of the measurements differ for each site and cluster, as it depends on the flight schedule of the aircraft (see Figs. S4 and S5). For this reason, to determine a reliable climatological profile, we need to assess the statistical significance of the data. Similar to Logan (1999) and Sauvage et al. (2005), we compute the relative standard error (RSE) of the O<sub>3</sub> (CO) monthly mean, versus the number of flights per month. The RSE is defined as the ~~fraction ratio~~ between the standard error ( $SE = \frac{\sigma}{\sqrt{N}}$ , with  $\sigma$  the square root of the sample variance and  $N$  the number of flights) and the O<sub>3</sub> (CO) monthly mean. The minimum number of flights required for statistical significance corresponds to the number above which  $RSE \leq 10\%$ . We choose RSE less than 10 %, because RSE depends not only on the number of measurements, but also on the O<sub>3</sub> (CO) variability which is high over the tropics (Thompson et al., 2003b). For each site with an adequate number of flights per  
150 month, we consider an individual profile of O<sub>3</sub> (CO). Otherwise, we combine sites in clusters(~~see Table 1~~), in order to increase the amount of data and get significant climatological profiles. Besides, the clusters can be useful for validation of models with a coarse horizontal resolution, because they represent a wider area as resolved by the models, which are not expected to capture small-scale variations in the ozone field (e.g. Emmons et al., 2010). For clustering, the sites should be: i) in relatively

close distance from each other, ii) governed by similar meteorological conditions, and iii) display similar characteristics in the vertical distribution of O<sub>3</sub> (CO) (see Sect. 3.1).

The meteorological conditions in the tropics are peculiar, with different seasonal patterns depending on the region. For instance, in Africa the main seasons are two (dry and wet) with two intermediate seasons passing from wet to dry and vice versa (Sauvage et al., 2005; Lannuque et al., 2021). On the other hand, in Asia the seasons are defined by the Asian monsoon phases: Asian summer monsoon (wet season); Asian winter monsoon (dry season) and post monsoon. Thus, we considered it more appropriate for our analysis to deviate from the classical definition of the seasons, which fits better to studies concerning higher latitudes. Instead, we analyse the O<sub>3</sub>/CO profiles and horizontal distributions ~~over intermediate months of the~~ for months during the peak tropical seasons (January, April, July and October), to highlight seasonal patterns.

## 2.2 SOFT-IO model

The SOFT-IO (SOft attribution using FlexparT and carbon monoxide emission inventories for In-situ Observation database) tool (Sauvage et al., 2017; <http://dx.doi.org/10.25326/2>) has been developed to investigate the origin of the observed IAGOS-CO, by coupling FLEXPART 20-days backward transport simulations with emission inventories. For each point of IAGOS trajectory, SOFT-IO estimates the CO contribution coming from 14 different geographical regions (see Fig. 1), for AN and BB origin separately. We use Community Emissions Data System (CEDS2) AN emissions (McDuffie et al., 2020) and the Global Fire Assimilation System (GFAS) BB emissions (Kaiser et al., 2012) which include fire injection heights, to discriminate sources of CO anomalies over different regions of interest. For the calculations, the AN (resp. BB) emissions are updated on a monthly (resp. daily) basis.

SOFT-IO estimates the contribution to CO anomalies emitted by primary sources during the last 20 days, while it does not calculate the background CO. The background CO can be emitted by primary sources older than 20 days, and by secondary sources such as oxidation of methane and non-methane volatile organic compounds. The meteorological fields are based on 1° x 1° ECMWF analysis and forecast with a time resolution of 6 and 3h respectively.

Several studies (e.g. Cussac et al., 2020; Lannuque et al., 2021; Petetin et al., 2018b) have used SOFT-IO to track back the sources of CO measured by IAGOS. Sauvage et al. (2017) validated SOFT-IO performance against IAGOS CO observations for several regions and tropospheric levels. ~~Results show As detailed in their study, SOFT-IO 's capability to detect more than uncertainties and biases are mostly due to uncertainties in emission inventories, and to a lesser extent to uncertainties concerning the meteorological fields and FLEXPART transport parameterizations (turbulence, convection). Their results show that SOFT-IO can simulate~~ 95 % of the observed ~~CO anomalies over most of the regions~~ number of anomalies, without any strong dependence on altitude or region of the CO plume. SOFT-IO captures the intensity of CO anomalies with bias lower than ~~10-15-10-15~~ ppb for most of the regions and tropospheric levels. The bias is higher in extreme pollution events and might be related to uncertainties in the emissions inventories.

In our study, CO anomalies are defined as the positive difference between the observed and the background CO mixing ratio. Background CO mixing ratio represents a reference value, not affected by surface emission or pollution events. For this reason, it is computed as the monthly climatological median CO of a remote area away from polluted regions, in the upper troposphere

**Table 1.** Description of individual sites and clusters used in this study. The location of the sites is displayed in Fig. 1. NT and ST indicate Northern and Southern Tropical Africa respectively. P O<sub>3</sub> and P CO indicate the total number of profiles for the IAGOS period.

Individual sites/Clusters		IAGOS sites	<u>P O<sub>3</sub></u>	<u>P CO</u>
South America	South Brazil	Rio de Janeiro (Brazil), São Paulo (Brazil)	<u>518</u>	<u>62</u>
	Caracas	Caracas (Venezuela)	<u>414</u>	<u>248</u>
	Bogota	Bogota (Colombia)	<u>190</u>	<u>142</u>
<del>NH-NT</del> Africa	Lagos	Lagos (Nigeria)	<u>311</u>	<u>199</u>
	Sahel	Abuja (Nigeria), Ouagadougou (Uganda), Niamey (Niger)	<u>193</u>	<u>202</u>
	Gulf of Guinea	Lome (Togo), Yaounde (Cameroon), Douala (Cameroon), Libreville (Gabon), Accra (Ghana), <del>Cotonou (Benin), Port Harcourt (Nigeria);</del> Abidjan (Ivory Coast), Malabo (Equatorial Guinea)	<u>414</u>	<u>302</u>
			<u>Cotonou (Benin), Port Harcourt (Nigeria)</u>	
<del>SH-ST</del> Africa	Central Africa	Luanda (Angola), <u>Brazzaville (Congo)</u> Kinshasa (Democratic Republic of Congo) <del>;-Brazzaville (Congo)-</del>	<u>169</u>	<u>89</u>
	Windhoek	Windhoek (Namibia)	<u>651</u>	<u>692</u>
Arabia and Eastern Africa <del>(AEA)</del>	AbuDhabi	Abu Dhabi (United Arab Emirates), Muscat (Oman)	<u>118</u>	<u>56</u>
	Khartoum	Khartoum (Sudan)	<u>157</u>	<u>116</u>
	Addis Ababa	Addis Ababa (Ethiopia)	<u>121</u>	<u>110</u>
	Jeddah	Jeddah (Saudi Arabia)	<u>154</u>	<u>108</u>
Asia	South China	Hong Kong (China), Guangzhou (China), Xiamen (China)	<u>337</u>	<u>562</u>
	Gulf of Thailand	Kuala Lumpur (Malaysia), Singapore ( Singapore)	<u>162</u>	<u>140</u>
	Madras	Madras (India)	<u>239</u>	<u>253</u>
	Hyderabad	Hyderabad (India)	<u>159</u>	<u>170</u>
	Mumbai	Mumbai (India)	<u>61</u>	<u>29</u>
	Manila	Manila (Philippines)	<u>66</u>	<u>101</u>
	Bangkok	Bangkok (Thailand)	<u>526</u>	<u>336</u>
	Ho Chi Minh City	Ho Chi Minh City (Vietnam)	<u>113</u>	<u>90</u>

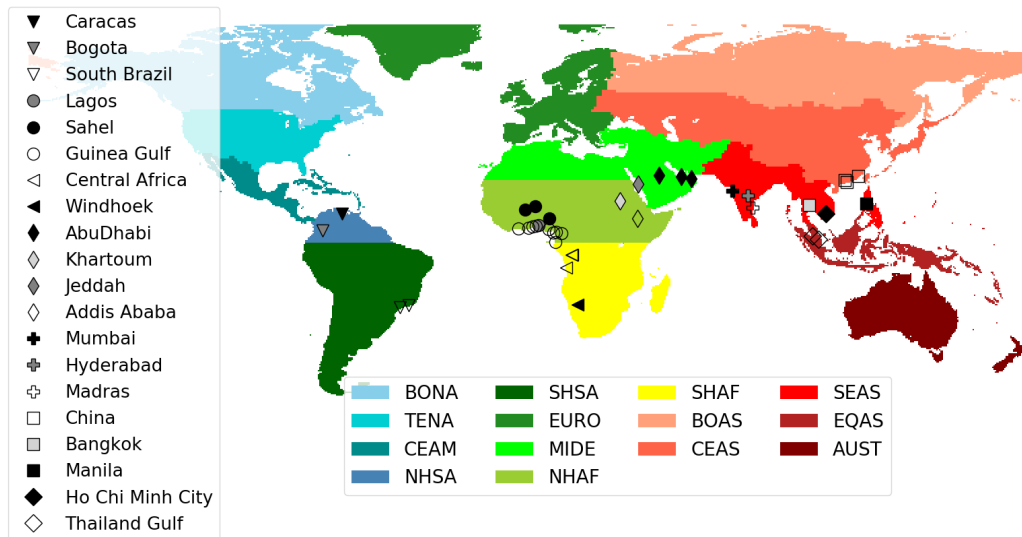


**Figure 1.** Locations of tropical sites served by IAGOS, and geographical source regions used in SOFT-IO model. BONA: Boreal North America; TENA: Temperate North America; CEAM: Central America; NHSA: Northern Hemisphere South America; SHSA: Southern Hemisphere South America; EURO: Europe; MIDE: Middle East; NHAf: Northern Hemisphere Africa; SHAF: Southern Hemisphere Africa; BOAS: Boreal Asia; CEAS: Central Asia; SEAS: Southeast SouthEast Asia; EQAS: Equatorial Asia; AUST: Australia and New Zealand.

190 (300–185 hPa, UT<sub>cruise</sub> (during the whole study period 2002–2020) – (Sect. S4 for more details). We performed an evaluation of SOFT-IO for the lower troposphere (LT, surface–750 hPa), the mid troposphere (MT, 750–350 hPa), and upper troposphere (UT, 300–200 hPa). Our simulations detect CO anomalies at the same rates as Sauvage et al. (2017). On average, SOFT-IO underestimates the observed CO anomalies by 10 ppb in the MT and UT, and by 45 ppb in the LT. A sensitivity test has shown absolute differences of 27% in the LT, 16% in the MT and 10% in the UT between SOFT-IO simulations using AN emissions from MACCity and from CEDS2. This clearly highlights the large uncertainty stemming from uncertainties in AN emissions. Another source of uncertainty comes from the definition of background CO. In order to assess this source of uncertainty, we

195 used the 600–300 hPa median CO mixing ratio as background for each site. The differences between the two backgrounds are within 2.5–60 ppbv. Nevertheless, using the alternative background did not make any difference in the anomaly source attribution and in the relative contributions.

### 2.3 IASI-SOFRID observations

200 The IASI sensor onboard MetOp-A (launched in 2006) has a 12 km footprint at nadir and a 2200 km swath allowing an overpass twice daily at 9:30 and 21:30 local solar time. IASI provides information for the atmospheric composition e.g. content of trace



gases such as O<sub>3</sub> (Eremenko et al., 2008; Barret et al., 2011; Boynard et al., 2016), CO (George et al., 2009; De Wachter et al., 2012) and N<sub>2</sub>O (Barret et al., 2021). We use O<sub>3</sub> (v3.5) and CO (v2.1 up to 2014, and v2.2 up to 2019) IASI retrievals performed with SOFRID (Barret et al., 2020; De Wachter et al., 2012).

SOFRID-O<sub>3</sub> v3.5 retrievals use a dynamical a priori profile based on latitude, season and the tropopause height (Barret et al., 2020). In the tropics, where the surface temperature, thermal contrast and tropopause height are the highest, SOFRID-O<sub>3</sub> retrievals allow two independent pieces of information, one in the troposphere and one in the UTLS (Barret et al., 2020). Comparisons with ozonesonde measurements for the period ~~2007–2017~~2008–2017, showed that SOFRID-O<sub>3</sub> is biased low in the tropical troposphere and UTLS, by  $3 \pm 16 \%$  and  $12 \pm 33 \%$  respectively in the Northern Tropics (0–30°N), and by  $8 \pm 14 \%$  and  $21 \pm 30 \%$  in the Southern Tropics (0–30°S) (Barret et al., 2020). ~~Comparisons between SOFRID-O<sub>3</sub> and ozonesonde measurements above Northern Africa are erroneous, due to retrieval problems in the presence of desert ground with sand emissivity interfering with the O<sub>3</sub> retrievals using a single signature (Boynard et al., 2018). The stripes along the 10° latitude bands in IASI O<sub>3</sub> maps (Fig. 2 e–h and q–t) are due to the use of a dynamical a priori profile and a, resulting in discontinuities between adjacent latitude bands with different a priori profiles. Nevertheless, the use of a dynamical a priori profile showed improvements (e.g. a general increase in the correlation coefficients and the amplitude of the retrieved variability) mostly in the troposphere. The change of the a priori profile leads to minor differences in the UTLS, indicating the highest sensitivity of IASI to this layer (Barret et al., 2020) largely improves the retrieved O<sub>3</sub> profiles in terms of biases, variability and correlation relative to the previous version based on a single a priori profile (Barret et al., 2020).~~

For SOFRID-CO v(2.1 and 2.2 after 2014), two independent pieces of information are provided in the ~~lower (surface–480 hPa) and upper (480–225 hPa)~~ low and upper troposphere (De Wachter et al., 2012). IASI correctly captures the seasonal variability of CO over southern Africa (Windhoek) and European mid-latitudes (Frankfurt) in ~~lower-low~~ (resp. upper) troposphere relative to IAGOS data (resp. correlation coefficients of 0.85 (0.70)). At Windhoek, SOFRID-CO is biased low in the ~~lower low~~ (resp. upper) troposphere by  $13 \pm 20 \%$  (resp.  $4 \pm 12 \%$ ).

We use monthly averaged SOFRID-CO and O<sub>3</sub> retrievals on a 1° x 1° grid from 2008–2019. We focus on ~~pressure levels corresponding approximately to the independent pieces of information, and on~~ daytime measurements when larger thermal contrast between the surface and the atmosphere results in increased sensitivity of the instrument (Clerbaux et al., 2009) and on pressure levels corresponding approximately to the independent pieces of information: low troposphere defined between 900–700 hPa (LT<sub>iasl</sub>), mid troposphere between 600–400 hPa (MT<sub>iasl</sub>) and upper troposphere between 290–220 hPa (UT<sub>iasl</sub>).

### 3 Results

#### 3.1 O<sub>3</sub> and CO over the Northern and Southern Tropics

Figure ?? displays the tropical lower troposphere (LT) IASI CO (a) and middle troposphere (MT) O<sub>3</sub> (b) annual distributions averaged over the 2008–2019 period. The pressure ranges differ for CO and O<sub>3</sub> because they are adjusted to the sensitivity of the instrument for each compound (see Sect. 2.3). For O<sub>3</sub>, the stripes along the 10° latitude bands are due to the use of a dynamical a priori profile (Sect. 2.3), resulting in discontinuities between adjacent latitude bands with different a priori profiles.

235 Nevertheless, the stripes are a minor issue, as the use of a dynamical a priori profile largely improves the retrieved  $O_3$  profiles in terms of variability and correlation in most latitude bands, relative to the previous version which uses a single a priori profile (Barret et al., 2020).

Northern Tropical CO and  $O_3$  mixing ratios are generally higher than those in the SH (Fig. ?? and Table ??). Geographically, the largest CO (165 ppb) and  $O_3$  (60 ppb) maxima are found over Northern Africa (Table ??), followed by comparable CO and  $O_3$  mixing ratios over Southern Africa and East Asia (145–150 ppb of CO and 50 ppb of  $O_3$ ) (Table ??). The smallest magnitude of  $O_3$  and CO maxima are observed over South America.

IASI LT CO (between 900–700 hPa) (a) and MT  $O_3$  (between 600–400 hPa) (b) mixing ratios averaged from 2008 to 2019 on a 1x1 grid.

245 Annual mean LT CO and  $O_3$  mixing ratio (in ppb) over the Northern Tropics (0–25° N), Southern Tropics (0–25° S), Northern Africa (10° W–12.5° E; 0–12.5° N), Southern Africa (10–35° E; 2.5–20° S), East Asia (92.5–110° E; 10–27° N) and South America (35–50° W; 0–20° S) based on IASI data (Fig. ??). NH SH Northern Africa Southern Africa East Asia South America

### 3.1 Regional characteristics of tropical $O_3$ and CO

Figure 2 displays the horizontal distributions of CO 115–100–165–145–150–110– $O_3$  75–45–60–50–50–45–

250 Figures S1 in LT<sub>iasi</sub> (a–d) and S2 show the monthly mean CO flux due to BB and AN emissions respectively. The BB emissions in both hemispheres show strong seasonal variability, as a consequence of the annual shift of the Intertropical Convergence Zone (ITCZ), and the alternance of the rainy and dry seasons. In contrast, AN emissions are located mostly in the NH and have weaker seasonal variability. The differences in CO abundances between the two hemispheres could be related to the spatial distribution of the AN emissions, and the seasonality of the fires. The main emissions of SH CO are the annual dry-season fires, while NH CO is related to the larger population and AN activities (Fig. S2) (Edwards et al., 2004).

255 The CO, and consequently the  $O_3$  maxima over Northern Africa could be related to the strong AN emissions over the Western African coast (Fig. S2a–d). During the dry season, local BB emissions are also active, and could contribute to the CO and  $O_3$  maxima (Fig. S1a). High CO and  $O_3$  over East Asia are likely related to anthropogenic emissions (Fig. S2a–d), in contrast to the SH regions (Southern Africa and South America) where the local dry-season BB emissions are significantly stronger than AN (Fig. S1c–d).

260 The persistent African CO and UT<sub>iasi</sub> (i–l and q–t), and of  $O_3$  maxima are exported over the South Atlantic (Fig. ??a–b), contributing to the wave-one  $O_3$  pattern. The wave-one is associated with systematic high  $O_3$  (60–65 ppb) above the South Atlantic and low  $O_3$  (30–40 ppb) above western Pacific. Similar asymmetry in the  $O_3$  pattern is observed in the NH, but with smaller magnitude because both sides of equatorial Pacific show similarly low  $O_3$  abundance, while  $O_3$  above the North Atlantic is lower than above the South Atlantic (10–15 ppb difference on average) (Fig. ??b).

265 In this Section we have shown that the CO and  $O_3$  maxima over the Northern and Southern Tropics are related to AN and BB emissions, as well as transport in the tropical troposphere. We will therefore focus on the following questions: what are the contributions of the AN and BB emissions to the  $O_3$  and CO abundances in the tropics? Are regional or local emissions

responsible for the O<sub>3</sub> and CO observed enhancements? To answer these questions, in the next section we analyse the O<sub>3</sub> and CO tropical profiles to quantify their persistent and repetitive characteristics. Using the SOFT-IO tool, we aim to establish connections between these characteristics and local or regional AN and BB emissions.

### 3.2 Regional characteristics of tropical O<sub>3</sub> and CO

In this Section, we focus on the tropical CO and O<sub>3</sub> distributions based on IAGOS and IASI data. The combination of the high vertical resolution of IAGOS (Figs. 3, 5, 6, 7 panels 1 in the MT<sub>ias</sub> (e-h) and 2), and the high spatial and temporal coverage of IASI 2-D global distributions (Fig. 2 a-1), allows us to investigate in detail data-sparse regions like the tropics, and monitor their atmospheric composition.

UT<sub>ias</sub> (m-p and u-x). The results shown in Fig. 2 (a-d) motivated our choice in combining IAGOS sites in clusters when it is necessary to increase the number of measurements. The LT<sub>ias</sub> CO maxima, like over the Gulf of Guinea, cover a wide area. Thus, cities located close to each other are likely to experience similar air masses. According to the wind maps they are also affected by similar meteorological conditions (Fig. S3).

Figures 3, 5, 6, 7 (panels 1 and 2) display the monthly average vertical distributions of O<sub>3</sub> and CO based on IAGOS data, since 1994 and 2002 respectively, for the African, Asian, South American, Arabian and Eastern African clusters. Panels 3 to 5 represent the mean contribution to these CO mixing ratios from AN and BB emissions as estimated by SOFT-IO, with information about their geographical origin (see Sect. 2.2 and Fig. 1). To better understand O<sub>3</sub> and CO anomalies, Fig. 4 displays the CO contributions in three tropospheric layers related to different dynamical regimes: lower troposphere below 750 hPa, LT corresponding roughly to planetary boundary layer (PBL); mid troposphere above up to 300 hPa, and upper troposphere above up to 200 hPa; MT above, and UT corresponding to the beginning of maximum convective detrainment.

#### 3.1.1 Africa (NH Africa: Lagos-Nigeria-, Sahel and Gulf of Guinea; SH Africa: Central Africa, Windhoek-Namibia-)

The striking feature of CO and O<sub>3</sub> over the NH African clusters (Sahel, Gulf of Guinea and Lagos) African clusters is the LT maxima during the dry season (January for the Northern Hemisphere and July for the Southern Hemisphere) (Fig. 3 panels 1-2). CO maximises close to the surface, with larger mixing ratios over Lagos (850 ppb) than Sahel (500 ppb) and Gulf of Guinea and Central Africa (400 ppb), mainly due to local AN emissions (58 % over Lagos and Sahel) (Figs. 3 panel 3a; A1 panel 1a; 4a; A2a), despite the active local fires (Fig. S1a). This is consistent with the increasing AN emissions (Lioussé et al., 2014) and decreasing BB area extend (Hickman et al., 2021) over northern Africa. The O<sub>3</sub> gradient close to the surface (Fig. 3 panels 1a-1e) is likely related to surface deposition and titration by highly concentrated nitrogen oxide (NO) (Monks, 2005) which is expected along with high CO emissions the high CO concentration. The O<sub>3</sub> maximum and the elevated CO levels (exceeding 300-500 ppb) at 2.5 km over the three-four clusters, likely indicate chemically processed air masses where.

During the Northern Hemisphere dry season (January), the AN contribution dominates over Lagos (58%) and Sahel (57%), while BB slightly dominates over Gulf of Guinea (53 %) (Figs. 3 panel 3a; A1 panels 1a and 2a; 4a; A2a). Contribution from the Northern Hemisphere African fires is also found over Central Africa, where it intensifies and becomes the only important one between 2 and 4 km (Fig. 3 panel 4a). During transport from Northern Hemisphere Africa, the air masses impacted

by BB emissions are chemically processed resulting in the formation of an O<sub>3</sub> ~~has been produced by precursors. The air masses above the~~ secondary maximum of 50 ppb coincident with the CO maximum (Fig. 3 panel 1d and 2d) as described in Sauvage et al. (2005). During the Southern Hemisphere dry season (July), the local (Southern Hemisphere Africa) fires are responsible for the CO anomalies over Central Africa in the LT and MT by 90 % (Fig. 4a and b). Impact of these fires is also  
305 found in the NT Africa clusters. CO over Lagos is mostly attributed to Southern Hemisphere African emissions (69 ppb) (Fig. 4a), from the surface to about 5 km (Fig. 3 panel 3c). Similar to Lagos, CO over the Gulf of Guinea and Sahel originates from local AN and Southern Hemisphere African BB emissions (Fig. A1 panels 1c and 2c).

The air masses above the fires in NT Africa (resp. ST Africa)(Fig. S1a and S1c resp.) during the respective dry seasons are transported from the continent (Fig. S3a and S3c resp.) by the north-easterly Harmattan flow (Sauvage et al., 2005). AN  
310 emissions are the dominant source of CO at 2.5 km over Lagos and Sahel (Figs. 3 panel 3a and A1 panel 3a). The (resp. the south easterly winds) (Sauvage et al., 2005). This result is clearly consistent with IASI LT<sub>iasi</sub> CO (Fig. 2a and c) which shows transport from the fire region where the highest concentrations are detected towards Southern Africa in January (resp. the Gulf of Guinea and southern West Africa in July). In the NT, the enhanced O<sub>3</sub> and CO are confined in the LT low troposphere due to the stability of the Harmattan flow and Saharan anticyclone which prevent vertical mixing (Sauvage et al., 2005). The stability  
315 is due to a temperature inversion which characterises the trade current, as moist cooler air above the surface is capped by dry warmer air above, resulting from advection by the Harmattan flow or subsidence in the anticyclone.

IAGOS monthly mean O<sub>3</sub> (panel 1) and CO (panel 2) vertical distributions for the African clusters and sites. The annotated numbers correspond to the number of flights per month, given in the same colour as in the legend. The shadowed part corresponds to  $\pm 1$  one standard deviation. The location of the clusters and sites is displayed in Fig. 1. Vertical distribution  
320 of CO contributions (in ppb), averaged over all the positive CO anomalies observed in the IAGOS vertical profile (panels 3 to 5). The geographic origin of CO emissions is indicated by the different colours, with the hatched part showing AN contribution, and the non-hatched part BB contribution. Note that the source region where the site belongs to is indicated by the colour of the box.

Mean SOFT-IO contributions (in ppb), averaged over all the positive CO anomalies for the tropical sites (Caracas, Lagos, Central Africa, South China and Bangkok) for low (a), mid (b) and upper (c) troposphere. The geographic CO origin of CO is  
325 indicated by the colours, for the AN (hatched) and BB (unhatched) contributions. Each pie corresponds to a different month and each group of four pies refer to a different site (see panel b).

Elevated LT CO levels (Over the NT African clusters, secondary CO and O<sub>3</sub> maxima are observed below 4 km ) are observed  
330 all year long over the NH African clusters (Fig. 3 panels 1a–1c and 2a–2c) except October. During during the transition from the NH Northern Hemisphere dry to wet season (April), when the fires are suppressed (Fig. S1b), LT CO mainly comes from local AN emissions (Figs. 3 panel 3b; A1 panels 1b and 2b), located over Ethiopia and Nigeria (Fig. S2b). The fact that SOFT-IO attributes approximately 80 ppbv of CO to local AN emissions (Figs. 3 panel 3b; A1 panels 1b and 2b), while the observed anomaly reaches 200–250 ppbv and no or few fires are detected by MODIS (Yamasoe et al. (2015); their Fig.7), indicates underestimation of the NHAfrican Northern Hemisphere African AN emissions. Nevertheless, these These high CO concentrations  
335 in April are detected by IASI in the LT<sub>iasi</sub> (Fig. 2b) over the whole of West Africa indicating the large-scale extent of the impact

of these emissions. The enhanced LT O<sub>3</sub> over the three clusters in April (Figs. 3a–c) indicates possible O<sub>3</sub> formation during the transport of the aforementioned emissions towards Sahel and the Gulf of Guinea. A small O<sub>3</sub> enhancement is also detected by IASI in the mid-troposphere (400–600 hPa) over west-MT<sub>iasl</sub> over West Africa (Fig. 2f). During the dry season, nitrogen is accumulated in soils (Jaeglé et al., 2004). ~~The beginning of rains activates the bacterial nitrification leading to significant release of NO which is rapidly converted into NO<sub>2</sub> via oxidative processes. Thus, enhanced NO~~Enhanced NO<sub>x</sub> concentrations, possibly due to soil emissions when rains start, also contribute to the O<sub>3</sub> increase over NH-NT Africa in April (Saunois et al., 2009). ~~The O<sub>3</sub> enhancement is larger over Sahel relative to Lagos and the Gulf of Guinea, especially over Sahel~~ (Fig. 3 panel 1a–c) because of higher NO<sub>2</sub> concentrations above dry savannas (Sahel) ~~compared to~~ than over wet savannas and forests (Southern Western Africa) (Adon et al., 2010). After excess nitrogen is consumed, the wet-season NO emissions decrease, contributing less to the local O<sub>3</sub> (Adon et al., 2010).

~~During the NH wet season (July), CO close to the surface over Lagos is mostly attributed to southern African (SHAF) emissions (70 ppb)~~At Windhoek, O<sub>3</sub> and CO maximise in October after Southern Hemisphere dry season (Fig. 3 panels 1e and 2e). This CO peak has the smallest magnitude among the African clusters (150 ppb at 4 km), while O<sub>3</sub> peak is among the largest, reaching 80 ppb in the UT (11.5 km). The LT CO anomalies over Windhoek in October are mainly caused by local BB emissions (68 % BB versus 12 % AN) (Fig. 4A2a). ~~This result is clearly consistent with IASI LT CO July distribution~~ These high CO concentrations in October are detected by IASI in the LT<sub>iasl</sub> (Fig. 2e) ~~which suggests transport from the fire region where the highest concentrations are detected towards the Gulf of Guinea and southern West Africa. The contribution of SHAF emissions is relatively constant from the surface to about 5 km~~ d) over the whole of Southern Africa reflecting the large extent of the impact of these emissions. Using MOPPIT CO and MODIS fire count data, Edwards et al. (2006) also noticed the time lag between the peak of the fires and the CO concentration over Southern Africa. They attributed the lag to smoldering fires at the end of the burning season, characterised by low combustion efficiency and increased CO emissions factors (Zheng et al., 2018b). In addition, there is non-negligible influence from Southern Hemisphere South American emissions (20 % mostly BB)(Figs. 3 panel 5d and A2a). The Southern Hemisphere South American BB contribution increases with height (30 % contribution in MT and 50 % in UT) contributing to the O<sub>3</sub> maximum observed in the UT (Fig. A2b and c) (Sauvage et al., 2006).

~~An O<sub>3</sub> enhancement of 80 ppb is also observed over Central Africa at 8 km in October~~ (Fig. 3 panel 3e). ~~This suggests transport of chemical mature air masses from the SH African fires towards Lagos, via the south easterly trade winds turning to the monsoon westerly flow (Sauvage et al., 2007a; Barret et al., 2010). The lower 1d) highlighting the stronger seasonal variability of MT and UT O<sub>3</sub> in ST than NT Africa related to the intense lightning activity in the Southern Hemisphere and the South Atlantic O<sub>3</sub> maximum (Sauvage et al., 2007b, c). The IASI UT<sub>iasl</sub> O<sub>3</sub> mixing ratio close to the surface is likely attributed to rapid deposition to forested areas and photochemical destruction in the moist monsoon air (Reeves et al., 2010). Similar to Lagos, CO over the Gulf of Guinea and Sahel originate from local AN and SHAF BB emissions~~ distribution clearly shows that the O<sub>3</sub> maximum covers the entire region from South America to Africa south of the Equator (Fig. 2l).

The annual minima of CO and O<sub>3</sub> over the African clusters occur during the transition from the wet to the dry season (April for ST and October for NT), when the local fires are suppressed (Fig. A1 panels 1e and 2e).

370 ~~Below about 4 km, the annual S1b and d). Over NT Africa, the  $O_3$  minimum occurs in October over the three clusters below about 4 km (Fig. 3 panel 1a–c). The CO maximum mixing ratio below 1 km is due to local AN emissions (Figs. 3 panel 3d; A1 panels 1d and 2d). In contrast with the other months, the CO mixing ratio above the surface maximum decreases sharply with altitude showing low CO concentrations from 2 km to 12 km. Indeed, in October, the monsoon flow has disappeared and West Africa is impacted by the north easterly trade winds which block the transport of air masses impacted by BB from~~  
375 ~~SHAF Southern Hemisphere Africa as is clearly visible on the LT-low tropospheric CO distribution from IASI (Fig. 2d). This is confirmed by the predominant local (NHAF Northern Hemisphere Africa) origin of CO over Lagos which is almost not impacted by SHAF-BB in October (Fig. 3 panel 3d). The similar  $O_3$  profile close to the surface with the one in July (Fig. 3 panel 1e), indicates significant ozone chemical and depositional sinks as in July. The influence of the moist air over Lagos and Guinea Gulf responsible for the photochemical destruction of  $O_3$  below 2.5 km is confirmed by high levels of RH (Fig. not~~  
380 ~~shown).-~~

~~The classical increase of  $O_3$  from the surface to the MT in October (and July) is because the role of photochemistry changes from a net sink to a net source of ozone above 6 km, depending on the  $NO_x$  concentration (Jacob et al., 1996). In the tropics, photochemical  $O_3$  destruction dominates the lower troposphere (Archibald et al., 2020), where water vapour concentrations are high, and in highly polluted regions where there is direct removal by titration with NO (Monks et al., 2015). The vegetation~~  
385 ~~can also act as a rapid sink for  $O_3$  via dry deposition (Cros et al., 2000). The lack of these sinks in the free troposphere, coupled with lower water vapour concentrations leads to an increase of  $O_3$  with altitude (Archibald et al., 2020). Lightning can also increase  $O_3$  mixing ratios in the MT and UT (Barret et al., 2010).-~~

~~$O_3$  and CO distribution over Central Africa in the SH dry season (July) is very similar to NH Africa in the respective dry season (Fig. 3 panels 1d and 2d). CO is characterised by two distinct maxima close to 400 ppb close to the surface and between~~  
390 ~~2 and 4 km, exclusively due to local emissions (SHAF) (Fig. 3 panel 4e). This is visible on the IASI LT CO distribution with a strong isolated maximum over the whole central African region (Fig. 2e). The contribution of local fires is lower close to the surface (80 ppb) than in the upper layer (280 ppb). The  $O_3$  gradient close to the surface is due to influence by the southern monsoon flow (Sauvage et al., 2005) (high RH below 1.5 km; Fig. not shown). CO emitted above the fires (over Angola, Zambia and Dem. Rep. of Congo Fig. S1e) is transported towards the IASI CO maximum over Central Africa via the~~  
395 ~~south easterly winds (Fig. 2e). During the transport  $O_3$  is formed (Sauvage et al., 2005, 2007a). As in NH Africa,  $O_3$  and CO enhancements over Central Africa in the dry season are confined below 4 km, because of the stability of the layers below 5 km due to strong temperature inversions.-~~

~~In October, 3 maxima at the surface, 2 and 4 km visible over Central Africa are due to local emissions (SHAF-AN and BB). The lower CO concentrations between the surface and 2 km is probably resulting from the enhancement of the contribution of~~  
400 ~~these emissions with altitude (Fig. 3 panel 4d). In January the vertical distribution of CO is characterised by two maxima, at the surface and at 2 km. Below 1 km, the main contributions are local AN, and BB NHAF emissions. The contribution from the NHAF fires intensifies and becomes the only important one between 2 and 4 km. During transport from northern Africa, the air masses impacted by BB emissions are chemically processed resulting in the formation of an  $O_3$  secondary maximum of 50 ppb coincident with the CO maximum (Fig. 3 panel 1d and 2d) as described in Sauvage et al. (2005).-~~

405 Interestingly, the annual CO surface maximum in Central Africa Occurs in April, before the beginning of the ~~SH fires. It is~~  
Southern Hemisphere fires, due to local AN emissions (~~SHAF~~) (Fig. 3 panel 4b). The measured CO maxima reaches 350 ppb,  
while SOFT-IO attributes 40 ppb ~~above the background levels~~ to the aforementioned sources. This means that ~~SHAF~~ Southern  
Hemisphere African AN emissions are likely underestimated. Above 1km, in the absence of fire contributions, CO remains  
constant with 100 ppb which is the annual minimum, and the O<sub>3</sub> profile is characterised by a steep gradient and the lowest  
410 annual concentrations. IASI LT ~~CO~~ CO<sub>i</sub> distribution (Fig. 2b) indicates that the CO minimum measured by IAGOS above 1km  
over Central Africa in April extends over the whole ~~central and southern Africa. The maximum close to the surface is indeed~~  
~~not detectable by IASI. Central and Southern Africa.~~

~~At Windhoek, The classical increase of O<sub>3</sub> and CO maximise in October after SH dry season (July) (Fig. 3 panels 1e from~~  
~~the surface to the MT in October and 2e). This CO peak has the smallest magnitude among the African clusters (150 ppb at 4~~  
415 ~~km), while O<sub>3</sub> April is due to photochemistry which changes from a net sink to a net source of ozone above 6km, depending on~~  
~~the NO<sub>x</sub> concentration (Jacob et al., 1996). In the tropics, photochemical O<sub>3</sub> peak is among the largest, reaching 80 ppb in the~~  
~~UT (11.5 km).~~

~~The LT CO anomalies over Windhoek in October are mainly caused by local BB emissions (68 % BB versus 12 % AN)~~  
~~(Fig. A2a). Interestingly, the contribution from the local fires is larger than in July (by 7 ppb in the LT; Fig. 3 panel 5c),~~  
420 ~~when the peak of the fire emissions occurs (Fig. S1c-d). These high CO concentrations in October are detected by IASI in~~  
~~the LT (Fig. 2d) over the whole of South Africa reflecting the large extent of the impact of these emissions. Using MOPPIT~~  
~~CO and MODIS fire count data, Edwards et al. (2006) also noticed the time lag between the peak of the fires and the CO~~  
~~concentration over South Africa. They attributed the lag to smoldering fires at the end of the burning season. The CO emissions,~~  
~~and thus the concentrations, are larger over the savanna fires during October, because of the low combustion efficiency of the~~  
425 ~~smoldering fires resulting in increased CO emissions factors (Zheng et al., 2018b). In addition, there is non-negligible influence~~  
~~from Southern Hemisphere South America (SHSA) emissions (20 % mostly BB)(Figs. 3 panel 5d and A2a). The SHSA BB~~  
~~contribution increases with height (30 % contribution in MT and 50 % in UT) contributing to the~~  
~~destruction dominates the~~  
~~low troposphere (Archibald et al., 2020), where water vapour concentrations are high, and in highly polluted regions where~~  
~~there is direct removal by titration with NO (Monks et al., 2015). The vegetation can also act as a rapid sink for O<sub>3</sub> maximum~~  
430 ~~observed in the UT (Fig. A2b and c) (Sauvage et al., 2006). The absence of a strong CO maximum at the height of the O<sub>3</sub>~~  
~~maximum suggests an additional source of O<sub>3</sub> over Windhoek's UT. As already mentioned (Sect. ??), the high O<sub>3</sub> over South~~  
~~Africa is associated with the South Atlantic O<sub>3</sub> maximum which intensifies in October due to the strong LiNO<sub>x</sub> production~~  
~~over southern Africa and south America (Sauvage et al., 2007b, c).~~

~~It is noteworthy that an~~ via dry deposition (Cros et al., 2000). The lack of these sinks in the MT and UT, coupled with lower  
435 water vapour concentrations leads to an increase of O<sub>3</sub> enhancement of 80 ppb is also observed over Central Africa at 8 km in  
October (Fig. 3 panel 1d) highlighting that the stronger seasonal variability of with altitude (Archibald et al., 2020). Lightning  
can also increase O<sub>3</sub> in the mid and upper troposphere in SH than NH Africa is due to the intense lightning activity in the SH.  
The IASI UT O<sub>3</sub> distribution clearly shows that the O<sub>3</sub> maximum covers the entire region from South America to Africa south  
of the Equator (Fig. 2f). mixing ratios in the MT and UT (Barret et al., 2010).

440 The annual minimum of  $O_3$  and CO over Windhoek occurs in April (Fig. 3 panels 1e and 2e), the transition period from SH wet to dry season, when the local fires are suppressed (Fig. S1b). The CO mixing ratio is less than 100 ppb over the whole tropospheric column and comes from local AN emissions. In comparison to Central Africa, Windhoek is less influenced by SHAF emissions due to its remote location away from sources (Petetin et al., 2018b). The  $O_3$  minimum of less than 30 ppb probably results from titration by NO above the surface.

### 445 3.1.2 Asia: ~~Mumbai, Hyderabad, Madras-India-, Ho Chi Minh City-Vietnam-, Manila-Philippines-, Bangkok-Thailand-, Gulf of Thailand, South China~~

Over the Asian clusters, the CO profiles display the highest mixing ratios in the surface layer (below 1km) all year long (Fig. 5 panel 2). ~~The annual maximum annual CO maximum close to the surface~~ occurs in January (except over Manila and the Gulf of Thailand)(Fig. 5 panel 2), due to the lowest boundary layer height ~~during winter. The winter surface CO maximum~~ ranges from 300 ppb over oceanic sites (Madras) to 700 ppb over megacities (Ho Chi Minh and Mumbai)~~in winter~~, and is mainly attributed to local ~~or regional~~ AN emissions (Figs. 5 ~~panels 3a to 5a; and~~ A1 panels 3a to 4a, 5a). Over the Indian and South China clusters~~in January, local emissions (SEAS and CEAS, local AN emissions (SouthEast and Central Asian resp.)~~ are dominant, with contributions ~~in the range of from~~ 85 to 95 % (Figs. 5 ~~panel panels~~ 3a and 4a; A1 panel 3a and 4a, and 4a). ~~The impact of these Chinese emissions (CEAS) is not limited to a local scale, as they dominate AN Central Asian emissions~~ ~~mainly control~~ the LT CO anomalies over the ~~rest of the~~ Asian clusters (except Bangkok) ~~with contributions in the range of in~~ ~~January from~~ 52 % (over ~~the~~ Gulf of Thailand) to 75 % (over Manila) (Figs. 4a, A2a and A3a) ~~. Their advection is favoured due to due to their advection by~~ the northeasterly trade winds. ~~Bangkok is also impacted by CEAS emissions (42%), but the local AN (45%) and BB (10%) contributions are more important (Fig. 4a).~~

~~In winter, The~~ elevated CO mixing ratios below 2.5 km ~~are related to over the Asian clusters in January are coincident with~~  $O_3$  enhancements (Figs. 5 panel 1) ~~. During winter due to~~ the chemical ageing ~~of the air masses in the LT is~~ favoured by: i) the confinement of the CO-rich air masses due to the large-scale subsidence ~~preventing upward vertical motions~~ (Lelieveld et al., 2001) and ii) the cloud free conditions ~~promoting  $O_3$  formation~~. This  $O_3$  enhancement ~~has been~~ described in Barret et al. (2011) for South Asia during the post monsoon ~~based on IASI  $O_3$  data for 2008. It is also visible on the climatological IASI MT  $O_3$  map is also detected by IASI~~ (Fig. 2f). ~~The accumulation of CO and  $O_3$  in the LT over the Asian clusters, is observed in lower altitudes than in the NH African ones (see Sect. 3.1.1). This is due to the lower PBL height in DJF over tropical Asia than Africa as suggested by Kalmus et al. (2022).~~

During the pre monsoon season (April), CO and  $O_3$  are both enhanced above the ~~PBL boundary layer~~ and below 4 to 6 km over most sites ~~of the Asian clusters. (Fig. 5 panels 1 and 2)~~. Local AN emissions control the CO anomalies over the majority of the ~~Asian sites~~ (Figs. 5 panels 3b–5b; A1 panels 3b–7b), while spring ~~SEAS fires significantly SouthEast Asian fires~~ impact South China~~and Bangkok, but also, Bangkok, Ho Chi Minh City and Manila~~ ~~. The contributions of the SEAS fires in this cluster are in a range of 20 and 30 by 20–30 %~~ in the LT and MT (Figs. 4a and b; A3a and b). In spring ~~, the fires are mostly located~~ above East Asia and especially the region of Myanmar, Northern Thailand and Laos (Fig. S1b) and the corresponding large CO concentrations are captured by IASI (Fig. 2b). ~~The westward LT and MT winds above the fires explain the BB outflow~~



towards South China and the Pacific ocean is due to westward low and mid tropospheric winds (Figs. 2b and S3b and S3f). The  
475 enhanced MT O<sub>3</sub> is attributable to the intense solar radiation associated with the important amounts of precursors from AN  
and BB emissions which were previously evidenced. This is in agreement with the observed O<sub>3</sub> maximum in spring over South  
China (e.g. Dufour et al. (2010) using IASI data) and Bangkok (Sahu et al. (2013) using IAGOS data). Using observational  
(IAGOS and IASI) and model (Model for OZone And Related chemical Tracers-version-4 model) data, (Dufour et al., 2010)  
and Bangkok (Sahu et al., 2013). Yarragunta et al. (2019) found that local AN emissions are responsible for the CO and O<sub>3</sub>  
480 abundances over South India during the pre-monsoon season. This is in accordance with the SOFT-IO contributions over the  
Indian clusters (Figs. 5 panels 3b; A1 panels 3b and 4b; A3a). However, it is worth noticing that CO anomalies over Mumbai  
are also caused by transport of AN emissions from MIDE the Middle East (36%) in the LT, and NHAF Northern Hemisphere  
Africa (30%) in the MT (Fig. A3a and b). In the UT, where the transport of the air masses is favoured, the impact of NHAF the  
impact of Northern Hemisphere African (AN and BB) emissions dominates over Mumbai (54 %) and Hyderabad (50 %). The  
485 UT It has to be noted that the number of profiles over Mumbai (6) and Hyderabad (19) are lower than the threshold established  
for representativeness (see Sect. 2.1.1). The UT<sub>ias</sub> CO and O<sub>3</sub> transport from NHAF Northern Hemisphere Africa towards the  
Arabian sea and South India is also captured by the IASI maps IASI (Figs. 2j and 2n), indicating O<sub>3</sub> photochemical production  
during the transport.

The BB contribution is also important during the post monsoon season (October) because of active fires over Indonesia (Fig.  
490 S1). The Gulf of Thailand cluster is the most affected, from the surface (600 ppb) to the UT (Fig. 5 panel 1e). Interestingly,  
the CO mixing ratio at 6–12 km is approximately 200 ppb over the Gulf of Thailand cluster, the highest CO abundance in  
the MT and UT among the Asian clusters. IASI CO data (Fig. 2d) and wind fields (Fig. S3d) show that the LT<sub>ias</sub> CO-rich  
air masses impacted by the fires (Fig. S1d) are advected towards the SE Asian coast South East Asian coastal clusters (South  
China, Gulf of Thailand, Bangkok and Manila), as confirmed by the SOFT-IO contributions (contributions of 10 % EQAS  
495 contribution on average) in addition to the local AN influence (Figs. 5 panels 4d and 5d; A1 panels 6d and 7d; 4a; A2a and  
A3a). The collocated O<sub>3</sub> enhancement (below 2 km) over the SE Asian coast these clusters (Figs. 5 pane 1c–1e) indicates O<sub>3</sub>  
production by BB and AN precursors.

The contribution of the EQAS BB The Equatorial Asian BB contribution intensifies in the UT in October, reaching 40–57 %  
over the SE Asian coastal clusters, and 33 % (resp. 40–57 %), Madras (50 %) over Hyderabad (resp. Madras and Hyderabad  
500 (33 %) (Figs. 4c; A2c and A3c). The UT upper tropospheric CO maximum above the fires is also captured by IASI and IAGOS  
UT data (Figs. 2l; 2p and S1d). Based on MLS CO data, Livesey et al. (2013) also found an UT upper tropospheric CO  
maximum over Indonesia and attributed it to episodically strong convection, in agreement with the low outgoing longwave  
radiation at OLR in Fig. 2p. In contrast, the UT and MT<sub>ias</sub> and MT<sub>ias</sub> O<sub>3</sub> distribution show a SE-NW gradient (Figs. 2l  
and 2h) with lower O<sub>3</sub>-levels over the Maritime continent and the southern Indian Ocean and higher ones over India and the  
505 Arabian sea. This was reported by Barret et al. (2011) as a result of convection over the first region and subsidence of precursor  
enriched air masses over the second one.

The LT O<sub>3</sub> and CO mixing ratios over the Asian clusters minimise during the summer monsoon (July) (Fig. 5 panels 1–2).  
The reversal of the north-easterly trades to the monsoon flow (Fig. S3c) results in advection of O<sub>3</sub>- and CO-poor air masses

from the Indian ocean towards Asia. ~~The lowest O<sub>3</sub> levels close to the surface are observed over Mumbai due to the stronger~~  
510 ~~oceanic influence (high relative humidity close to the surface compared to the other clusters, Fig. not shown). Furthermore,~~  
~~convective clouds result in cloudy conditions, and rain scavenges~~ Furthermore, cloudy conditions scavenging of O<sub>3</sub> precursors  
~~resulting result~~ in lower O<sub>3</sub> production than in clear sky conditions (Mari et al., 2000; Safieddine et al., 2016). The steep CO  
gradient close to the surface (below 1 km) ~~clearly~~ indicates the convective uplift of polluted PBL boundary layer air masses  
towards the UT. The resulting enhancement of CO in the UT within the AMA Asian monsoon anticyclone (AMA) analysed  
515 in Park et al. (2008) and Barret et al. (2016) is clear from IASI (Fig. 2k). In contrast, the positive ~~south-north~~ South-North O<sub>3</sub>  
gradient between the Maritime continent and north ~~SAsia~~ South Asia and Middle East (Figs. 2o and w) is associated with: i)  
the photochemical ageing of air masses while they are recirculating towards Middle East, ~~allowing sufficient O<sub>3</sub> production~~  
~~during transport~~ (Lawrence and Lelieveld, 2010) and ii) the high insolation over Middle East ~~favouring O<sub>3</sub> photochemical~~  
~~production~~ (Barret et al., 2016).

### 520 3.1.3 South America: ~~Caracas-Venezuela, Bogota-Colombia and SBrazil~~

~~Over Caracas and Bogota, the concentrations of CO in the troposphere are maxima in April and minima in January, while the~~  
~~highest concentrations occur in October over SBrazil (Fig. 6 panel 2). In April, CO concentrations exceed 400 ppb over Bogota~~  
~~below 1 km above the surface, and 200 ppb up to 2 km over Caracas. The CO concentrations detected by IASI over northern~~  
~~Venezuela and Colombia are also maxima in April (Fig. 2b). This is clearly related to the large vertical extent of the high~~  
525 ~~concentrations which improves the detection by IASI. In terms of CO, Bogota is the most polluted cluster over South America~~  
~~throughout the year.~~

~~Same as Fig. 3 for the South American clusters.~~

~~In January, CO concentrations are below 300 ppb (resp. 180 ppb) over Bogota (resp. Caracas and SBrazil) below 1 km~~  
~~a.s.s. (Fig. 6 panel 2). The CO mixing ratios decrease below 100 ppb above the polluted layers all year long, with exception of~~  
530 ~~South Brazil, where a first maximum (150–200 ppb) occurs in the MT (2–4 km) and a second one (200–250 ppb) is observed~~  
~~above 8 km in October. IASI clearly detects the MT (Fig. 2d) and UT (Fig. 2p) maxima over most of tropical south America~~  
~~in October.~~

~~The~~ One common characteristic among the South American clusters is the increase in O<sub>3</sub> ~~profiles over South America~~  
~~generally display the classical increase~~ from the surface to the MT (Fig. 6 panel 1). ~~The increase of O<sub>3</sub> with altitude is~~  
535 ~~attributed~~ This is due to the lack of depositional and chemical sinks ~~in the FT~~ above the low troposphere, in combination with  
lower water vapour concentrations, and lightning emissions, as discussed in Sec. 3.1.1.

~~Over Caracas, tropospheric CO is maximum in April (250 ppbv) and the profile displays one maximum of~~ In Caracas, O<sub>3</sub>  
~~(40 ppb) shows one maximum~~ in the LT and one in the MT ~~(50 ppb) in April~~. Over Bogota and SBrazil O<sub>3</sub> ~~is maximum peaks~~  
in October over the whole troposphere with mixing ratios reaching 45 and 60 ppb in the UT. For Bogota (resp. SBrazil) the  
540 tropospheric O<sub>3</sub> annual minimum occurs in July (resp. April). As IAGOS over SBrazil below 6 km, the IASI distributions over  
tropical South America (Fig. 2 ~~e to h~~) ~~display lower tropospheric~~ e-h display MT<sub>iasl</sub> O<sub>3</sub> in January and April than in July and  
October.

From Another common characteristic among the three clusters is the LT CO maximum in April (Fig. 6 panel 2). The CO mixing ratios peak over Bogota below 1km (400 ppb) and over Caracas up to 2km (200 ppb). According to SOFT-IO we can see that, over SBrazil in October, CO enhancement below 1 km is caused by the CO maximum over Caracas is due to local AN (52-35 %) and BB (44-32 %) emissions (Fig. 6 panel 5d). In the MT and the UT, the BB contribution exceeds 80 % because of the strong convection moving over the BB regions (Liu et al., 2010). This is also indicated by low outgoing longwave radiation Northern Hemisphere South America) (Figs. A2, and 6 panel 5b). Similar contributions are found over Bogota (Fig. 6 panel 4). This local origin of emissions is corroborated by the elevated IASI LT<sub>ias</sub> CO mixing ratios (Fig. 2l) which is used as a convection proxy (Park et al., 2007). The uplifted BB products are trapped in an anticyclonic circulation developed over Central South America b) collocated with the strong AN emissions above Colombia and Venezuela, and active fires above the latter (Figs. S1b and S2b). Transport also plays an important role with 20 % of the anomalies caused by BB Northern Hemisphere African emissions (Fig. S3l). CO from SHSA fires are transported over Bogota, at the edge of the anticyclone, but does not reach Caracas which lies outside of the anticyclone 4a). The O<sub>3</sub> maximum collocated with the CO one at 2 km over Caracas (Fig. 6 panels 3d and 4d). Their photochemical processing contributes to the seasonal 1a and 2a), indicates O<sub>3</sub> enhancement over South America which is the western part of the wave-one pattern (Thompson et al., 2003b; Sauvage et al., 2006). This is highlighted by the collocation of IASI UT CO (Fig. 2l) and production during transport of Northern Hemisphere African air masses impacted by BB. The second O<sub>3</sub> (Fig. 2p) maxima within the anticyclone. Nevertheless, as described by Sauvage et al. (2007e) the lightning activity over South America and Africa in October is the most important cause of the O<sub>3</sub> wave-one pattern maximum above 5 km over Caracas is also noticed by Yamasoe et al. (2015) that attributed it to local AN sources followed by lightning.

Below 1km Over SBrazil, the annual CO maximum over SBrazil in April below 1.5 km in April (Fig. 6 panel 2c) is due to local AN emissions (Fig. 6 panel 5b) located over the southern part of Brazil (Fig. S2b). The observed CO enhancement reaches approximately 350 ppb (Fig. 6e), while SOFT-IO attributes 65 ppb above the background levels to the aforementioned emissions. This indicates that SHSA Southern Hemisphere South American AN emissions are underestimated by the SOFT-IO calculations. The observed CO enhancement at 1.5 km is a new CO feature new compared to Yamasoe et al. (2015) that studied CO climatology over SBrazil for the period 1994–2013. The CO enhancement is due to additional data that were collected for the year 2014. SOFT-IO shows and is related to increased local AN contributions for March–April–May 2014 relative to the previous years. This is in agreement with the CEDS inventory, which shows a peak in AN emissions over South Brazil (18–29° S and 35–52° W) for the year in 2014, mostly coming from the transportation sector (Fig. not shown).

Over Caracas, the annual CO maximum below 2 km in April mostly comes from local AN (35 %) and BB (32 %) emissions (NHSA) (Figs. A2, and 6 panel 5b). This local origin of emissions is corroborated by the elevated IASILT

The CO minima over the three clusters are observed in January, when CO concentrations are below 300 ppb (resp. 180 ppb) over Bogota (resp. Caracas and SBrazil) below 1km (Fig. 6 panel 2). The CO mixing ratios (Fig. 2b) collocated with the strong AN emissions above Colombia and Venezuela, and active fires above the latter (Figs. S1b and S2b). Transport also plays an important role with 20 % of the anomalies caused by BB NHAF emissions (Fig. 4a). The O<sub>3</sub> maximum collocated with the CO one at 2 km decrease below 100 ppb above the polluted layers all year long, with exception of SBrazil, where a first maximum

(150–200 ppb) occurs between 2–4 km and a second one (200–250 ppb) above 8 km in October. IASI clearly detects the  $MT_{iasi}$  and  $UT_{iasi}$  (Fig. 6 panels 1a and 2a), indicates  $O_3$  production during transport of NHAF air masses impacted by BB. The second  $O_3$  maximum above 5 km is also noticed by Yamasoe et al. (2015). Using the GEOS-chem model, they identified local anthropogenic sources followed by lightning, as the main sources of  $O_3$  precursors over Caracas in April. In addition, the  $O_3$  maximum at around 6 km in October was attributed to local anthropogenic sources and lightning from Africa. This transport pathway from Africa to Caracas in October is confirmed by SOFT-IO (2d and p resp.) maxima over most of tropical south America in October.

From SOFT-IO we can see that, over SBrazil in October, CO enhancement below 1 km is caused by local AN (52 %) and BB (44 %) emissions (Fig. 6 panel 3d).

It is interesting to note that the CO mixing ratio between 2 and 4 km over Caracas is elevated ( $\geq 150$  ppb) compared to the free tropospheric background ( $\approx 100$  ppb) all year long. The January–July and October maxima are lower than the April one with dominant CO sources being local AN and African (SHAF or NHAF depending on the season) emissions with contributions of 30 % each. In January there is also a small (15 %) influence from AN central and equatorial Asian emissions (CEAS and EQAS). In Bogota, local (71 %) and NHAF (26 %) emissions control the CO annual maxima close to the surface in April, 5d). In the MT and UT, the BB contribution exceeds 80 % because of the strong convection moving over the BB regions (Liu et al., 2010), documented by low OLR (Fig. 2l). The uplifted BB products are trapped in an anticyclonic circulation developed over Central South America (Fig. S3l). CO from Southern Hemisphere South American fires are transported over Bogota, at the edge of the anticyclone, but does not reach Caracas which lies outside of the anticyclone (Fig. 6 panel 4b). During the rest of the year, local AN emissions ( $\geq 60$  %) control the LT CO anomalies. Emissions from Africa are also contributing to LT CO in Bogota with 15 % in July (SHAF and NHAF) and 27 % in January (NHAF). In contrast to Caracas, emissions from SHSA also contribute to LT CO anomalies over Bogota, with 31 % in July and 10 % in October, panels 3d and 4d). Their photochemical processing contributes to the seasonal  $O_3$  enhancement over South America which is the western part of the wave-one pattern (Thompson et al., 2003b; Sauvage et al., 2006). This is highlighted by the collocation of IASI  $UT_{iasi}$  CO (Fig. 2l) and  $O_3$  (Fig. 2p) maxima within the anticyclone.

### 3.1.4 Arabia and Eastern Africa (AEA): Khartoum–Sudan-, Addis Ababa–Ethiopia-, Jeddah–Saudi Arabia-, Abu Dhabi

The striking feature of the AEA clusters is the elevated  $O_3$  in the free troposphere (FT) (70 ppb on average) centered at around 8 km (70 ppb on average) for all the clusters during April and for the northern clusters of Jeddah and Abu Dhabi during July (Fig. 7 panel 1 a–d). The particularly low CO mixing ratio accompanying the  $O_3$  enhancements around 8 km over the AEA clusters (Fig. 7 panel 2a–d) points to a dynamical origin of  $O_3$ . Note that only limited number of profiles are available over Abu Dhabi above 10 km and Khartoum in April. The  $O_3$  enhancements over the 4 sites of AEA and the anticorrelation with CO, are also detected by IASI in the  $UT$  and  $MT_{iasi}$  and  $UT_{iasi}$  (Fig. 2j, k, n and o).

Tropopause foldings in the vicinity of the subtropical jet stream are associated with downward transport of stratospheric ozone (Stohl et al., 2003; Lelieveld et al., 2009; Safieddine et al., 2014) resulting in a tropospheric  $O_3$  enhancement. The  $O_3$

flux from the stratosphere to the troposphere in the vicinity of the NH subtropical jet peaks during spring and summer (Tang et al., 2011). This is in agreement with Cohen et al. (2018) that found the maximum O<sub>3</sub> to CO ratio over the Arabian peninsula during spring and summer for the same seasons (their Fig. A1), using IAGOS data for the period 1994 to 2013. This indicates higher occurrence of O<sub>3</sub>-rich and CO-poor air masses, reflecting a stronger stratospheric influence. Nevertheless, Also, large O<sub>3</sub> regional enhancements are detected by IASI over the Arabian sea similarly to Jia et al. (2017) based on TOC from OMI/MLS. Jia et al. (2017) attributed these O<sub>3</sub> enhancements to emissions from India (50 %), with smaller contributions from the Middle East and Africa (30 %). This is in agreement with SOFT-IO, which shows a significant contribution from SEAS SouthEast Asia over Jeddah (29 %) and a lower one over Addis Ababa (7%) (Figs. 7 panels 4b and 5b, and A2a). SOFT-IO also attributes large contributions from NHAF Northern Hemisphere African AN and BB emissions over Abu Dhabi and to a lesser extent over Khartoum (Fig. 7 panels 3b and 6b). The contribution of American sources over Abu Dhabi indicates eastward transport, which is not present in the rest of the AEA clusters. Due to its northern position, because Abu Dhabi is affected by the subtropical westerly jet in the UT. In contrast the rest of the AEA clusters are affected by the tropical easterly jet which brings CO from Asian regions.

In July, the Middle East summer O<sub>3</sub> maximum is also partly related to subsidence of AMA air masses which brings O<sub>3</sub> produced from South Asian AN and LiNO<sub>x</sub> emissions (Barret et al., 2016). The polluted air masses from South and SouthEast Asia uplifted by monsoon deep convection are trapped in the AMA which extends westward to Northeast Africa and the Middle East (Barret et al., 2016; Park et al., 2007). Over Khartoum and Jeddah (resp. Addis Ababa and Abu Dhabi) 20 ppb (resp. 10 ppb) of CO originates from SEAS SouthEast Asia at 6–12 km. The impact of the SEAS SouthEast Asian emissions is stronger over Jeddah (78 %) than over Khartoum (60 %) and Addis Ababa (46 %) (Fig. A2c). Addis Ababa and Khartoum, further to the south, which are outside of the AMA and therefore characterised by lower levels of O<sub>3</sub> in the UT (Fig. 7 panel 1). Furthermore, the O<sub>3</sub> minimum over Addis Ababa (45–50 ppb) is related to the ITCZ located between 5° N and 10° N during the NH Northern Hemisphere wet season (Lannuque et al., 2021). The UT<sub>iasy</sub> O<sub>3</sub> enhancement over Arabia and the Arabian sea, and the transition to lower concentrations south of the tip of Arabia are also clear with the IASI map IASI (Fig. 2c). The O<sub>3</sub> minimum over Africa is caused by uplift of local African O<sub>3</sub>-poor air masses from the surface in the ITCZ (Fig. 2e), to the ITCZ (Lannuque et al., 2021). The increase of O<sub>3</sub> northwards (such as over Khartoum with 60 ppb; Fig. 7 panel 1d) is due to the O<sub>3</sub> production within uplifted CO-rich air masses, transported away from the ITCZ by the upper branches of the Hadley cell (Lannuque et al., 2021).

One common characteristic among the AEA clusters is the elevated CO mixing ratio in the surface layer (below 1km) all year long (Fig. 7 panel 2). The surface maximum is larger over Addis Ababa (700 ppb in July) and Khartoum (350 ppb in April), than in Jeddah and Abu Dhabi (<250 ppb). Over the East African sites (Khartoum and Addis Ababa), a layer of enhanced CO is observed in the FT below 4 km, in January and April. This winter to spring high CO layer in the FT LT<sub>iasy</sub> over Eastern Africa is detected by IASI which clearly shows that it does not reach Arabia (Fig. 2a–b). IASI data (Fig. 2i–l) also displays little annual UT CO variability over this region.

In January, the surface CO maximum is mostly controlled by local AN emissions over the AEA clusters (Figs. 7 panels 3a to 6a). Above the surface layer, strong Ethiopian AN emissions (Fig. S2) Strong AN emissions from Northern Hemisphere Africa

control the CO anomalies over Addis Ababa with contribution of 71 % in the LT and 58 % in the MT (Fig. A2a). Influence from the ~~NHAF~~ Northern Hemisphere African fires is also evident (12 % in the LT and 20 % in the MT) (Fig. A2a). The impact from ~~the NHAF these~~ fires intensifies over Khartoum and Jeddah between 2 and 4 km with contributions of 58 % and 53 % respectively (Fig. A2a). The effect of the ~~NHAF emissions towards eastern Africa (Khartoum and Addis Ababa) and Northern Hemisphere African emissions towards Eastern Africa and~~ Jeddah is also detected by IASI (Fig. 2a), which shows a negative eastward CO gradient. ~~As expected, the fire contribution is stronger in the western African clusters such as Lagos, due to the prevailing north easterly winds (Fig. S3a) (see Sect. 3.1.1).~~ The co-occurring O<sub>3</sub> enhancement (Fig. 2e) over Khartoum and Jeddah below 4 km reflects O<sub>3</sub> formation during transport from the fires (Fig. 7 panels 1b and 1d). ~~The small enhancement of O<sub>3</sub> is also captured by IASI in the MT (Fig. 2e).~~

In July, the CO surface maximum is again caused by local AN emissions (Fig. 7 panels 3c–5c), except over Khartoum where air masses from ~~SHAF~~ Southern Hemisphere African fires are the dominant source of CO (Fig. 7 panel 6c). The combination of local AN (70 %) and ~~SHAF~~ Southern Hemisphere African BB (23 %) emissions is responsible for the annual CO maximum at the surface over Addis Ababa ~~in July~~ (Figs. 7 panel 5c, and A2a). Interestingly, the impact of the ~~SHAF~~ Southern Hemisphere African fires below 4km over Khartoum and Addis Ababa is stronger than the impact of local fires during the respective dry season (Figs. 7 panels 5ac and 6ac). The O<sub>3</sub> enhancement below 4 km over the Jeddah, Khartoum and Addis Ababa indicates O<sub>3</sub> production during the transport of CO-rich air masses impacted by the ~~SHAF~~ Southern Hemisphere African fires (Fig. 7 panels 1 j to l). In contrast, over Abu Dhabi the O<sub>3</sub> ~~enhancement in the FT~~ enhancements at around 7 and 10 km (Fig. 7 panel 1a) ~~is are~~ likely related to transport of CO-rich air masses from ~~the MIDE and BOAS regions~~ Boreal Asia (Fig. 7 panel 3c).

In October, ~~in the LT the~~ long range transport from Asia (~~SEAS AN and EQAS~~ SouthEast AN and Equatorial BB) plays a significant role in CO anomalies over the AEA sites (Figs. 7 panels 3d–6d), especially over Addis Ababa and Jeddah. In the LT iasy, the northeasterlies (Fig. S3d) ~~transport~~ CO-rich air masses from Asia towards eastern Africa. ~~This transport of CO from Asia over the Arabian sea is well captured as detected~~ by IASI (Fig. 2d).

Above 4km in October, O<sub>3</sub> enhancements are observed over the AEA sites especially over Abu Dhabi which is the eastern-most site of the AEA region (Fig. 7 panel 1). IASI detects a MT iasy O<sub>3</sub> increase above the Arabian sea and Northern India (Fig. 2h). The O<sub>3</sub> enhancement in the MT over the Arabian sea detected with ozone soundings during the INDOEX campaign (1999–2000) has been attributed to Indian sources uplifted over the marine boundary layer by the sea breeze circulation in Lawrence and Lelieveld (2010). ~~It and~~ was further analysed and documented with IASI O<sub>3</sub> data by Barret et al. (2011) ~~who already highlighted the MT O<sub>3</sub> enhancement over northern India and the northern part of the Arabian sea during the post-monsoon season~~. The O<sub>3</sub>-rich air masses are further transported towards Eastern Africa by the prevailing northeasterlies (Fig. S3h) as documented by the predominant ~~SEAS origin of FT~~ SouthEast Asian origin of MT and UT CO over the AEA sites (Figs. 7 panels 3d and 6d).

### 3.2 Control factors of tropical O<sub>3</sub> and CO

~~In this Section we present the main features of the tropical O<sub>3</sub> and CO distributions.~~ Figure 8 displays the annual maximum/minimum of O<sub>3</sub> (a) and CO (b) mixing ratios and their corresponding mean height. The annual maxima/minima are

**Table 2.** Total (AN + BB) CO emission rates (in  $10^{-10} \text{ kg m}^{-2} \text{ s}^{-1}$ ) based on CEDS and GFAS emission inventories over West Africa ( $10^{\circ} \text{ W}$ – $12.5^{\circ} \text{ E}$ ;  $0$ – $12.5^{\circ} \text{ N}$ ), Central Africa ( $10$ – $35^{\circ} \text{ W}$ ;  $2.5$ – $20^{\circ} \text{ S}$ ), East Asia ( $92.5$ – $110^{\circ} \text{ E}$ ;  $10$ – $27^{\circ} \text{ N}$ ), Maritime Continent ( $93$ – $121^{\circ} \text{ E}$ ;  $10^{\circ} \text{ S}$ – $10^{\circ} \text{ N}$ ), South Brazil ( $35$ – $50^{\circ} \text{ W}$ ;  $0$ – $20^{\circ} \text{ S}$ ) and Arabia and Eastern Africa ( $30$ – $60^{\circ} \text{ E}$ ;  $5$ – $25^{\circ} \text{ N}$ ).

	West Africa	Central Africa	East Asia	India	Maritime Continent	South Brazil	AEA
January	6	1	4	3	1.5	1	1.5
April	3	1	11	3.5	1.5	0.5	1
July	2.5	10	3	3	2	1	0.5
October	2.5	3	3	3	6	4	1
Annual	3.5	3.7	5.5	3.1	3	1.5	1

calculated based on monthly averaged mixing ratios over vertical layers with 40 hPa thickness. Figure 9 displays the transport pathways of CO emissions from the African, South American and Asian source regions, towards the 20 tropical sites in the LT (a), MT (b) and UT (c). We show the source regions and the months corresponding to the largest amounts of transported CO (in ppb). Figure 10 displays the AN and BB contribution to CO anomalies (in ppb) over the tropical UT(300–185 hPa)<sub>cruise</sub>.

685 Overall, the CO profiles above all tropical clusters display an annual maximum above the surface layer (approximately at 0.5 km) (Fig. 8b). This is also valid for Caracas, Bogota, Windhoek and Addis Ababa which are located at high altitude above the sea surface (with a mean elevation of 0.9 km, 2.6 km, 1.6 km and 2.3 km respectively). For all the clusters located in the ~~NH-tropics (African, Asian and South American~~NT (except the Gulf of Guinea and Caracas), the CO-polluted boundary layer, is mainly attributed to local AN emissions, even for ~~clusters such as over West Africa~~Lagos and Sahel, 690 where BB is expected to be of great importance (Reeves et al., 2010; Mari et al., 2008; Sauvage et al., 2005) (Figs. 4a; A2a; A3a). (Reeves et al., 2010; Mari et al., 2008). This finding confirms the key role of ~~the~~AN emissions in the ~~NH~~Northern Hemisphere, related to larger population compared to the ~~SH~~Southern Hemisphere, and enhanced AN urban and industrial activity, ~~as discussed in Edwards et al. (2004)~~. Concerning the ~~SH~~ST, the surface-layer pollution is predominantly caused by BB over ~~SH~~ST Africa (Central Africa and Windhoek) during the dry season (Figs. 4, A2), and by AN over the SBrazil (Fig. 695 A2). Interestingly, ~~the~~The CO maxima over the latter occurs before the burning season. This is in accordance with previous studies suggesting fossil fuels as the main CO source over Sao Paulo and Rio de Janeiro (Alonso et al., 2010), and decreasing BB over South America (Andela et al., 2017; Deeter et al., 2018). ~~The decrease of BB CO emissions is~~ due to the long-term declining deforestation rates, especially over forested areas ( $\approx 54\%$ ) and over savanna and shrublands ( $\approx 39\%$ ) (Naus et al., 2022). The importance of the AN emissions is also evident over Central Africa~~with non-negligible contributions during dry~~ 700 ~~season (10%) (Fig. 4). Also, the,~~ where a polluted surface layer ~~over Central Africa~~ is present all year long, ~~with large AN contributions of 40% and 86% and~~ during the transition seasons, when the fires are suppressed~~, it is largely caused by AN contributions (40% and 86% in April and October;~~ Fig. 4a). Thus, the impact of the AN emissions is also important in the ~~SH~~ST.

The CO maxima show strong variations in terms of magnitude and season among the tropical clusters. ~~This is~~ because they are mostly caused by local emissions with varying intensity and seasonal pattern, depending on the region. In contrast, the CO minima are uniform in terms of intensity levels of mixing ratios, close to the CO background levels of ~~100 ppb~~, due to mixing and transport over the lifetime of CO. As expected, they occur in the ~~FT~~ MT or UT, in the absence of the emissions and where CO is chemically destroyed. As for the CO maxima, their strong seasonality is related to the seasonality of the surface emissions and the meteorological conditions, which differ over each region. Further discussions on the magnitude and the seasonality of the CO maxima and minima will follow later.

Because of its complex chemistry, the situation for O<sub>3</sub> is more complicated. Africa is the only region where the annual O<sub>3</sub> maximum occurs in the LT (at 2.5 km) during the dry season (Fig. 8a Sahel, Guinea Gulf, Lagos and Central Africa). The co-occurrence of maximum O<sub>3</sub> with the maximum in CO over Africa during the local fires indicates stronger dependency of O<sub>3</sub> on the surface AN and BB CO emissions for these regions, in agreement with Sauvage et al. (2007b). South China is the only Asian cluster where the annual O<sub>3</sub> maximum is observed in the LT (at 2.6 km) during the active local fires (April), ~~but it is not accompanied by the annual CO maximum (Fig. 8), suggesting that the ozone maximum has been formed differently.~~ In contrast, over the other regions, the annual O<sub>3</sub> maximum is observed ~~in the FT~~ above 6 km (Fig. 8a). This ~~likely~~ indicates that O<sub>3</sub> is ~~formed by photochemical processes, and is likely~~ associated with larger ozone production efficiency in the MT and UT (Sauvage et al., 2007c). In regions such as Arabia (Jeddah and Abu Dhabi), the lack of CO enhancement in the UT indicates dynamical origin of O<sub>3</sub> (e.g. stratospheric influence and transport of O<sub>3</sub> and precursors from Asia; see Sec. 3.1.4). In contrast, in regions such as SBrazil and Windhoek in October, the co-occurrence of O<sub>3</sub> and CO enhancement in the MT and UT indicates ~~tropospheric origin for~~ O<sub>3</sub> production from surface sources (e.g. fires ~~and LiNO<sub>x</sub> emissions;~~). In addition, LiNO<sub>x</sub> emissions can contribute to O<sub>3</sub> production at higher altitudes (Secs. 3.1.1 and 3.1.3). The annual O<sub>3</sub> minima for all the tropical clusters are observed close to the surface (below 0.5 km on average) (Fig. 8a). This is ~~related to the chemical and deposition sinks of~~ O<sub>3</sub> located in the LT likely related to deposition and titration by NO (see Sect. 3.1.1 for more details).

The highest CO and O<sub>3</sub> maxima among all the tropical clusters occur over ~~NH~~ NT Africa in the LT (at 0.3 km for CO and 2.5 km for O<sub>3</sub>) during the dry season (January) mostly due to local AN emissions. ~~According to IASI (Fig. 2), the CO-rich and O<sub>3</sub>-rich air masses due to the African emissions show a large extend along the tropical Equatorial Africa, and accumulate in the LT due to the stability of the Harmattan winds (Sauvage et al., 2005) (over Lagos and Sahel) and BB (over Guinea Gulf).~~ Table 2 displays the total (AN and BB) CO emissions rates over several regions of interests based on the sum of CEDS and GFAS emission inventories. ~~Indeed, the O<sub>3</sub> and CO maxima co-occur with the highest emissions over Western Africa in January, confirming their strong dependency on the surface emissions.~~ The NO<sub>x</sub>-limited O<sub>3</sub> production regime over Western Africa (Saunois et al., 2009; Zhang et al., 2016) likely explains the O<sub>3</sub> maxima when the local emissions, and thus the NO<sub>2</sub> concentration (Jaeglé et al., 2004), intensify in the region. The largest O<sub>3</sub> and CO mixing ratio over Lagos (Fig. 8) is due to its proximity to the strong Nigerian AN emissions, as confirmed by SOFT-IO (see Sect. 3.1.1). ~~As expected, the impact on CO is higher in the proximity of the emissions, while the CO mixing ratio decreases downwind (towards Sahel and Gulf of Guinea) (Fig. 8) because of physical processes, such as dilution by mixing and entrainment (Martin et al., 2017), and CO consumption in O<sub>3</sub> build-up in fires (Chatfield et al., 1996).~~ The O<sub>3</sub> maxima show smaller variations (of approximately 10 ppb) among the



NH-NT African clusters. In contrast to CO, the O<sub>3</sub> enhancement does not strongly depend on the proximity to emissions, as it is produced during the transport and chemical ageing of air masses rich in precursors (Sauvage et al., 2007b).

The second highest CO and O<sub>3</sub> maxima over the tropical regions are observed over Asia (Fig. 8). ~~As in NH Africa, the CO maximum occurs in January, when the stability of the trade wind results in accumulation of CO-rich air masses in the LT. The surface-layer CO maximum is attributed to local AN emission over Indian and South China clusters (85–95 %). In the rest of the Asian cluster, there are non-negligible contributions from regional AN sources of the Asian cluster in addition to the dominant local ones, mostly due to AN emissions.~~ According to Table 2, the CO emissions over East Asia and India are lower than the ones over Western Africa in January. This explains the lower CO mixing ratio over Asia than over Lagos. SOFT-IO seems to represent better the Asian contributions ~~relative to the Africa~~ than the African ones. As mentioned in Sect. 3.1.1, the AN emissions over NH and SH Africa are likely underestimated by the SOFT-IO computations (Fig. 3 panels 3b and 4b). This is confirmed by that fact that CO mixing ratio is higher over Africa than over Asia, in contrast to the CO contributions estimated by SOFT-IO. ~~Thus, the impact of the African AN emissions is likely underestimated.~~

Previous studies have already found concentrations of pollutants in West Africa (e.g. Lagos, Abidjan, Cotonou) comparable to those observed over Asian megacities (Assamoi and Liousse, 2010; Adon et al., 2016; Sauvage et al., 2007b). ~~Indeed, the~~ The rapid growth over African megacities is responsible for increasing emissions from diffuse and inefficient combustion sources (Marais and Wiedinmyer, 2016). ~~This increase is mostly attributed to the growing residential source, such as residential sources~~ mainly for cooking and heating (Zheng et al., 2019), but also to and traffic emissions (related to large number of two-stroke vehicles, poor fuel quality and poorly-maintained engines) (Assamoi and Liousse, 2010). In contrast, Eastern China has had one of the largest decreases in CO emissions (Hedelius et al., 2021) due to technological changes with improved combustion efficiency ~~and emission control measures (Zheng et al., 2018a). Using MOPPIT data for the period 2002–2018, Buchholz et al. (2021) found the largest reduction in CO concentrations over China. This reduction is attributed to declines in local CO emissions since 2002, related to (Zheng et al., 2018a), such as~~ replacing residential coal use with electricity and natural gas ~~, and to the (Buchholz et al., 2021), and~~ implementation of Clean Air Policies (van der A et al., 2017) around 2010. In India, on the other hand, there are no regulation in the emissions, and this explains the highest CO mixing ratios among the Asian clusters (Fig. 8). Previous studies have already reported increasing CO emissions over India from 1996–2015, due to several factors such as increases in residential and agricultural sources (Pandey et al., 2014) and to power production and transport activities (Sadavarte and Venkataraman, 2014).

As in NH-NT Africa, the CO-rich air masses accumulated in the LT over the Asian clusters in January ~~result in are~~ accompanied by a secondary LT O<sub>3</sub> maximum. However, these maxima are significantly lower (40–60 ppb) (Sect. 3.1.2) than the NH-NT African ones (65–75 ppb) (Fig. 8a; Sect. 3.1.1), even for clusters with similar LT CO mixing ratios (e.g. Sahel and South China) (Fig. 8a). This is because: i) the CO emissions are less strong over the Asian clusters, as mentioned before, and ii) the O<sub>3</sub> enhancement over Asia is caused by AN-polluted air, while in NH-NT Africa by mixed (AN and BB) polluted air. During the Atom campaign, Bourgeois et al. (2021) found that O<sub>3</sub> levels are more enhanced in mixed air pollution, because they are associated with greater NO<sub>x</sub> and peroxy acyl nitrates (a NO<sub>x</sub> reservoir compound), and thus increased O<sub>3</sub> production,

in comparison to BB- or AN-polluted air alone. This is in agreement with the O<sub>3</sub> annual maximum in April over East Asia (Fig. 8a), over clusters such as South China and Bangkok, which are affected by the local fires.

775 ~~Unlike Africa, the~~ The highest emission rates over East Asia and India are observed in April (Table 2). In the absence of the stability of the north easterlies, the air masses are not confined close to the surface like in January, ~~and thus the secondary CO maxima above the surface is also captured by IASI (Fig. 2f).~~ Over East Asia, the contribution of the local fires is ~~also~~ present in addition to the local AN emissions. The impact of the fires dominates in the MT in clusters such as South China and Bangkok, and is evident over Manila and Ho Chi Minh City (see Sect. 3.1.2). Interestingly, the NH Northern Hemisphere  
780 African fires in January correspond to 72 % of the global burned area, whereas the NH Northern Hemisphere Asian fires only to the 2.5 % (Van der Werf et al., 2010). However, both regions contribute significantly to the global CO concentrations (44 % for Africa and 22 % for Asia) because of more complete oxidation, and thus reduced CO production, over grass fires (Africa savannas), relative to fires in forests and peatlands (deforestation and peatland fires over Asia) (Van der Werf et al., 2010). The large extend of the impact of the NH Northern Hemisphere Asian fires is displayed in IASImap, with an outflow towards SE  
785 Asian coast and the Pacific (Fig. 2f). The stronger winds in April than in January, ~~which does not favour the accumulation of the pollution,~~ and the eastwards transport pathway (Fig. 9 panel 1 a–b) leads to lower CO mixing ratio in April ~~than January,~~ despite the higher emission rates (Table 2).

Concerning India, local AN emissions are responsible for the CO enhancement in April, with negligible BB contribution (Figs. 5 panel 3a and A1 panels 3a and 4a). ~~The CO emissions rates over India are high during the whole year, showing weak seasonal variability (Table 2). The LT CO distribution~~ According to IAGOS and IASI (Figs. 2a–d, 5 panel 1ab), the LT CO  
790 ~~over India shows strong seasonal variability which is not cannot be explained by the seasonality of the emissions. The LT CO weak variations of the Indian emissions (Table 2). This indicates that LT CO over India~~ is rather linked with seasonal changes in the meteorological circulation. Similarly to East Asia, during January the air masses are transported southward due to the north easterlies, while the reversal of the winds to southwesterlies in July results in northward transport (Figs. 2 and S3)  
795 (Lawrence and Lelieveld, 2010). Because of this circulation pattern in July, the oceanic influence brings clean air masses over the Asian clusters resulting in an annual CO minimum during the Asian summer monsoon (Fig. 8). The CO-rich air masses for the surface are uplifted in the upper troposphere due to deep convection over the area (Sect. 3.1.2).

As for CO, O<sub>3</sub> seasonality is also linked with the seasonality of the meteorological conditions and dynamics over Asia. The O<sub>3</sub> maximum in April is attributed to the intense solar radiation associated with important amount of precursors from mostly  
800 AN emissions, except for South China where BB emissions dominate. The O<sub>3</sub> minimum occurs during the ~~asian~~ Asian summer monsoon (July), because of lower O<sub>3</sub> production in the presence of convective clouds relative to clear sky conditions (Sect. 3.1.2).

Despite the CO emissions reductions over South China, the O<sub>3</sub> levels remain relatively high (Fig. 8a). This is because the O<sub>3</sub> production regime over South China is VOCs-limited (Li et al., 2013), and the total NMVOCs emissions increased ~~in China~~  
805 ~~by a factor of 3.5 (1997–2017) because of activity increases in the solvent, energy, and industry sectors (Zheng et al., 2018a). As discussed in Wang et al. (2017), despite~~ Despite the successful controls of NO<sub>x</sub> emissions from coal fired power plants since 2010 over Eastern China (Wang et al., 2017), it is recommended to apply controls over VOCs emissions as they control

the local O<sub>3</sub> distribution. In contrast, over India the O<sub>3</sub> production regime is NO<sub>x</sub>-limited (Kumar et al., 2012), as the local emissions are mostly associated with incomplete combustion processes by biofuel burning, and thus higher NMHC to NO<sub>x</sub> emission ratio as compared to other regions of the Northern Hemisphere (Lawrence and Lelieveld, 2010).

Concerning Central Africa, the O<sub>3</sub> and CO maximum in the LT during the dry season, indicates the strong dependence of the CO and O<sub>3</sub> distribution on the surface emissions, as over NH-NT Africa. The CO magnitude over Central Africa is similar to the one over Sahel and Guinea Gulf during the respective dry season, even though the emissions rates are higher over the former (Table 2). This is because higher amount of CO impacted by the SH-Southern Hemisphere African fires is transported towards the NH-NT Africa due to the trade winds, relative to the respective southward transport during the NH Northern Hemisphere dry season (Fig. 9). In addition, the O<sub>3</sub> mixing ratio is slightly higher over Central Africa (85 ppb) likely indicating rapid photochemical O<sub>3</sub> production by BB precursors (Singh et al., 1996) during the SH-fires. ~~Concerning Windhoek, the O<sub>3</sub> maximum in the FT (85 ppb at 10 km) (Fig. 8) indicates that O<sub>3</sub> production is controlled by LiNO<sub>x</sub> emissions at higher altitude (Sauvage et al., 2007b) during the peak of the lightning activity over South Africa (Fig. not shown).~~ Southern Hemisphere fires.

The smallest LT CO maximum over the NH-NT are observed over Arabia and East Africa clusters and South America (Fig. 8) because of the smallest emissions rates among the tropics (Table 2). The CO emissions over Middle East are mainly related to electricity generation, water desalination, and industry supplied by oil and gas deposits with cheap but relatively clean fuels (Krotkov et al., 2016). In addition, because of its location between the two highest emitters (Asia and Africa), transport plays a significant role in CO enhancements over AEA, especially in the MT and UT where long range transport of emissions is favoured (Figs. 9 panels 1 b–c; 2 a–c and 2b–c). This transport from Asia and Africa over AEA clusters determines the O<sub>3</sub> maxima over the AEA clusters (Sect. 3.1.4). Similarly, over NH-NT South America, the local AN contributions are much smaller than the respective local Asian or African ones, indicating lower pollution levels over South America than Asia and Africa. The O<sub>3</sub> maximum is controlled by LiNO<sub>x</sub> emissions at higher altitudes.

From the previous analysis, all the tropical clusters and the associated CO source regions exhibit primarily local influence, in the proximity of the region where they are emitted. However, CO transport plays also an important role in the CO distribution over the tropics. CO sources located over Africa show the maximum influence on the regional tropical CO. The highest impact of the African emissions is found at an inter-hemispheric scale, where CO from the dry-season African regions is transported towards the wet-season African (Fig. 9 panels 1 and 2). As a result, CO contributions of 45–50 ppb (resp. over 50 ppb) from NHAF-Northern Hemisphere (resp. SHAF-Southern Hemisphere) Africa is found over SHAF-Southern (resp. NHAF-Northern) Africa during the respective dry season in the LT and MT. ~~This transport of precursors results in a secondary O<sub>3</sub> maximum, as can be seen by IASI maps (Fig. 2e and g).~~

~~Impact of the SHAF BB in July is also found in the LT over India with contributions of 5–10 ppb (Fig. 9 panel 2a). Similarly, NHAF AN and BB contributions in January are found over South America (5–10 ppb in the MT) and India (5–10 ppb in the MT and UT) (Fig. 9 panel 1a). The impact of the NHAF emissions~~ Also, Northern Hemisphere African emissions are transported towards South America (10–15 ppb in MT; 5–10 ppb in the rest) ~~is increased~~ in April (Fig. not shown) and significantly

~~contributes~~ contribute to the local South American annual maximum (30 % and 50 % of CO anomalies over Caracas (LT and MT resp.) (Fig. 4a–b).

845 During the transport of the ~~SHAF–Southern~~ (resp. ~~NHAF–Northern~~) Hemisphere African emissions towards the ITCZ location in the ~~North–Northern~~ (resp. ~~South–Southern~~) Africa, the air masses reach convective regions and are injected in the ~~North–African–(resp. South–African)–upper–troposphere–(UT<sub>cruise</sub>)~~ (Fig. 10). This explains why the ~~SHAF–Southern~~ (resp. ~~NHAF–Northern~~) Hemisphere African emissions are dominant in the wet-season hemisphere during July (resp. January) (Figs. 10 and resp. A6 and A4). Nevertheless, the ~~NHAF–Northern Hemisphere African~~ contribution in the UT<sub>cruise</sub> CO anomalies is present on a local scale all year long, above ~~NH–NT~~ Africa and South Atlantic. During the dry season, the impact of the ~~NHAF~~ Northern Hemisphere African emissions is stronger and extends to a wider area over South America, Middle East, South Asia  
850 (Figs. A4 NHAF).

~~The impact of CO emissions from South America is extended over South Africa during October. This is because of the anticyclone over Central South America which traps the CO emitted locally, and transports it towards the east by westerlies (see Sect. 3.1.3). The highest transport in terms of CO amount from NHSA and SHSA occurs in the MT (10–15 ppb each). IASI maps show an O<sub>3</sub> and CO enhancement over the tropical South Atlantic (Figs. 2 d and h, 2l and p). Thus, the South American emissions mostly coming from BB (Figs. 10, A7 SHSA and NHSA) contributes to the wave-one pattern. Nevertheless, the most important source of O<sub>3</sub> over the tropical South Atlantic is LiNO<sub>x</sub> emissions from South America and South Africa, as highlighted by previous studies (Sauvage et al., 2007b, e).~~

855

~~The~~ contribution of Asian emissions in the tropical LT is limited to a regional or local scale, as they are mostly impact  
860 neighbour Asian regions (Fig. 9a)(see Sect. 3.1.2 for more details). CO export from Asia is favoured during the Asian summer monsoon and post monsoon (July and October) in the UT, where the transport is favoured due to stronger winds relative to the surface (Fig. S3).

During the Asian summer monsoon, the CO-rich (and O<sub>3</sub>-poor) air masses from the ~~PBL–boundary layer~~ (Fig. 2c and g) are convectively uplifted in the UT<sub>cruise</sub> (Figs. 10c and A6), and trapped in the AMA circulation (see Sect. 3.1.2). ~~The impact of the Asian emissions on the UT CO anomalies is extended over~~ Asian emissions are transported towards Arabia (25–30 ppb) and Eastern Africa (~~25–30 ppb~~) 10–15 ppb in the UT<sub>cruise</sub> (Figs. 10c; 9 panel 3c and A6 SEAS and CEAS). ~~Interestingly, subsidenee–Subsidence~~ of air masses from AMA above Arabia are responsible for an O<sub>3</sub> maximum above AEA (Fig. 8a) (Sect. 3.1.4). During the post monsoon season (October), sporadic convection uplifts CO emitted by ~~EQAS fires~~ the Equatorial Asian fires in the UT<sub>cruise</sub> (Figs. 10g, A7 EQAS) (see Sect. 3.1.2). At the same time, convection over continental Asia uplifts  
870 ~~SEAS–SouthEast Asian~~ AN emissions (Figs. 10d and A7 SEAS) in the UT<sub>cruise</sub>. As a result, CO from the Asian emissions impacts CO anomalies in the UT over Eastern Africa ~~with EQAS contribution of (15–20 ppb, and SEAS contribution of from Equatorial Asia and~~ 5–10 ppb (~~from SouthEast Asia~~; Fig. not shown).

#### 4 Summary and conclusions

IAGOS O<sub>3</sub> and CO observations since 1994 and 2002 respectively, were used (when available) in order to analyse vertical profiles over 20 tropical sites, along with the ~~(lower part) of UT<sub>cruise</sub>~~. One limitation of our study is the rather limited spatial coverage of IAGOS profiles to limited locations. However, according to Petetin et al. (2018a), a few hundreds meters above the ground, these measurements are representative of the urban background and of the upper tropical troposphere. IAGOS data combined with global 2D distributions based on IASI-SOFRID regional scale at higher altitudes in the lower troposphere. Furthermore, IASI, which provides global daily O<sub>3</sub> and CO retrievals since 2008, were used in order to study the characteristics and seasonal variability of the tropical tropospheric O<sub>3</sub> and CO distributions –with a coarse vertical resolution, allows us to complement IAGOS observations on the global scale over the data sparse tropical band. Throughout the paper we have shown that the anomalies detected by IAGOS are often also detected by IASI at the regional scale.

In the LT, the CO anomalies ~~over the tropics~~ are caused by a combination of AN and BB emissions. In the majority of the clusters, local AN contributions are dominant all year long. The BB contribution increases or dominates over some clusters, when the regional or local fires are active. Local AN emissions have greatest impact over Asia where they account for more than 80 % of the CO. The BB impact increases over South China (35 % in April), and dominates over the Gulf of Thailand (90 % in October) during the local fires (~~SEAS and EQAS SouthEast and Equatorial Asian~~ resp.). Over NH ~~Africa, local AN contributions are~~ NT Africa, with contributions in the range of ~~60–85 % all year, except July. During the SH dry season, CO impacted by the SHAF fires is transported northwards contributing significantly to LT CO anomalies over NH Africa (53–66 %over Lagos~~ 57-85% local AN emissions largely dominate the CO anomalies all year long. There are a few exceptions of larger BB contributions in January over Guinea Gulf (53%) and in July over Lagos (53%) and Guinea Gulf (66%) during Northern and Southern Hemisphere African BB seasons. Similar impact of the ~~SHAF Southern Hemisphere African~~ fires is found over Khartoum in July. In contrast, the rest of the ~~Arabian and Eastern Africa AEA~~ clusters are impacted by local AN emissions all year long (70–95 %). Over South America, stronger local AN contribution are found over the ~~SH-ST~~ (81–94 % over SBrazil) than in the ~~NH-NT~~ (75–80 % Caracas and Bogota), while the ~~contributions from the local fires~~ BB contributions are similar (51 % over Caracas in April and 53 % over SBrazil in October). The highest BB impact is found over ~~SH Africa during the NH and SH dry season with contributions of 60 and 90 % respectively. As expected, the local BB dominate the LT CO anomalies during the ST Africa all year long (57%–90%), except in April, with BB emissions mostly originating from local fires, however there is important transport from the NHAF. Despite the fact that BB dominates over SH Africa during the dry seasons, the AN emissions are important during the transition periods but also from Northern Hemisphere Africa in January (45-73%) and Southern Hemisphere Southern America in October (29% over Windhoek).~~ During the transition periods, the local AN contributions are larger (46 and 80 %). Our results highlight the importance of the AN emissions over the ~~tropiestropical sites~~, even in the ~~SHST~~. This is in accordance with the global decreasing trends of BB (~~Andela et al., 2017~~) and the increasing AN emissions (~~Granier et al., 2011~~).

In the MT and UT, the BB contributions are increased compared to the LT, and their effect dominates over more clusters. Also, the contribution of the transport is more important than in the LT, where mostly local emissions dominate. Over ~~NH-NT~~

Africa, the BB dominates twice a year, during the ~~NH and SH~~ Northern and Southern Hemisphere dry seasons, because of local and ~~SHAF~~ Southern Hemisphere African fires respectively. In ~~SH-NT~~ Africa, as in the LT, BB dominates all year long except April. In addition to the African BB, AN ~~SEAS and BB SHSA~~ SouthEast Asian and BB Southern Hemisphere South  
910 American contributions are found in the MT and UT. Over Asia, ~~BB from SEAS in April, exceeds the AN contribution over the SE~~ SouthEast Asian BB contributions dominate over the South East Asian coast (South China, Manila, Ho Chi Minh City) in April in the MT. In contrast, the ~~EQAS BB effect~~ impact of the Equatorial Asian BB is stronger in the UT, ~~extending over SE and has a largest spatial extent over the South East~~ Asian coast (China, Ho Chi Minh City, Manila) ~~and~~, India (Madras) ; but also and Eastern Africa (Addis Ababa).

915 Over Africa, the O<sub>3</sub> and CO maxima are observed in the ~~low troposphere~~ LT during the respective dry season. The role of the local AN emissions are more important than previously ~~noted (Reeves et al., 2010; Mari et al., 2008; Sauvage et al., 2005)~~ documented as: i) local AN emissions ~~define the O<sub>3</sub> and control the~~ CO anomalies over ~~NH Africa~~ Lagos and Sahel, and ii) the persistent CO-rich surface layer in Central Africa is caused by local AN emissions (40 and 86 %) in the absence of ~~the~~ local fires. Africa is also the most important tropical region in terms of export of emissions in the tropical troposphere. According  
920 to IASI ~~horizontal distributions~~, the main export pathway is the inter-hemispheric transport of O<sub>3</sub> and precursors from the dry-season African regions to the wet-season ones ( $\approx 50$  ppb), confirmed by SOFT-IO ~~contributions~~. During the dry season, the ~~NHAF~~ Northern (resp. ~~SHAF~~ Southern) Hemisphere African fires are the dominant source of CO over AEA (resp. Khartoum and Jeddah) in the MT and UT, and they also reach India accounting for ~~5–10~~ 5–10 ppb in the MT and UT. Transport of mostly BB emissions from ~~NHAF and SHAF~~ Africa occurs all year round towards northern South America in all tropospheric  
925 layers. The highest ~~NHAF~~ Northern Hemisphere African regional impact is found over Caracas in the MT and UT (30 % on average). In contrast, the impact of Asian emissions, is mostly limited on a regional or local scale, especially in the LT and MT. The transport of the Asian emissions is important only during the Asian summer monsoon in the UT towards Arabia and ~~NH~~ Eastern Africa.

The highest ~~abundances of the O<sub>3</sub> (75 ppb) and CO mixing ratio (800 ppb) and CO maxima~~ among the tropical clusters  
930 ~~are found over Northern Hemisphere Africa at about~~ occur in the LT of NT Africa in January (75 ppb at 2.5 km altitude for O<sub>3</sub> and 800 ppb at 0.3 km for CO over Lagos). This is largely a result of the local AN emissions as suggested by the co-occurrence of the peaks of ~~O<sub>3</sub>~~ O<sub>3</sub> and CO in the LT. In contrast over Asia, the second most polluted region, the distributions are mostly controlled by meteorological conditions associated with the Asian monsoon phase. The CO maximum occurs in the LT during January, due to the stability of the northeasterlies which confine the CO-rich air masses to the LT. ~~In contrast, The~~  
935 ~~annual maximum of O<sub>3</sub>~~ O<sub>3</sub> occurs during the pre monsoon season (April) when the increased solar radiation favours ~~O<sub>3</sub>~~ O<sub>3</sub> production. During the Asian summer monsoon, O<sub>3</sub> and CO mixing ratio minimize in the ~~low troposphere~~ LT because of : i) transport of clean oceanic air above continental Asia, ii) reduced photochemical O<sub>3</sub> production due to cloudy conditions, and iii) convective uplift of CO-rich air masses from the surface towards the Asian upper troposphere.

Over Asia, the LT and MT CO and O<sub>3</sub> anomalies are mostly impacted by regional or local Asian emissions of AN origin. The  
940 BB contribution is important during April and significantly contributes to ~~O<sub>3</sub> and~~ CO anomalies over South China. According to IASI, the BB impact extends over the tropical Pacific. The ~~impact export~~ of the AN Asian emissions is important only in

the UT during the Asian summer monsoon and post monsoon season (July and October). According to IASI, the polluted air masses from the surface are uplifted in the UT cruise in July and are trapped in the AMA. These air masses are transported over ~~Arabia and Northern Africa~~ AEA (CO contributions of 25–30 ppb and 10–15 ppb) causing the annual O<sub>3</sub> maxima due to subsidence and high isolation over the regions. This highlights the importance of long range transport for the air quality in the UT over Arabia, which shows the lowest CO local contribution and the highest O<sub>3</sub> levels among the tropical clusters. The CO transport towards Eastern Africa in the UT by the Tropical Easterly Jet, is found in October when the air masses impacted by the Indonesian fires, and the AN continental source are uplifted in the UT, and transported towards Eastern Africa (CO contributions of 15–20 ppb and 5–10 ppb respectively).

950 Last, over South America the local CO contributions at the surface level are as low as over Arabia and Eastern Asia. During the dry season (October), when the convection moves over the South American fires, CO and precursors are trapped in an anticyclonic circulation developed over Central South America, resulting in the annual local maxima of O<sub>3</sub> and CO. The ~~transatlantic~~ transport of O<sub>3</sub> and precursors over ~~the~~ Atlantic can be seen by IASI and this contributes to the O<sub>3</sub> wave-one pattern (~~Sauvage et al., 2007e~~). This is confirmed by SOFT-IO which calculates Northern and Southern Hemisphere South  
955 American contribution of 10–15 ppb ~~from SHSA and 10–15 ppb NHSA~~ each towards Windhoek, in the altitude of the anticyclone (MT).

~~Overall, the importance of anthropogenic emissions is highlighted over the tropics, not only in the NH but also in SH. The interconnections among the tropical regions, especially transport of O<sub>3</sub> and precursors originating from Africa, makes it necessary to assess the pollution on a local scale in order to improve air quality on a local and region scale over the tropics.~~

## A1 Vertical profiles

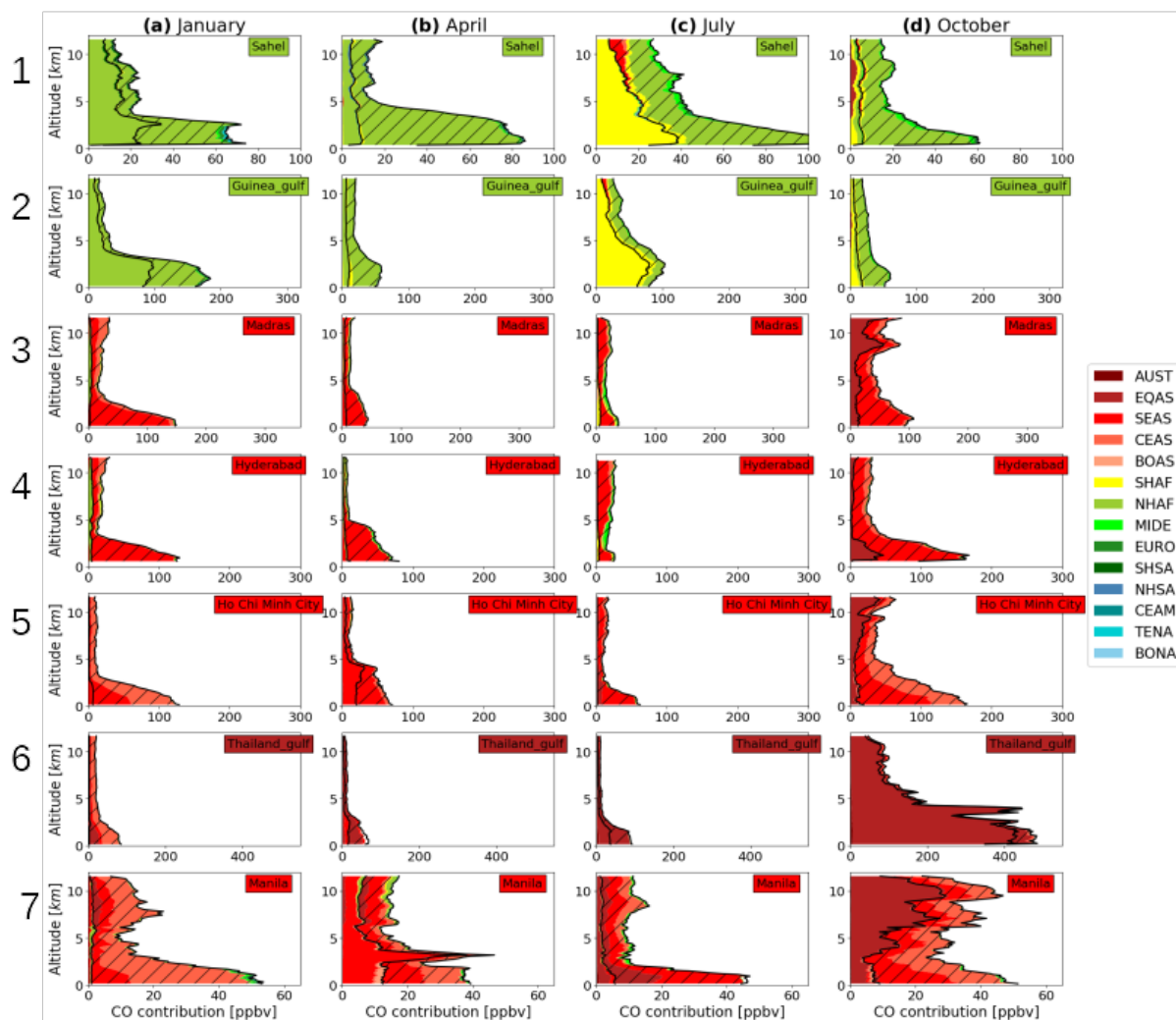


**Figure A1.** Same as Fig. 3 (panel 3) for CO contributions over Sahel (1), Gulf of Guinea (2), Madras (3), Hyderabad (4), Ho Chi Minh City (5), Gulf of Thailand (6) and Manila (7).



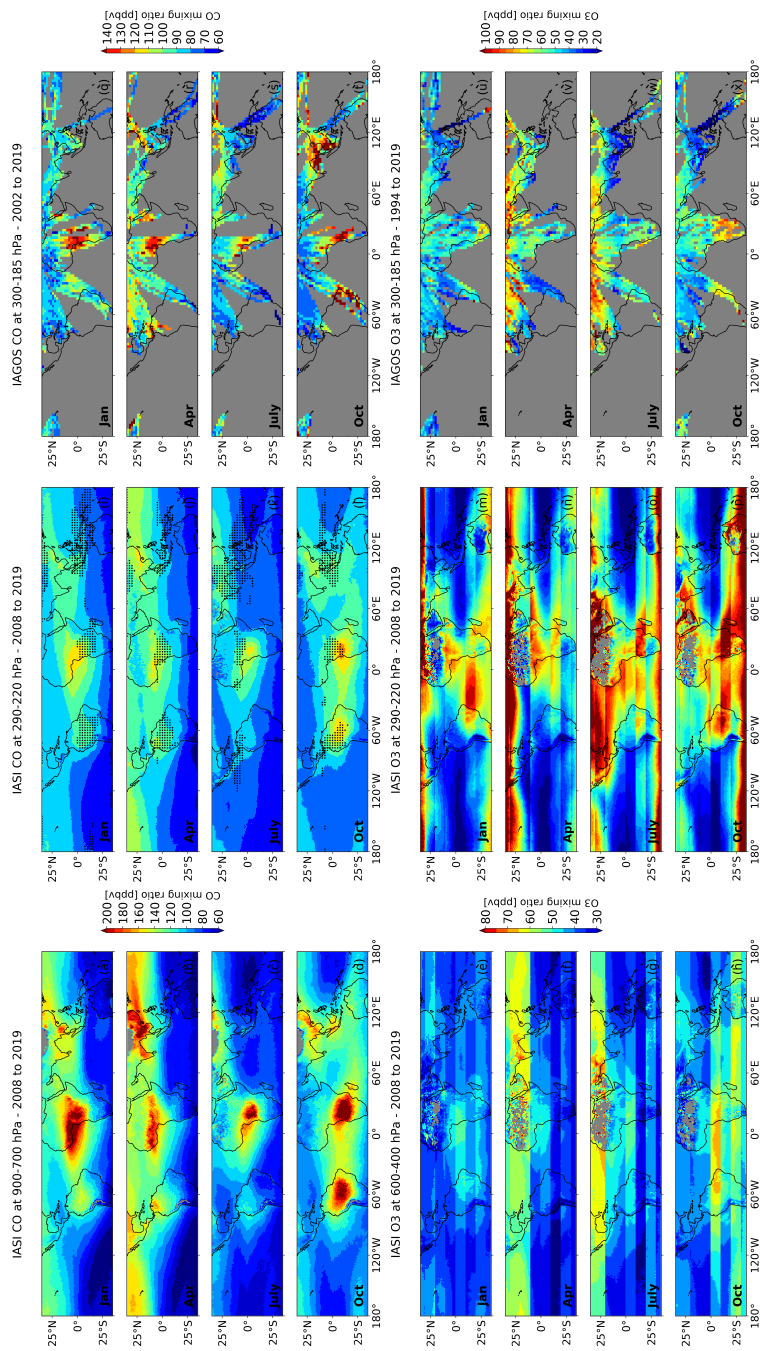


**Figure 2.** Monthly mean LT-low tropospheric IASI CO distributions (900–700 hPa; a–d), MT-mid tropospheric IASI O<sub>3</sub> distributions (600–400 hPa; e–h), UT-upper tropospheric CO distributions based on IASI (i–l) and IAGOS (q–t), UT-O<sub>3</sub> distributions based on IASI (290–220 hPa; i–l and m–p resp.) and IAGOS (300–185 hPa; q–t and u–x resp.).

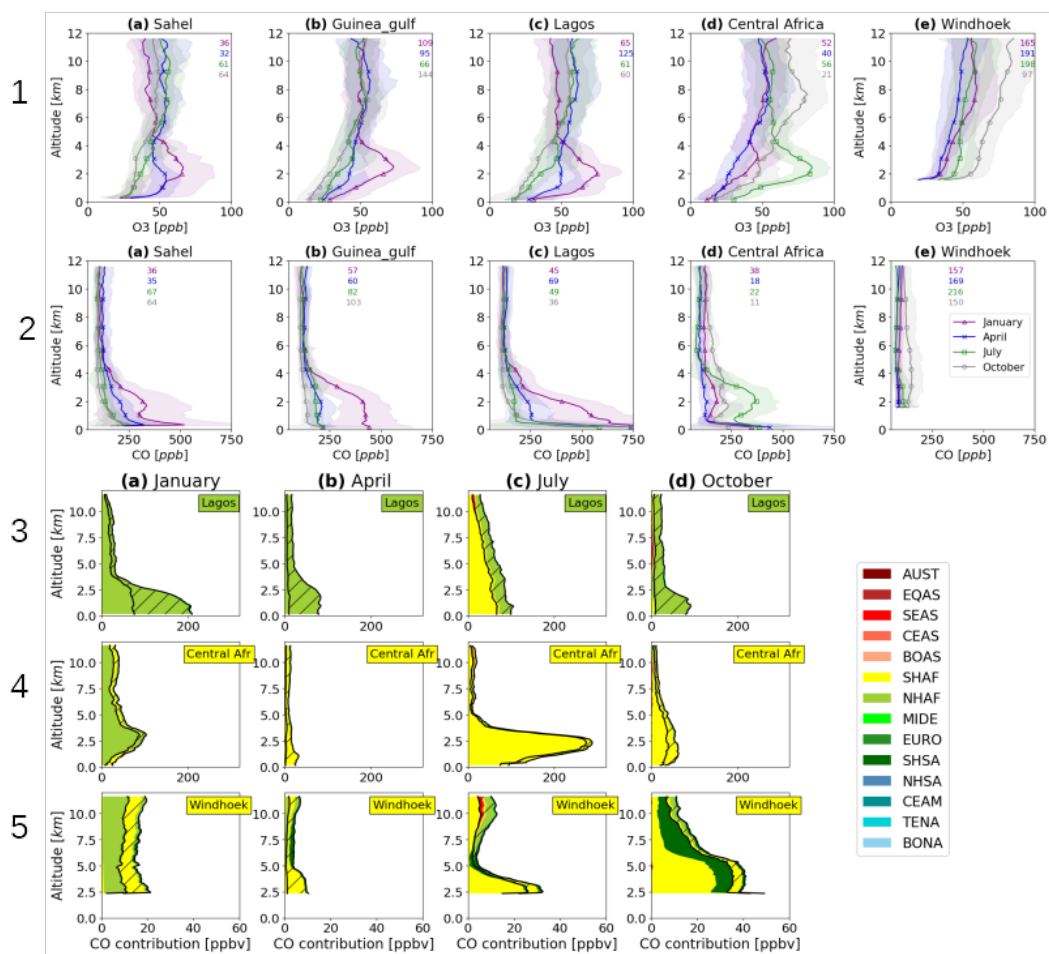


**Figure 3.** IAGOS monthly mean O<sub>3</sub> (panel 1) and CO (panel 2) vertical distributions. The annotated numbers correspond to the total number of flights per month for the IAGOS period, given in the same colour as in the legend. The shadowed part corresponds to  $\pm 1$  one standard deviation. Vertical distribution of CO contributions (in ppbv) (panels 3 to 5) with the hatched part showing AN contribution, and the non-hatched part BB contribution. For clarity reasons the CO contribution for Sahel and Gulf of Guinea are displayed in Fig. A1.

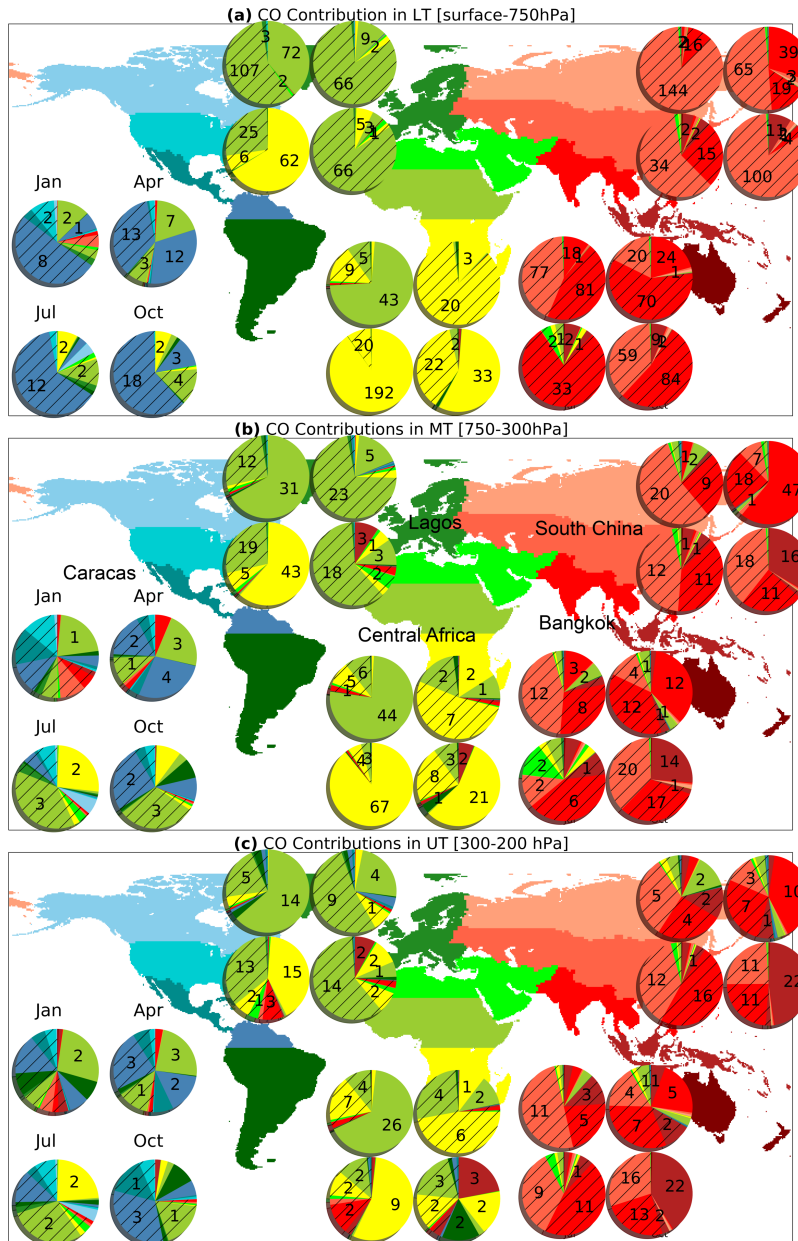


**Figure 4.** Mean SOFT-IO contributions (in ppb), averaged over all the positive CO anomalies for the tropical sites (Caracas, Lagos, Central Africa, South China and Bangkok) for LT (a), MT (b) and UT (c) for the AN (hatched) and BB (unhatched) contributions. Each pie corresponds to a different month and each group of four pies refer to a different site (see panel b).

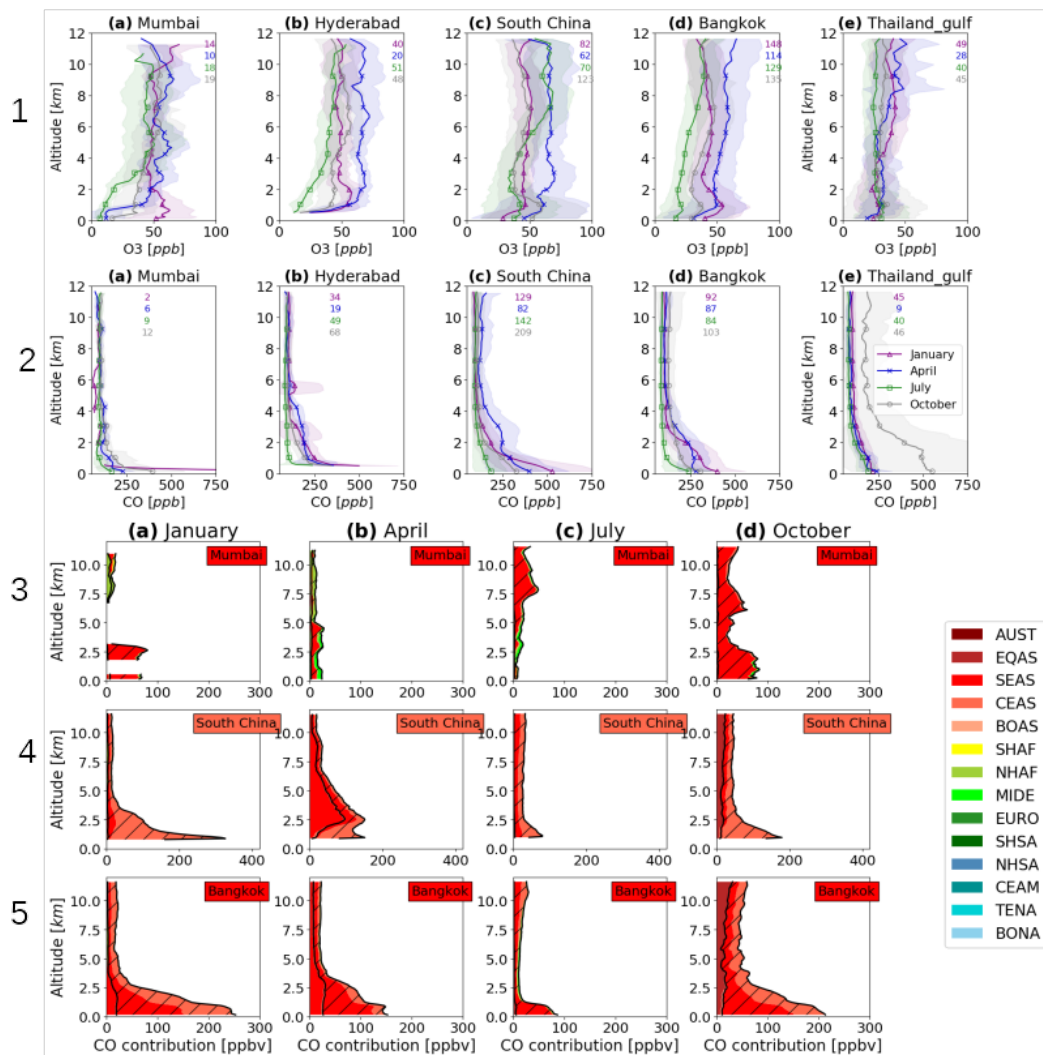


Figure 5. Same as Fig. 3 for the Asian clusters.

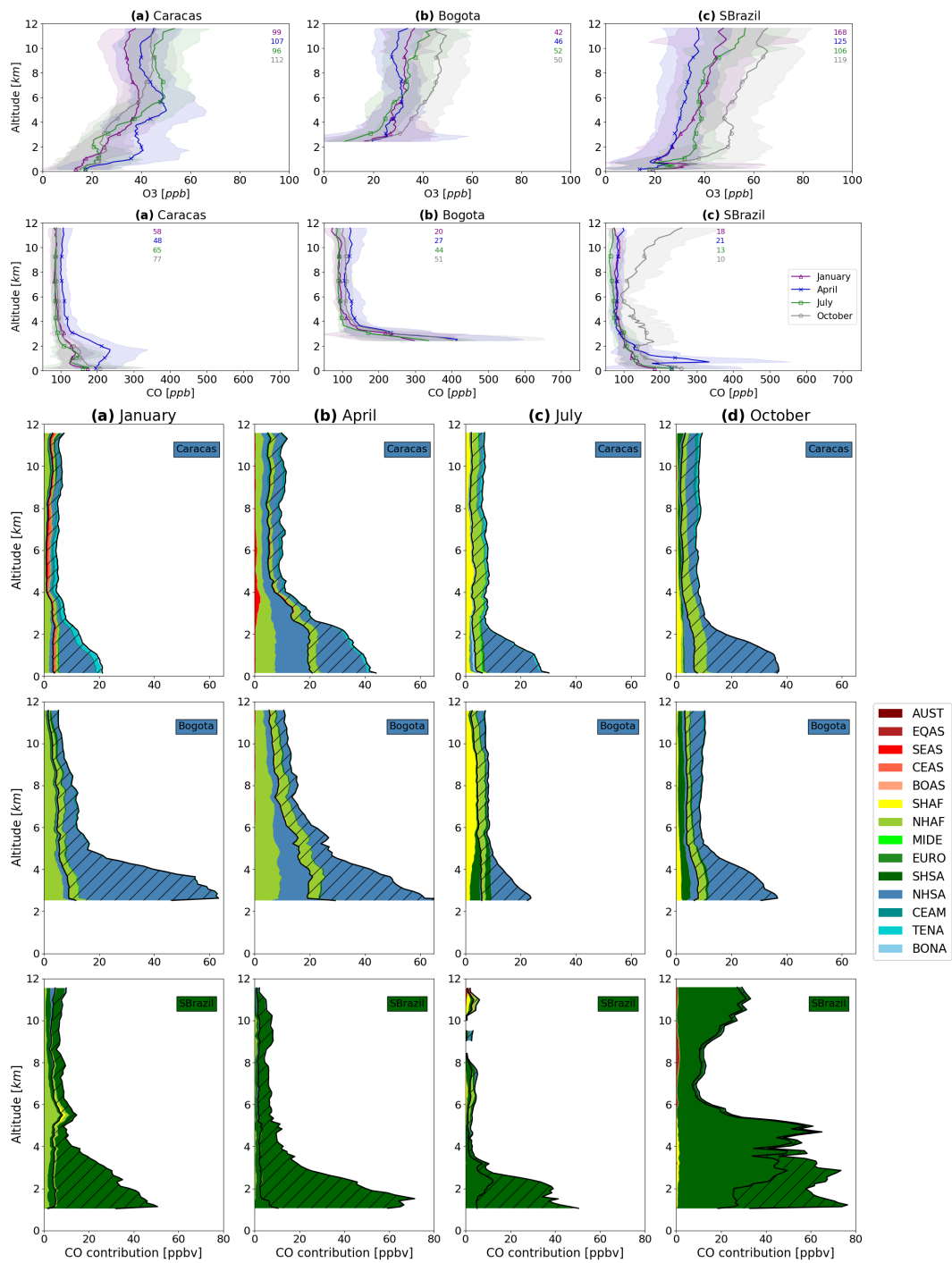
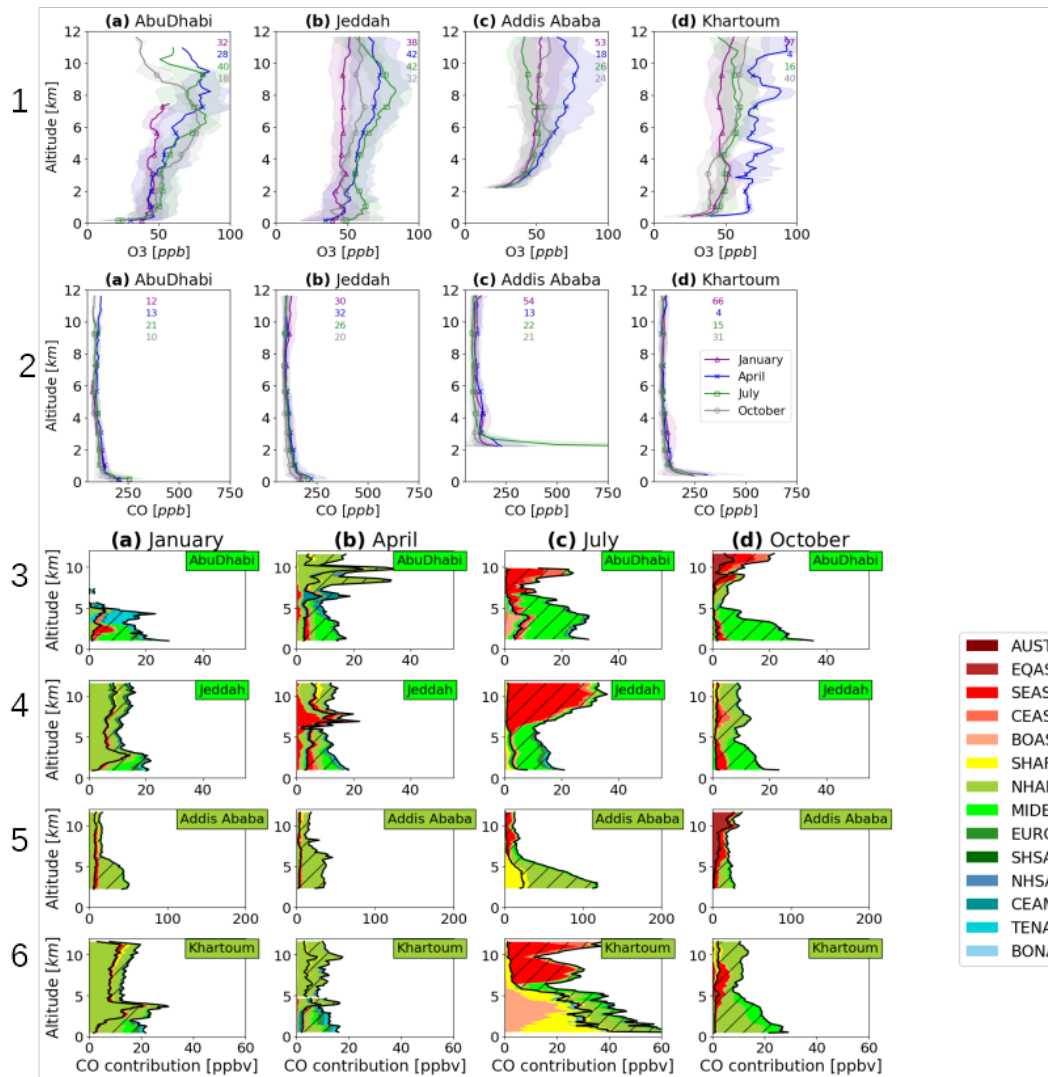
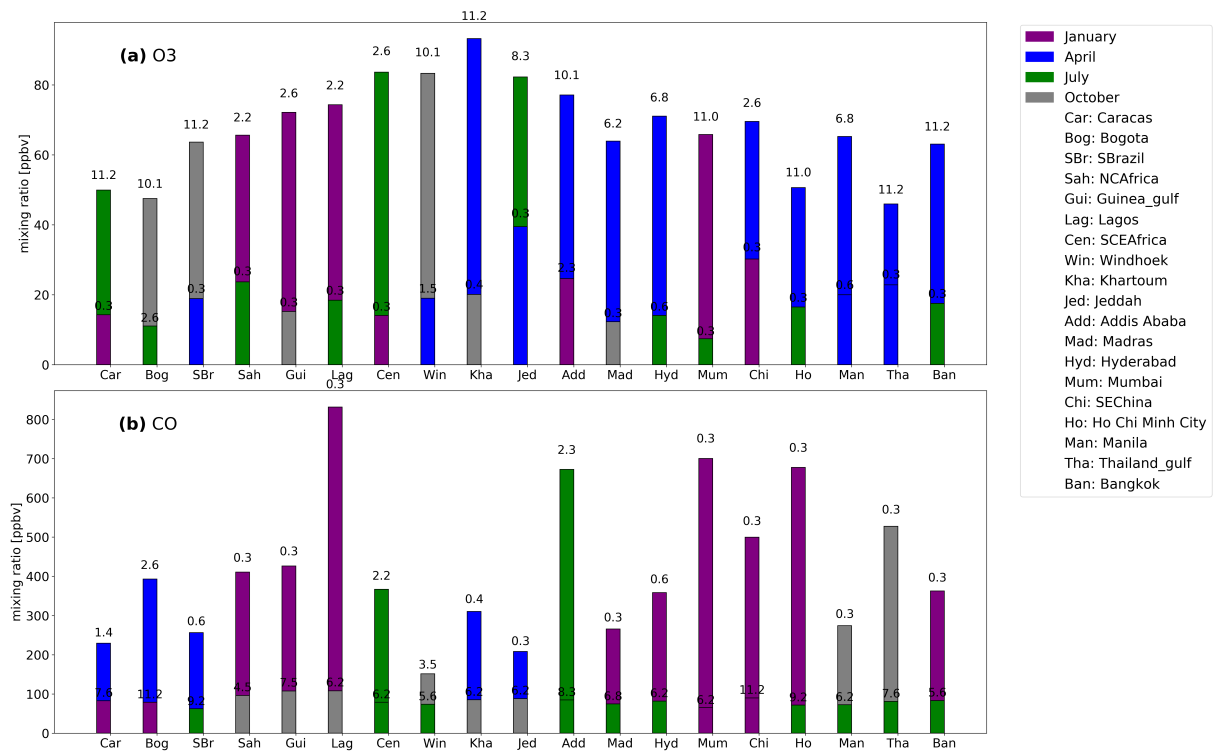


Figure 6. Same as Fig. 3 for the South American clusters.



**Figure 7.** Same as Fig. 3 for the Arabian and Eastern African clusters.



**Figure 8.** O<sub>3</sub> (a) and CO (b) annual maximum (higher bar) and minimum (lower bar) mixing ratio observed over the tropical clusters. The annotated number on top of each bar indicates the altitude (in km) of the observed annual maximum/minimum mixing ratio. The colour in the bar indicates the month of the maximum/minimum.

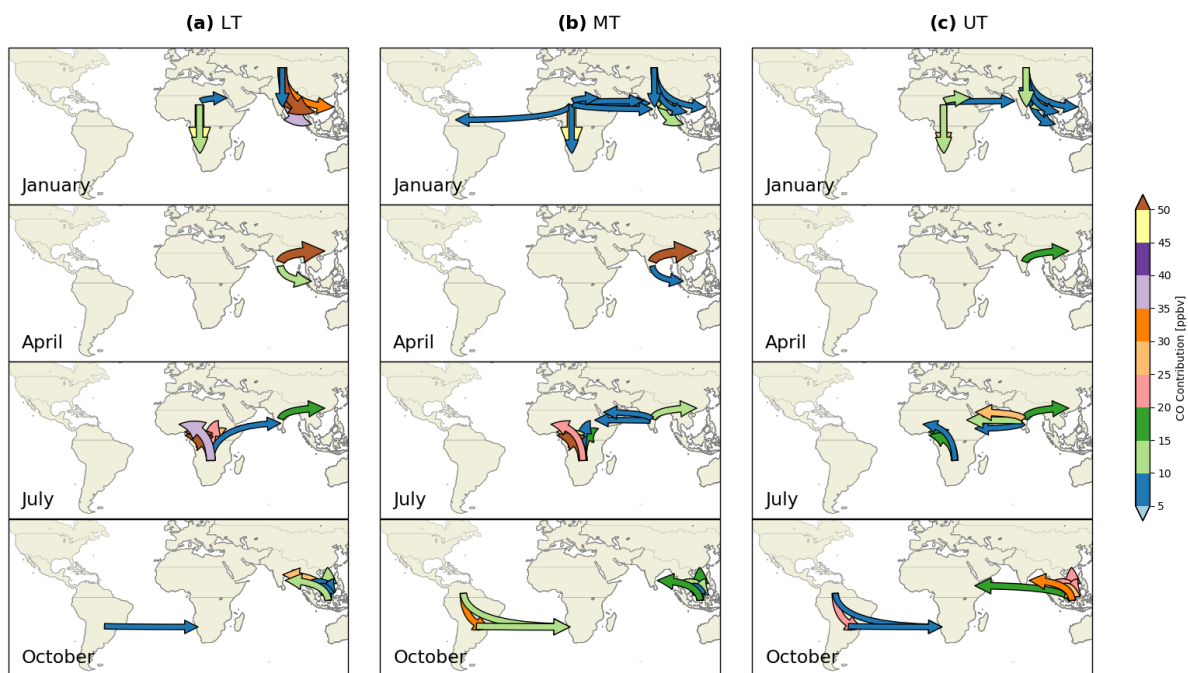


**Figure 9.** Transport of CO (AN+BB) emissions from the African, South American and Asian source regions towards the 20 tropical sites taken into account for this study. The colorbar shows the amount of CO transported in ppb.

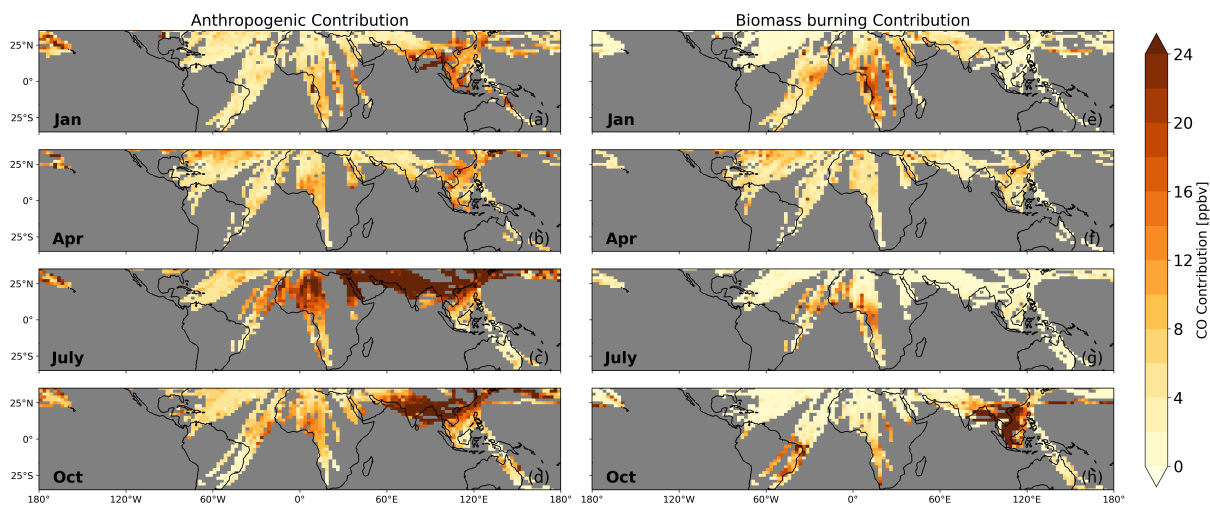


**Figure 10.** Mean AN (a-d) and BB (e-h) contributions in ppb over the tropical upper troposphere (between 300-185 hPa) from 2002-2019.



# A1 Low, mid and upper troposphere

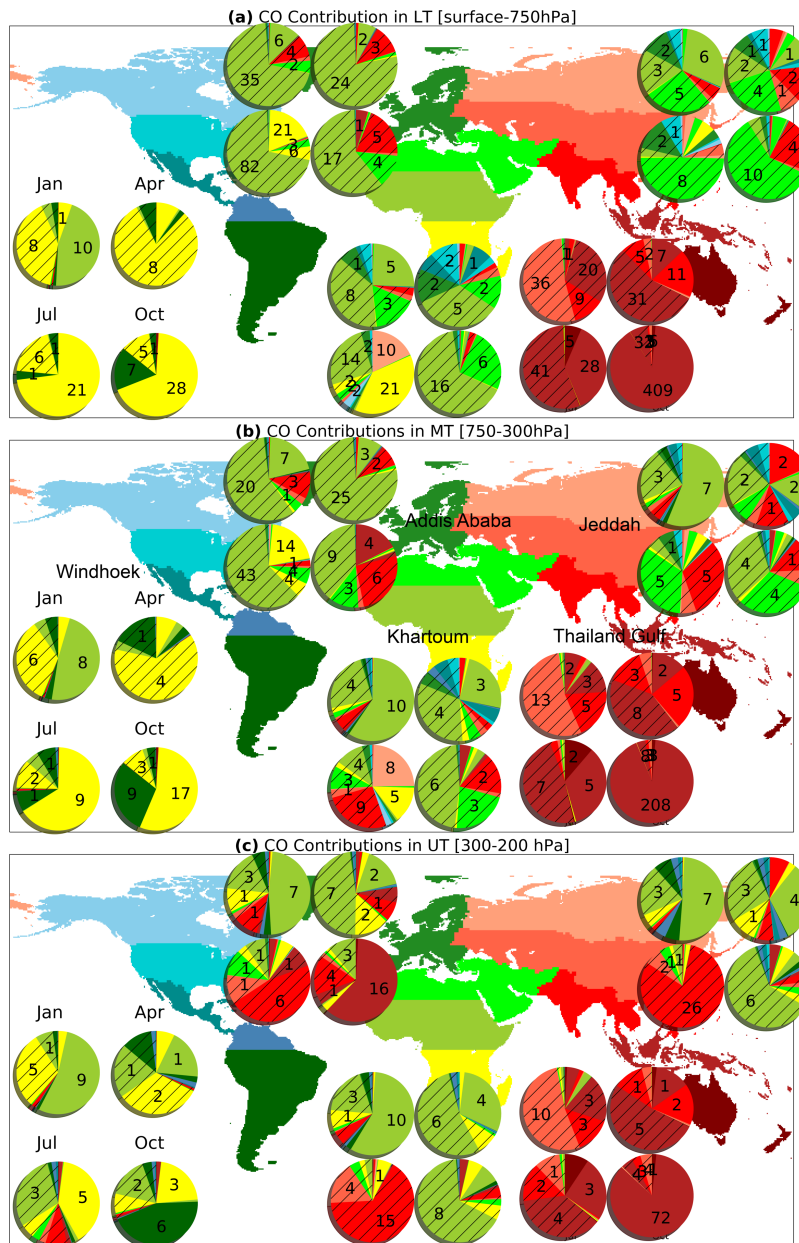
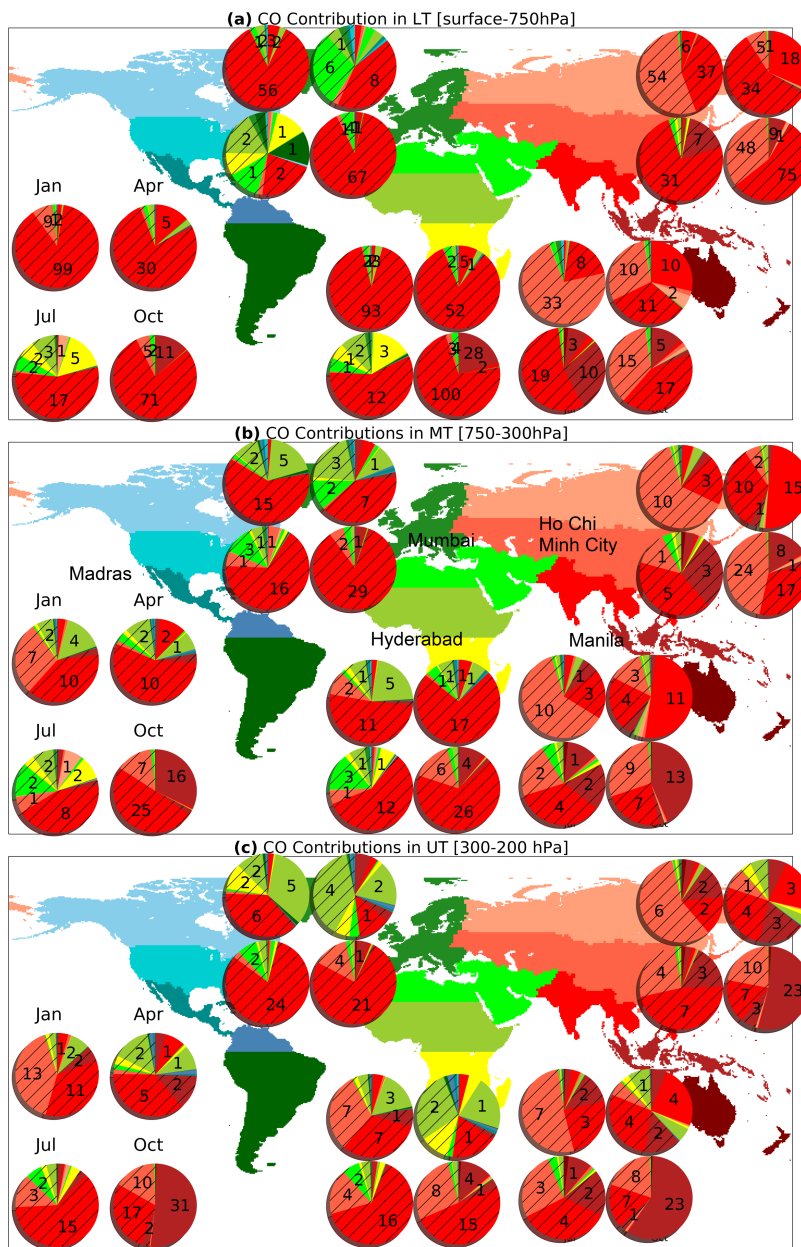


Figure A2. Same as Fig. 4 for CO contributions over Windhoek, Addis Ababa, Khartoum, Jeddah and Gulf of Thailand.



**Figure A3.** Same as Fig. 4 for CO contributions over Madras, Mumbai, Hyderabad, Ho Chi Minh City and Manila.

## A2 Upper troposphere

January

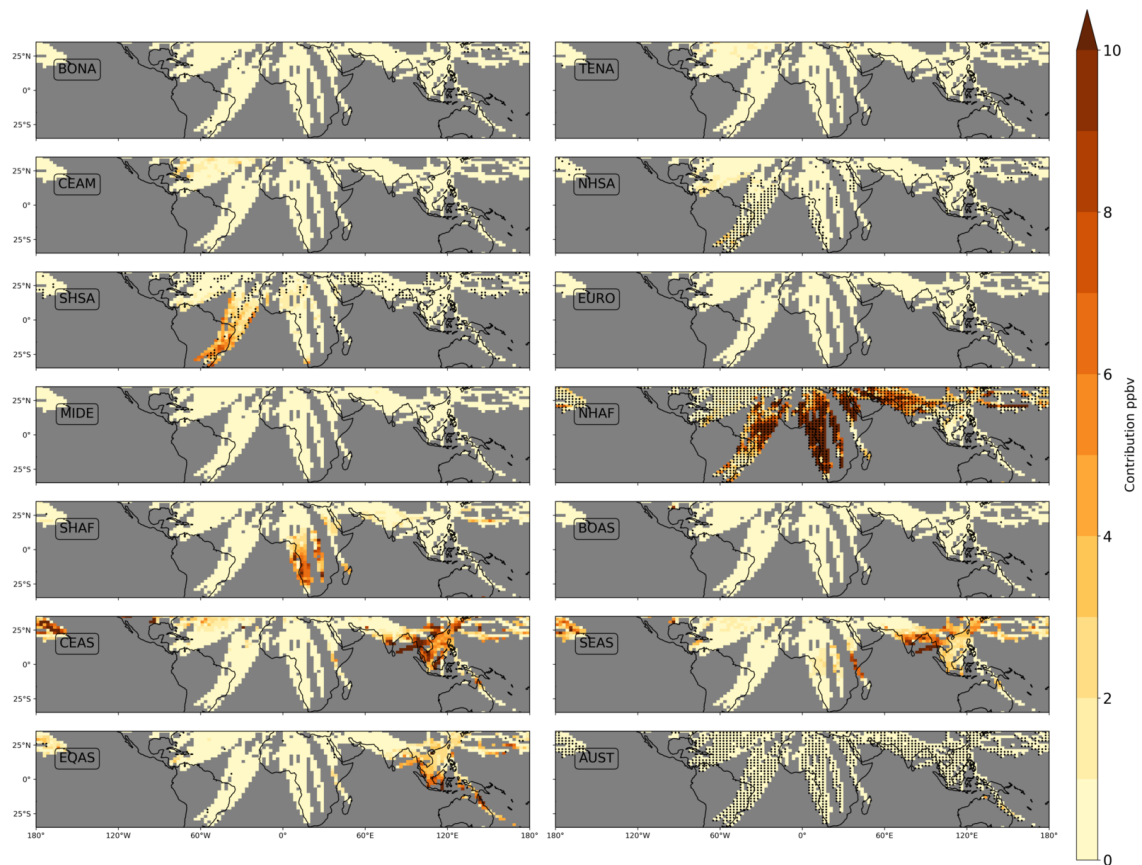


**Figure A4.** Mean CO contribution (in ppbv) per source region in the tropical UT<sub>cruise</sub> (300–185 hPa) averaged from ~~2002–2019~~ 2002–2020 for January. The hatched part indicates BB as the dominant source of CO.

April

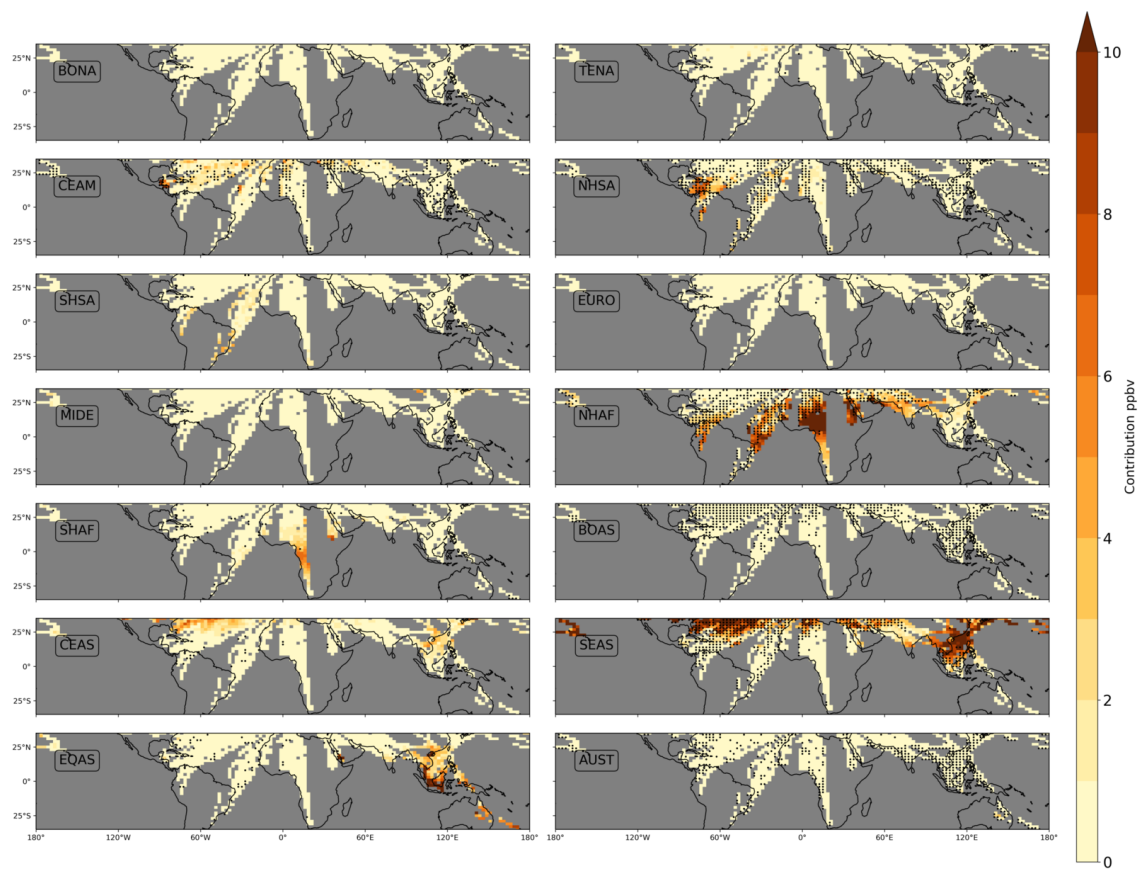


**Figure A5.** Same as Fig. A4 for April.

July

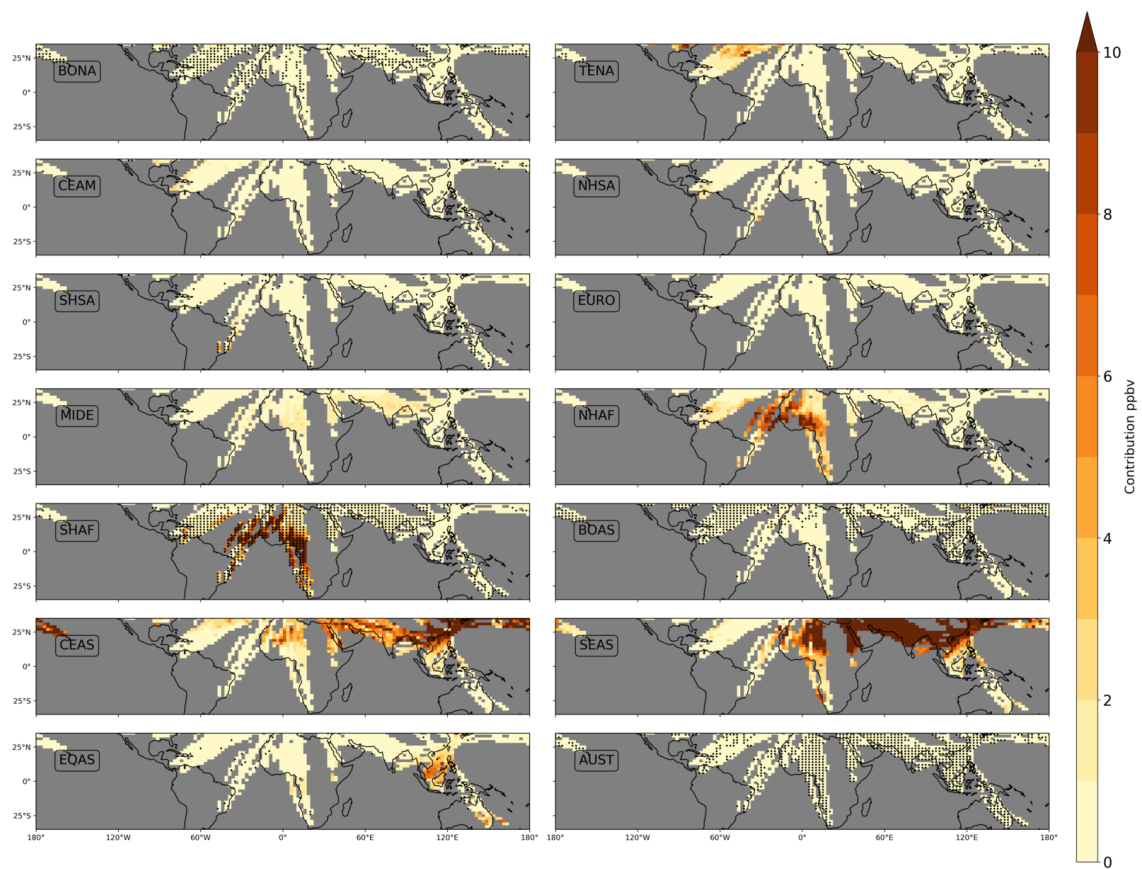


**Figure A6.** Same as Fig. A4 for July.

October

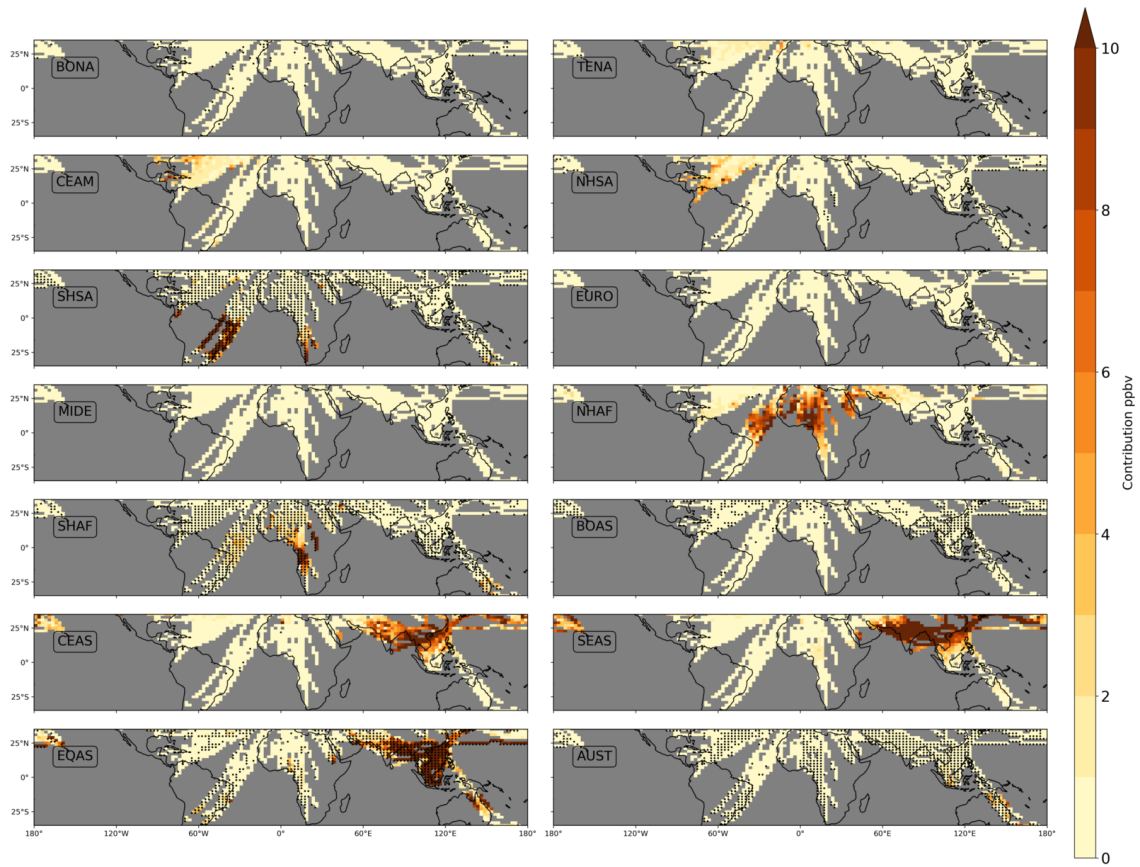


**Figure A7.** Same as Fig. A4 for October.

*Data availability.* The IAGOS data are available on the IAGOS data portal (<https://doi.org/10.25326/20>). The SOFT-IO v1.0 products are  
965 part of the ancillary products of IAGOS central database (<https://doi.org/10.25326/2>; <https://doi.org/10.25326/3>). The SOFRID-O<sub>3</sub> data are  
freely available on the IASI-SOFRID website (<http://thredds.sedoo.fr/iasi-sofrid-o3-co/>, last access: 8 June 2022; SEDOO, 2014).

*Author contributions.* MT, BS and BB designed the research. All the co-authors contributed to acquisition of data. MT analysed the data.  
MT, BS and BB interpreted the data. MT drafted the article. MT, BS and BB revised the article. VT and HC commented the article. ELF and  
BB are responsible for the SOFRID retrieval software. ELF is in charge of the production and quality control of SOFRID data.

970 *Competing interests.* The authors declare that they have no conflict of interest.

*Acknowledgements.* We acknowledge the strong support of the European Commission, Airbus and the airlines (Deutsche Lufthansa, Air  
France, Austrian, Air Namibia, Cathay Pacific, Iberia, China Airlines and Hawaiian Airlines) that have carried the MOZAIC or IAGOS  
equipment and performed the maintenance since 1994. IAGOS has been funded by the European Union projects IAGOS–DS and IA-  
GOS–ERI. Additionally, IAGOS has been funded by INSU-CNRS (France), Météo-France, Université Paul Sabatier (Toulouse, France) and  
975 Research Center Jülich (FZJ, Jülich, Germany). The IAGOS database is supported in France by AERIS (<https://www.aeris-data.fr>). IASI is a  
joint mission of EUMETSAT and the Centre National d’Etudes Spatiales (CNES, France). The authors acknowledge the CNES for financial  
support for the IASI activities.

*Financial support.* This research has been supported by Bonus Stratégique programme at Université Paul Sabatier Toulouse III who funded  
the first author’s doctoral position.

980 **References**

- Adon, M., Galy-Lacaux, C., Yoboué, V., Delon, C., Lacaux, J., Castera, P., Gardrat, E., Pienaar, J., Al Ourabi, H., Laouali, D., et al.: Long term measurements of sulfur dioxide, nitrogen dioxide, ammonia, nitric acid and ozone in Africa using passive samplers, *Atmospheric Chemistry and Physics*, 10, 7467–7487, <https://doi.org/10.5194/acp-10-7467-2010>, 2010.
- Adon, M., Yoboué, V., Galy-Lacaux, C., Liousse, C., Diop, B., Gardrat, E., Ndiaye, S. A., Jarnot, C., et al.: Measurements of NO<sub>2</sub>, SO<sub>2</sub>, NH<sub>3</sub>, HNO<sub>3</sub> and O<sub>3</sub> in West African urban environments, *Atmospheric Environment*, 135, 31–40, <https://doi.org/10.1016/j.atmosenv.2016.03.050>, 2016.
- Aghedo, A. M., Schultz, M. G., and Rast, S.: The influence of African air pollution on regional and global tropospheric ozone, *Atmospheric Chemistry and Physics*, 7, 1193–1212, <https://doi.org/10.1016/j.atmosenv.2016.03.050>, 2007.
- Alonso, M. F., Longo, K. M., Freitas, S. R., da Fonseca, R. M., Marécal, V., Pirre, M., and Klenner, L. G.: An urban emissions inventory for South America and its application in numerical modeling of atmospheric chemical composition at local and regional scales, *Atmospheric Environment*, 44, 5072–5083, <https://doi.org/10.1016/j.atmosenv.2010.09.013>, 2010.
- Andela, N., Morton, D. C., Giglio, L., Chen, Y., van der Werf, G. R., Kasibhatla, P. S., DeFries, R. S., Collatz, G., Hantson, S., Kloster, S., et al.: A human-driven decline in global burned area, *Science*, 356, 1356–1362, <https://doi.org/10.1126/science.aal4108>, 2017.
- Archibald, A., Neu, J., Elshorbany, Y., Cooper, O., Young, P., Akiyoshi, H., Cox, R., Coyle, M., Derwent, R., Deushi, M., et al.: Tropospheric Ozone Assessment Report A critical review of changes in the tropospheric ozone burden and budget from 1850 to 2100, *Elementa: Science of the Anthropocene*, 8, <https://doi.org/10.1525/elementa.2020.034>, 2020.
- Assamoi, E.-M. and Liousse, C.: A new inventory for two-wheel vehicle emissions in West Africa for 2002, *Atmospheric Environment*, 44, 3985–3996, <https://doi.org/10.1016/j.atmosenv.2010.06.048>, 2010.
- Barret, B., Ricaud, P., Mari, C., Attié, J.-L., Bousserrez, N., Josse, B., Le Flochmoën, E., Livesey, N., Massart, S., Peuch, V.-H., et al.: Transport pathways of CO in the African upper troposphere during the monsoon season: a study based upon the assimilation of spaceborne observations, *Atmospheric Chemistry and Physics*, 8, 3231–3246, <https://doi.org/10.5194/acp-8-3231-2008>, 2008.
- Barret, B., Williams, J., Bouarar, I., Yang, X., Josse, B., Law, K., Pham, M., Le Flochmoën, E., Liousse, C., Peuch, V., et al.: Impact of West African Monsoon convective transport and lightning NO<sub>x</sub> production upon the upper tropospheric composition: a multi-model study, *Atmospheric Chemistry and Physics*, 10, 5719–5738, <https://doi.org/10.5194/acp-10-5719-2010>, 2010.
- Barret, B., Le Flochmoen, E., Sauvage, B., Pavelin, E., Matricardi, M., and Cammas, J.-P.: The detection of post-monsoon tropospheric ozone variability over south Asia using IASI data, *Atmospheric Chemistry and Physics*, 11, 9533–9548, <https://doi.org/10.5194/acp-11-9533-2011>, 2011.
- Barret, B., Sauvage, B., Bennouna, Y., and Le Flochmoen, E.: Upper-tropospheric CO and O<sub>3</sub> budget during the Asian summer monsoon, *Atmospheric Chemistry and Physics*, 16, 9129–9147, <https://doi.org/10.5194/acp-16-9129-2016>, 2016.
- Barret, B., Emili, E., and Le Flochmoen, E.: A tropopause-related climatological a priori profile for IASI-SOFRID ozone retrievals: improvements and validation, *Atmospheric Measurement Techniques*, 13, 5237–5257, <https://doi.org/10.5194/amt-13-5237-2020>, 2020.
- Barret, B., Gouzenes, Y., Le Flochmoen, E., and Ferrant, S.: Retrieval of Metop-A/IASI N<sub>2</sub>O profiles and validation with NDACC FTIR data, *Atmosphere*, 12, 219, <https://doi.org/10.3390/atmos12020219>, 2021.
- Blot, R., Nedelec, P., Boulanger, D., Wolff, P., Sauvage, B., Cousin, J.-M., Athier, G., Zahn, A., Obersteiner, F., Scharffe, D., et al.: Internal consistency of the IAGOS ozone and carbon monoxide measurements for the last 25 years, *Atmospheric Measurement Techniques*, 14, 3935–3951, <https://doi.org/10.5194/amt-14-3935-2021>, 2021.



- Bourgeois, I., Peischl, J., Thompson, C. R., Aikin, K. C., Campos, T., Clark, H., Commane, R., Daube, B., Diskin, G. W., Elkins, J. W., et al.: Global-scale distribution of ozone in the remote troposphere from the ATom and HIPPO airborne field missions, *Atmospheric Chemistry and Physics*, 20, 10 611–10 635, <https://doi.org/10.5194/acp-20-10611-2020>, 2020.
- 1020 Bourgeois, I., Peischl, J., Neuman, J. A., Brown, S. S., Thompson, C. R., Aikin, K. C., Allen, H. M., Angot, H., Apel, E. C., Baublitz, C. B., et al.: Large contribution of biomass burning emissions to ozone throughout the global remote troposphere, *Proceedings of the National Academy of Sciences*, 118, e2109628 118, <https://doi.org/10.1073/pnas.2109628118>, 2021.
- Boynard, A., Hurtmans, D., Koukouli, M. E., Goutail, F., Bureau, J., Safieddine, S., Lerot, C., Hadji-Lazaro, J., Wespes, C., Pommereau, J.-P., et al.: Seven years of IASI ozone retrievals from FORLI: validation with independent total column and vertical profile measurements, *Atmospheric Measurement Techniques*, 9, 4327–4353, <https://doi.org/10.5194/amt-9-4327-2016>, 2016.
- 1025 Boynard, A., Hurtmans, D., Garane, K., Goutail, F., Hadji-Lazaro, J., Koukouli, M. E., Wespes, C., Vigouroux, C., Keppens, A., Pommereau, J.-P., et al.: Validation of the IASI FORLI/EUMETSAT ozone products using satellite (GOME-2), ground-based (Brewer–Dobson, SAOZ, FTIR) and ozonesonde measurements, *Atmospheric Measurement Techniques*, 11, 5125–5152, <https://doi.org/10.5194/amt-11-5125-2018>, 2018.
- 1030 Buchholz, R. R., Worden, H. M., Park, M., Francis, G., Deeter, M. N., Edwards, D. P., Emmons, L. K., Gaubert, B., Gille, J., Martínez-Alonso, S., et al.: Air pollution trends measured from Terra: CO and AOD over industrial, fire-prone, and background regions, *Remote Sensing of Environment*, 256, 112 275, <https://doi.org/10.1016/j.rse.2020.112275>, 2021.
- Chatfield, R. B., Vastano, J. A., Singh, H., and Sachse, G.: A general model of how fire emissions and chemistry produce African/oceanic plumes (O<sub>3</sub>, CO, PAN, smoke) in TRACE A, *Journal of Geophysical Research: Atmospheres*, 101, 24 279–24 306, 1996.
- 1035 Clerbaux, C., Boynard, A., Clarisse, L., George, M., Hadji-Lazaro, J., Herbin, H., Hurtmans, D., Pommier, M., Razavi, A., Turquety, S., et al.: Monitoring of atmospheric composition using the thermal infrared IASI/MetOp sounder, *Atmospheric Chemistry and Physics*, 9, 6041–6054, <https://doi.org/10.5194/acp-9-6041-2009>, 2009.
- Cohen, Y., Petetin, H., Thouret, V., Marécal, V., Josse, B., Clark, H., Sauvage, B., Fontaine, A., Athier, G., Blot, R., et al.: Climatology and long-term evolution of ozone and carbon monoxide in the upper troposphere–lower stratosphere (UTLS) at northern midlatitudes, as seen by IAGOS from 1995 to 2013, *Atmospheric Chemistry and Physics*, 18, 5415–5453, <https://doi.org/10.5194/acp-18-5415-2018>, 2018.
- 1040 Cros, B., Delon, C., Affre, C., Marion, T., Druilhet, A., Perros, P., and Lopez, A.: Sources and sinks of ozone in savanna and forest areas during EXPRESSO: Airborne turbulent flux measurements, *Journal of Geophysical Research: Atmospheres*, 105, 29 347–29 358, <https://doi.org/10.1029/2000JD900451>, 2000.
- Curtis, L., Rea, W., Smith-Willis, P., Fenyves, E., and Pan, Y.: Adverse health effects of outdoor air pollutants, *Environment international*, 32, 815–830, <https://doi.org/10.1016/j.envint.2006.03.012>, 2006.
- 1045 Cussac, M., Marécal, V., Thouret, V., Josse, B., and Sauvage, B.: The impact of biomass burning on upper tropospheric carbon monoxide: a study using MOCAGE global model and IAGOS airborne data, *Atmospheric Chemistry and Physics*, 20, 9393–9417, <https://doi.org/10.5194/acp-20-9393-2020>, 2020.
- De Wachter, E., Barret, B., Le Flochmoën, E., Pavelin, E., Matricardi, M., Clerbaux, C., Hadji-Lazaro, J., George, M., Hurtmans, D., Coheur, P.-F., et al.: Retrieval of MetOp-A/IASI CO profiles and validation with MOZAIC data, *Atmospheric Measurement Techniques*, 5, 2843–2857, <https://doi.org/10.5194/amt-5-2843-2012>, 2012.
- 1050 Deeter, M., Martínez-Alonso, S., Andreae, M. O., and Schlager, H.: Satellite-based analysis of CO seasonal and interannual variability over the Amazon Basin, *Journal of Geophysical Research: Atmospheres*, 123, 5641–5656, <https://doi.org/10.1029/2018JD028425>, 2018.

- Dufour, G., Eremenko, M., Orphal, J., and Flaud, J.-M.: IASI observations of seasonal and day-to-day variations of tropospheric ozone over three highly populated areas of China: Beijing, Shanghai, and Hong Kong, *Atmospheric Chemistry and Physics*, 10, 3787–3801, <https://doi.org/10.5194/acp-10-3787-2010>, 2010.
- Duncan, B. N., Lamsal, L. N., Thompson, A. M., Yoshida, Y., Lu, Z., Streets, D. G., Hurwitz, M. M., and Pickering, K. E.: A space-based, high-resolution view of notable changes in urban NO<sub>x</sub> pollution around the world (2005–2014), *Journal of Geophysical Research: Atmospheres*, 121, 976–996, <https://doi.org/10.1002/2015JD024121>, 2016.
- Edwards, D., Emmons, L., Hauglustaine, D., Chu, D., Gille, J., Kaufman, Y., Pétron, G., Yurganov, L., Giglio, L., Deeter, M., et al.: Observations of carbon monoxide and aerosols from the Terra satellite: Northern Hemisphere variability, *Journal of Geophysical Research: Atmospheres*, 109, <https://doi.org/10.1029/2004JD004727>, 2004.
- Edwards, D., Emmons, L., Gille, J., Chu, A., Attié, J.-L., Giglio, L., Wood, S., Haywood, J., Deeter, M., Massie, S., et al.: Satellite-observed pollution from Southern Hemisphere biomass burning, *Journal of Geophysical Research: Atmospheres*, 111, <https://doi.org/10.1029/2005JD006655>, 2006.
- Emmons, L. K., Walters, S., Hess, P. G., Lamarque, J.-F., Pfister, G. G., Fillmore, D., Granier, C., Guenther, A., Kinnison, D., Laepple, T., et al.: Description and evaluation of the Model for Ozone and Related chemical Tracers, version 4 (MOZART-4), *Geoscientific Model Development*, 3, 43–67, <https://doi.org/10.5194/gmd-3-43-2010>, 2010.
- Eremenko, M., Dufour, G., Foret, G., Keim, C., Orphal, J., Beekmann, M., Bergametti, G., and Flaud, J.-M.: Tropospheric ozone distributions over Europe during the heat wave in July 2007 observed from infrared nadir spectra recorded by IASI, *Geophysical Research Letters*, 35, <https://doi.org/10.1029/2008GL034803>, 2008.
- Galanter, M., Levy, H., and Carmichael, G. R.: Impacts of biomass burning on tropospheric CO, NO<sub>x</sub>, and O<sub>3</sub>, *Journal of Geophysical Research: Atmospheres*, 105, 6633–6653, <https://doi.org/10.1029/1999JD901113>, 2000.
- Gaudel, A., Cooper, O. R., Ancellet, G., Barret, B., Boynard, A., Burrows, J., Clerbaux, C., Coheur, P.-F., Cuesta, J., Cuevas, E., et al.: Tropospheric Ozone Assessment Report: Present-day distribution and trends of tropospheric ozone relevant to climate and global atmospheric chemistry model evaluation, *Elementa: science of the anthropocene*, 6, <https://doi.org/10.1525/elementa.291>, 2018.
- Gaudel, A., Cooper, O. R., Chang, K.-L., Bourgeois, I., Ziemke, J. R., Strode, S. A., Oman, L. D., Sellitto, P., Nédélec, P., Blot, R., et al.: Aircraft observations since the 1990s reveal increases of tropospheric ozone at multiple locations across the Northern Hemisphere, *Science Advances*, 6, eaba8272, <https://doi.org/10.1525/elementa.291>, 2020.
- Gauss, M., Myhre, G., Pitari, G., Prather, M., Isaksen, I., Berntsen, T., Brasseur, G., Dentener, F., Derwent, R., Hauglustaine, D., et al.: Muller, JF, Plantevin, P., Pyle, JA, Rogers, HL, Stevenson, DS, Sundet, JK, van Weele, M., and Wild, O.: Radiative forcing in the 21st century due to ozone changes in the troposphere and the lower stratosphere, *J. Geophys. Res.*, 108, <https://doi.org/10.1029/2002JD002624>, 2003.
- George, M., Clerbaux, C., Hurtmans, D., Turquety, S., Coheur, P.-F., Pommier, M., Hadji-Lazaro, J., Edwards, D., Worden, H., Luo, M., et al.: Carbon monoxide distributions from the IASI/METOP mission: evaluation with other space-borne remote sensors, *Atmospheric Chemistry and Physics*, 9, 8317–8330, <https://doi.org/10.5194/acp-9-8317-2009>, 2009.
- Granier, C., Bessagnet, B., Bond, T., D’Angiola, A., Denier van der Gon, H., Frost, G. J., Heil, A., Kaiser, J. W., Kinne, S., Klimont, Z., et al.: Evolution of anthropogenic and biomass burning emissions of air pollutants at global and regional scales during the 1980–2010 period, *Climatic change*, 109, 163–190, <https://doi.org/10.1007/s10584-011-0154-1>, 2011.

- 1090 Gressent, A., Sauvage, B., Defer, E., Pätz, H. W., Thomas, K., Holle, R., Cammas, J.-P., Nédélec, P., Boulanger, D., Thouret, V., et al.: Lightning NO<sub>x</sub> influence on large-scale NO<sub>y</sub> and O<sub>3</sub> plumes observed over the northern mid-latitudes, *Tellus B: Chemical and Physical Meteorology*, 66, 25 544, <https://doi.org/10.3402/tellusb.v66.25544>, 2014.
- Gressent, A., Sauvage, B., Cariolle, D., Evans, M., Leriche, M., Mari, C., and Thouret, V.: Modeling lightning-NO<sub>x</sub> chemistry on a sub-grid scale in a global chemical transport model, *Atmospheric Chemistry and Physics*, 16, 5867–5889, [https://doi.org/10.5194/acp-16-5867-](https://doi.org/10.5194/acp-16-5867-2016)  
1095 2016, 2016.
- Hedelius, J. K., Toon, G. C., Buchholz, R. R., Iraci, L. T., Podolske, J. R., Roehl, C. M., Wennberg, P. O., Worden, H. M., and Wunch, D.: Regional and urban column CO trends and anomalies as observed by MOPITT over 16 years, *Journal of Geophysical Research: Atmospheres*, 126, e2020JD033 967, <https://doi.org/10.1029/2020JD033967>, 2021.
- Heue, K.-P., Coldewey-Egbers, M., Delcloo, A., Lerot, C., Loyola, D., Valks, P., and Van Roozendaal, M.: Trends of tropical tropospheric ozone from 20 years of European satellite measurements and perspectives for the Sentinel-5 Precursor, *Atmospheric Measurement Techniques*, 9, 5037–5051, <https://doi.org/10.5194/amt-9-5037-2016>, 2016.
- Hickman, J. E., Andela, N., Dammers, E., Clarisse, L., Coheur, P.-F., Van Damme, M., Di Vittorio, C. A., Ossohou, M., Bauer, S. E., et al.: Changes in biomass burning, wetland extent, or agriculture drive atmospheric NH<sub>3</sub> trends in select African regions, *Atmospheric Chemistry and Physics*, 21, 16 277–16 291, <https://doi.org/10.5194/acp-21-16277-2021>, 2021.
- 1105 IPCC: Climate change 2021: The physical science basis, Tech. rep., <http://www.ipcc.ch/report/ar6/wg1/>, 2021.
- Jacob, D. J., Heikes, E., Fan, S.-M., Logan, J. A., Mauzerall, D., Bradshaw, J., Singh, H., Gregory, G., Talbot, R., Blake, D., et al.: Origin of ozone and NO<sub>x</sub> in the tropical troposphere: A photochemical analysis of aircraft observations over the South Atlantic basin, *Journal of Geophysical Research: Atmospheres*, 101, 24 235–24 250, <https://doi.org/10.1029/96JD00336>, 1996.
- Jaeglé, L., Martin, R., Chance, K., Steinberger, L., Kurosu, T., Jacob, D. J., Modi, A., Yoboué, V., Sigha-Nkamdjou, L., and Galy-Lacaux, C.: Satellite mapping of rain-induced nitric oxide emissions from soils, *Journal of Geophysical Research: Atmospheres*, 109, <https://doi.org/10.1029/2004JD004787>, 2004.
- 1110 Jerrett, M., Burnett, R. T., Pope III, C. A., Ito, K., Thurston, G., Krewski, D., Shi, Y., Calle, E., and Thun, M.: Long-term ozone exposure and mortality, *New England Journal of Medicine*, 360, 1085–1095, <https://doi.org/10.1056/NEJMoa0803894>, 2009.
- Jia, J., Ladstätter-Weissenmayer, A., Hou, X., Rozanov, A., and Burrows, J. P.: Tropospheric ozone maxima observed over the Arabian Sea during the pre-monsoon, *Atmospheric Chemistry and Physics*, 17, 4915–4930, <https://doi.org/10.5194/acp-17-4915-2017>, 2017.
- 1115 Kaiser, J., Heil, A., Andreae, M., Benedetti, A., Chubarova, N., Jones, L., Morcrette, J.-J., Razinger, M., Schultz, M., Suttie, M., et al.: Biomass burning emissions estimated with a global fire assimilation system based on observed fire radiative power, *Biogeosciences*, 9, 527–554, <https://doi.org/10.5194/bg-9-527-2012>, 2012.
- Kalmus, P., Ao, C. O., Wang, K.-N., Manzi, M. P., and Teixeira, J.: A high-resolution planetary boundary layer height seasonal climatology from GNSS radio occultations, *Remote Sensing of Environment*, 276, 113 037, <https://doi.org/10.1016/j.rse.2022.113037>, 2022.
- 1120 Krotkov, N. A., McLinden, C. A., Li, C., Lamsal, L. N., Celarier, E. A., Marchenko, S. V., Swartz, W. H., Bucsela, E. J., Joiner, J., Duncan, B. N., et al.: Aura OMI observations of regional SO<sub>2</sub> and NO<sub>2</sub> pollution changes from 2005 to 2015, *Atmospheric Chemistry and Physics*, 16, 4605–4629, <https://doi.org/10.5194/acp-16-4605-2016>, 2016.
- Kumar, R., Naja, M., Pfister, G., Barth, M., Wiedinmyer, C., and Brasseur, G.: Simulations over South Asia using the Weather Research and Forecasting model with Chemistry (WRF-Chem): chemistry evaluation and initial results, *Geoscientific Model Development*, 5, 619–648, <https://doi.org/10.5194/gmd-5-619-2012>, 2012.
- 1125

- Lamarque, J.-F., Bond, T. C., Eyring, V., Granier, C., Heil, A., Klimont, Z., Lee, D., Liousse, C., Mieville, A., Owen, B., et al.: Historical (1850–2000) gridded anthropogenic and biomass burning emissions of reactive gases and aerosols: methodology and application, *Atmospheric Chemistry and Physics*, 10, 7017–7039, <https://doi.org/doi.org/10.5194/acp-10-7017-2010>, 2010.
- 1130 Lannuque, V., Sauvage, B., Barret, B., Clark, H., Athier, G., Boulanger, D., Cammas, J.-P., Cousin, J.-M., Fontaine, A., Le Flochmoën, E., et al.: Origins and characterization of CO and O<sub>3</sub> in the African upper troposphere, *Atmospheric chemistry and physics*, 21, 14535–14555, <https://doi.org/10.5194/acp-21-14535-2021>, 2021.
- Lawrence, M. and Lelieveld, J.: Atmospheric pollutant outflow from southern Asia: a review, *Atmospheric Chemistry and Physics*, 10, 11017–11096, <https://doi.org/10.5194/acp-10-11017-2010>, 2010.
- 1135 Lelieveld, J., Hoor, P., Jöckel, P., Pozzer, A., Hadjinicolaou, P., Cammas, J.-P., and Beirle, S.: Severe ozone air pollution in the Persian Gulf region, *Atmospheric Chemistry and Physics*, 9, 1393–1406, <https://doi.org/10.5194/acp-9-1393-2009>, 2009.
- Lelieveld, J., Gromov, S., Pozzer, A., and Taraborrelli, D.: Global tropospheric hydroxyl distribution, budget and reactivity, *Atmospheric Chemistry and Physics*, 16, 12477–12493, <https://doi.org/10.5194/acp-16-12477-2016>, 2016.
- Lelieveld, J. o., Crutzen, P., Ramanathan, V., Andreae, M., Brenninkmeijer, C., Campos, T., Cass, G., Dickerson, R., Fischer, H.,  
 1140 De Gouw, J., et al.: The Indian Ocean experiment: widespread air pollution from South and Southeast Asia, *Science*, 291, 1031–1036, <https://doi.org/10.1126/science.1057103>, 2001.
- Li, Y., Lau, A. K., Fung, J. C., Zheng, J., and Liu, S.: Importance of NO<sub>x</sub> control for peak ozone reduction in the Pearl River Delta region, *Journal of Geophysical Research: Atmospheres*, 118, 9428–9443, <https://doi.org/10.1002/jgrd.50659>, 2013.
- Liousse, C., Assamoi, E., Criqui, P., Granier, C., and Rosset, R.: Explosive growth in African combustion emissions from 2005 to 2030,  
 1145 *Environmental Research Letters*, 9, 035003, <https://doi.org/10.1088/1748-9326/9/3/035003>, 2014.
- Liu, J., Logan, J. A., Jones, D., Livesey, N., Megretskaia, I., Carouge, C., and Nedelec, P.: Analysis of CO in the tropical troposphere using Aura satellite data and the GEOS-Chem model: insights into transport characteristics of the GEOS meteorological products, *Atmospheric Chemistry and Physics*, 10, 12207–12232, <https://doi.org/10.5194/acp-10-12207-2010>, 2010.
- Livesey, N., Logan, J., Santee, M., Waters, J., Doherty, R., Read, W., Froidevaux, L., and Jiang, J.: Interrelated variations of O<sub>3</sub>, CO and  
 1150 deep convection in the tropical/subtropical upper troposphere observed by the Aura Microwave Limb Sounder (MLS) during 2004–2011, *Atmospheric Chemistry and Physics*, 13, 579–598, <https://doi.org/10.5194/acp-13-579-2013>, 2013.
- Logan, J. A.: An analysis of ozonesonde data for the troposphere: Recommendations for testing 3-D models and development of a gridded climatology for tropospheric ozone, *Journal of Geophysical Research: Atmospheres*, 104, 16115–16149, <https://doi.org/10.1029/1998JD100096>, 1999.
- 1155 Logan, J. A., Prather, M. J., Wofsy, S. C., and McElroy, M. B.: Tropospheric chemistry: A global perspective, *Journal of Geophysical Research: Oceans*, 86, 7210–7254, <https://doi.org/10.1029/JC086iC08p07210>, 1981.
- Lu, X., Zhang, L., Zhao, Y., Jacob, D. J., Hu, Y., Hu, L., Gao, M., Liu, X., Petropavlovskikh, I., McClure-Begley, A., et al.: Surface and tropospheric ozone trends in the Southern Hemisphere since 1990: possible linkages to poleward expansion of the Hadley circulation, *Science Bulletin*, 64, 400–409, <https://doi.org/10.1016/j.scib.2018.12.021>, 2019.
- 1160 Marais, E. A. and Wiedinmyer, C.: Air quality impact of diffuse and inefficient combustion emissions in Africa (DICE-Africa), *Environmental science & technology*, 50, 10739–10745, <https://doi.org/10.1021/acs.est.6b02602>, 2016.
- Marengo, A., Thouret, V., Nédélec, P., Smit, H., Helten, M., Kley, D., Karcher, F., Simon, P., Law, K., Pyle, J., et al.: Measurement of ozone and water vapor by Airbus in-service aircraft: The MOZAIC airborne program, An overview, *Journal of Geophysical Research: Atmospheres*, 103, 25631–25642, <https://doi.org/10.1029/98JD00977>, 1998.

- 1165 Mari, C., Jacob, D. J., and Bechtold, P.: Transport and scavenging of soluble gases in a deep convective cloud, *Journal of Geophysical Research: Atmospheres*, 105, 22 255–22 267, <https://doi.org/10.1029/2000JD900211>, 2000.
- Mari, C., Cailley, G., Corre, L., Saunois, M., Attié, J., Thouret, V., and Stohl, A.: Tracing biomass burning plumes from the Southern Hemisphere during the AMMA 2006 wet season experiment, *Atmospheric Chemistry and Physics*, 8, 3951–3961, <https://doi.org/10.5194/acp-8-3951-2008>, 2008.
- 1170 Martin, S. T., Artaxo, P., Machado, L., Manzi, A. O., Souza, R. d., Schumacher, C., Wang, J., Biscaro, T., Brito, J., Calheiros, A., et al.: The Green Ocean Amazon experiment (GoAmazon2014/5) observes pollution affecting gases, aerosols, clouds, and rainfall over the rain forest, *Bulletin of the American Meteorological Society*, 98, 981–997, <https://doi.org/10.1175/BAMS-D-15-00221.1>, 2017.
- McDuffie, E. E., Smith, S. J., O'Rourke, P., Tibrewal, K., Venkataraman, C., Marais, E. A., Zheng, B., Crippa, M., Brauer, M., and Martin, R. V.: A global anthropogenic emission inventory of atmospheric pollutants from sector-and fuel-specific sources (1970–2017): an application of the Community Emissions Data System (CEDS), *Earth System Science Data*, 12, 3413–3442, <https://doi.org/10.5194/essd-12-3413-2020>, 2020.
- 1175 Monks, P. S.: Gas-phase radical chemistry in the troposphere, *Chemical Society Reviews*, 34, 376–395, <https://doi.org/10.1039/B307982C>, 2005.
- Monks, P. S., Archibald, A., Colette, A., Cooper, O., Coyle, M., Derwent, R., Fowler, D., Granier, C., Law, K. S., Mills, G., et al.: Tropospheric ozone and its precursors from the urban to the global scale from air quality to short-lived climate forcer, *Atmospheric Chemistry and Physics*, 15, 8889–8973, <https://doi.org/10.5194/acp-15-8889-2015>, 2015.
- 1180 Myhre, G., Samset, B. H., Schulz, M., Balkanski, Y., Bauer, S., Bernsten, T. K., Bian, H., Bellouin, N., Chin, M., Diehl, T., et al.: Radiative forcing of the direct aerosol effect from AeroCom Phase II simulations, *Atmospheric Chemistry and Physics*, 13, 1853–1877, <https://doi.org/10.5194/acp-13-1853-2013>, 2013.
- 1185 Naus, S., Domingues, L. G., Krol, M., Luijkx, I. T., Gatti, L. V., Miller, J. B., Gloor, E., Basu, S., Correia, C., Koren, G., et al.: Sixteen years of MOPITT satellite data strongly constrain Amazon CO fire emissions, *European Geoscience Union (EGU) General Assembly 2022*, pp. 1–25, <https://doi.org/10.5194/egusphere-2022-450>, 2022.
- Nedelec, P., Cammas, J.-P., Thouret, V., Athier, G., Cousin, J.-M., Legrand, C., Abonnel, C., Lecoecur, F., Cayez, G., and Marizy, C.: An improved infrared carbon monoxide analyser for routine measurements aboard commercial Airbus aircraft: technical validation and first scientific results of the MOZAIC III programme, *Atmospheric Chemistry and Physics*, 3, 1551–1564, <https://doi.org/10.5194/acp-3-1551-2003>, 2003.
- 1190 Nédélec, P., Blot, R., Boulanger, D., Athier, G., Cousin, J.-M., Gautron, B., Petzold, A., Volz-Thomas, A., and Thouret, V.: Instrumentation on commercial aircraft for monitoring the atmospheric composition on a global scale: the IAGOS system, technical overview of ozone and carbon monoxide measurements, *Tellus B: Chemical and Physical Meteorology*, 67, 27 791, <https://doi.org/10.3402/tellusb.v67.27791>, 2015.
- 1195 Pandey, A., Sadavarte, P., Rao, A. B., and Venkataraman, C.: Trends in multi-pollutant emissions from a technology-linked inventory for India: II. Residential, agricultural and informal industry sectors, *Atmospheric environment*, 99, 341–352, <https://doi.org/10.1016/j.atmosenv.2014.09.080>, 2014.
- 1200 Park, M., Randel, W. J., Gettelman, A., Massie, S. T., and Jiang, J. H.: Transport above the Asian summer monsoon anticyclone inferred from Aura Microwave Limb Sounder tracers, *Journal of Geophysical Research: Atmospheres*, 112, <https://doi.org/10.1029/2006JD008294>, 2007.

- Park, M., Randel, W. J., Emmons, L. K., Bernath, P. F., Walker, K. A., and Boone, C. D.: Chemical isolation in the Asian monsoon anticyclone observed in Atmospheric Chemistry Experiment (ACE-FTS) data, *Atmospheric Chemistry and Physics*, 8, 757–764, <https://doi.org/10.5194/acp-8-757-2008>, 2008.
- 1205 Petetin, H., Thouret, V., Athier, G., Blot, R., Boulanger, D., Cousin, J.-M., Gaudel, A., Nédélec, P., and Cooper, O.: Diurnal cycle of ozone throughout the troposphere over Frankfurt as measured by MOZAIC-IAGOS commercial aircraft Diurnal cycle of ozone throughout the troposphere, *Elementa: Science of the Anthropocene*, 4, <https://doi.org/10.12952/journal.elementa.000129>, 2016.
- Petetin, H., Jeoffrion, M., Sauvage, B., Athier, G., Blot, R., Boulanger, D., Clark, H., Cousin, J.-M., Gheusi, F., Nedelec, P., et al.: Representativeness of the IAGOS airborne measurements in the lower troposphere, *Elementa: Science of the Anthropocene*, 6, <https://doi.org/10.1525/elementa.280>, 2018a.
- 1210 Petetin, H., Sauvage, B., Parrington, M., Clark, H., Fontaine, A., Athier, G., Blot, R., Boulanger, D., Cousin, J.-M., Nédélec, P., et al.: The role of biomass burning as derived from the tropospheric CO vertical profiles measured by IAGOS aircraft in 2002–2017, *Atmospheric Chemistry and Physics*, 18, 17 277–17 306, <https://doi.org/10.5194/acp-18-17277-2018>, 2018b.
- Petzold, A., Thouret, V., Gerbig, C., Zahn, A., Brenninkmeijer, C. A., Gallagher, M., Hermann, M., Pontaud, M., Ziereis, H., Boulanger, D., et al.: Global-scale atmosphere monitoring by in-service aircraft—current achievements and future prospects of the European Research Infrastructure IAGOS, *Tellus B: Chemical and Physical Meteorology*, 67, 28 452, <https://doi.org/10.3402/tellusb.v67.28452>, 2015.
- 1215 Pickering, K. E., Thompson, A. M., Tao, W.-K., Rood, R. B., McNamara, D. P., and Molod, A. M.: Vertical transport by convective clouds: Comparisons of three modeling approaches, *Geophysical research letters*, 22, 1089–1092, <https://doi.org/10.1029/95GL00889>, 1995.
- Reeves, C., Formenti, P., Afif, C., Ancellet, G., Attié, J.-L., Bechara, J., Borbon, A., Cairo, F., Coe, H., Crumeyrolle, S., et al.: Chemical and aerosol characterisation of the troposphere over West Africa during the monsoon period as part of AMMA, *Atmospheric Chemistry and Physics*, 10, 7575–7601, <https://doi.org/10.5194/acp-10-7575-2010>, 2010.
- 1220 Sadavarte, P. and Venkataraman, C.: Trends in multi-pollutant emissions from a technology-linked inventory for India: I. Industry and transport sectors, *Atmospheric environment*, 99, 353–364, <https://doi.org/10.1016/j.atmosenv.2014.09.081>, 2014.
- Safieddine, S., Boynard, A., Coheur, P.-F., Hurtmans, D., Pfister, G., Quennehen, B., Thomas, J. L., Raut, J.-C., Law, K. S., Klimont, Z., et al.: Summertime tropospheric ozone assessment over the Mediterranean region using the thermal infrared IASI/MetOp sounder and the WRF-Chem model, *Atmospheric chemistry and physics*, 14, 10 119–10 131, <https://doi.org/10.5194/acp-14-10119-2014>, 2014.
- 1225 Safieddine, S., Boynard, A., Hao, N., Huang, F., Wang, L., Ji, D., Barret, B., Ghude, S. D., Coheur, P.-F., Hurtmans, D., et al.: Tropospheric ozone variability during the East Asian summer monsoon as observed by satellite (IASI), aircraft (MOZAIC) and ground stations, *Atmospheric Chemistry and Physics*, 16, 10 489–10 500, <https://doi.org/10.5194/acp-16-10489-2016>, 2016.
- 1230 Sahu, L., Sheel, V., Kajino, M., Gunthe, S. S., Thouret, V., Nedelec, P., and Smit, H. G.: Characteristics of tropospheric ozone variability over an urban site in Southeast Asia: A study based on MOZAIC and MOZART vertical profiles, *Journal of Geophysical Research: Atmospheres*, 118, 8729–8747, <https://doi.org/10.1002/jgrd.50662>, 2013.
- Sahu, L., Sheel, V., Kajino, M., Deushi, M., Gunthe, S. S., Sinha, P., Sauvage, B., Thouret, V., and Smit, H. G.: Seasonal and interannual variability of tropospheric ozone over an urban site in India: A study based on MOZAIC and CCM vertical profiles over Hyderabad, *Journal of Geophysical Research: Atmospheres*, 119, 3615–3641, <https://doi.org/10.1002/2013JD021215>, 2014.
- 1235 Saunois, M., Reeves, C., Mari, C., Murphy, J., Stewart, D. J., Mills, G., Oram, D., and Purvis, R.: Factors controlling the distribution of ozone in the West African lower troposphere during the AMMA (African Monsoon Multidisciplinary Analysis) wet season campaign, *Atmospheric Chemistry and Physics*, 9, 6135–6155, <https://doi.org/10.5194/acp-9-6135-2009>, 2009.

- 1240 Sauvage, B., Thouret, V., Cammas, J.-P., Gheusi, F., Athier, G., and Nédélec, P.: Tropospheric ozone over Equatorial Africa: regional aspects from the MOZAIC data, *Atmospheric Chemistry and Physics*, 5, 311–335, <https://doi.org/10.5194/acp-5-311-2005>, 2005.
- Sauvage, B., Thouret, V., Thompson, A., Witte, J., Cammas, J.-P., Nédélec, P., and Athier, G.: Enhanced view of the “tropical Atlantic ozone paradox” and “zonal wave one” from the in situ MOZAIC and SHADOZ data, *Journal of Geophysical Research: Atmospheres*, 111, <https://doi.org/10.1029/2005JD006241>, 2006.
- 1245 Sauvage, B., Gheusi, F., Thouret, V., Cammas, J.-P., Duron, J., Escobar, J., Mari, C., Mascart, P., and Pont, V.: Medium-range mid-tropospheric transport of ozone and precursors over Africa: two numerical case studies in dry and wet seasons, *Atmospheric Chemistry and Physics*, 7, 5357–5370, <https://doi.org/10.5194/acp-7-5357-2007>, 2007a.
- Sauvage, B., Martin, R., Van Donkelaar, A., Liu, X., Chance, K., Jaeglé, L., Palmer, P., Wu, S., and Fu, T.-M.: Remote sensed and in situ constraints on processes affecting tropical tropospheric ozone, *Atmospheric Chemistry and Physics*, 7, 815–838, <https://doi.org/10.5194/acp-7-815-2007>, 2007b.
- 1250 Sauvage, B., Martin, R. V., Van Donkelaar, A., and Ziemke, J.: Quantification of the factors controlling tropical tropospheric ozone and the South Atlantic maximum, *Journal of Geophysical Research: Atmospheres*, 112, <https://doi.org/10.1029/2006JD008008>, 2007c.
- Sauvage, B., Thouret, V., Cammas, J.-P., Brioude, J., Nedelec, P., and Mari, C.: Meridional ozone gradients in the African upper troposphere, *Geophysical Research Letters*, 34, <https://doi.org/10.1029/2006GL028542>, 2007d.
- 1255 Sauvage, B., Fontaine, A., Eckhardt, S., Auby, A., Boulanger, D., Petetin, H., Paugam, R., Athier, G., Cousin, J.-M., Darras, S., et al.: Source attribution using FLEXPART and carbon monoxide emission inventories: SOFT-IO version 1.0, *Atmospheric Chemistry and Physics*, 17, 15 271–15 292, <https://doi.org/10.5194/acp-17-15271-2017>, 2017.
- Sheel, V., Sahu, L., Kajino, M., Deushi, M., Stein, O., and Nedelec, P.: Seasonal and interannual variability of carbon monoxide based on MOZAIC observations, MACC reanalysis, and model simulations over an urban site in India, *Journal of Geophysical Research: Atmospheres*, 119, 9123–9141, <https://doi.org/10.1002/2013JD021425>, 2014.
- 1260 Singh, H., Herlth, D., Kolyer, R., Chatfield, R., Viezee, W., Salas, L., Chen, Y., Bradshaw, J., Sandholm, S., Talbot, R., et al.: Impact of biomass burning emissions on the composition of the South Atlantic troposphere: Reactive nitrogen and ozone, *Journal of Geophysical Research: Atmospheres*, 101, 24 203–24 219, <https://doi.org/10.1029/96JD01018>, 1996.
- Stein, O., Schultz, M. G., Bouarar, I., Clark, H., Huijnen, V., Gaudel, A., George, M., and Clerbaux, C.: On the wintertime low bias of Northern Hemisphere carbon monoxide found in global model simulations, *Atmospheric chemistry and physics*, 14, 9295–9316, <https://doi.org/10.5194/acp-14-9295-2014>, 2014.
- 1265 Stevenson, D., Young, P., Naik, V., Lamarque, J.-F., Shindell, D. T., Voulgarakis, A., Skeie, R. B., Dalsoren, S. B., Myhre, G., Berntsen, T. K., et al.: Tropospheric ozone changes, radiative forcing and attribution to emissions in the Atmospheric Chemistry and Climate Model Intercomparison Project (ACCMIP), *Atmospheric Chemistry and Physics*, 13, 3063–3085, <https://doi.org/10.5194/acp-13-3063-2013>, 2013.
- 1270 Stohl, A., Bonasoni, P., Cristofanelli, P., Collins, W., Feichter, J., Frank, A., Forster, C., Gerasopoulos, E., Gäggeler, H., James, P., et al.: Stratosphere-troposphere exchange: A review, and what we have learned from STACCATO, *Journal of Geophysical Research: Atmospheres*, 108, <https://doi.org/10.1029/2002JD002490>, 2003.
- Tang, Q., Prather, M., and Hsu, J.: Stratosphere-troposphere exchange ozone flux related to deep convection, *Geophysical Research Letters*, 38, <https://doi.org/10.1029/2010GL046039>, 2011.

- 1275 Tarasick, D., Carey-Smith, T., Hocking, W., Moeini, O., He, H., Liu, J., Osman, M., Thompson, A., Johnson, B., Oltmans, S., et al.: Quantifying stratosphere-troposphere transport of ozone using balloon-borne ozonesondes, radar windprofilers and trajectory models, *Atmospheric Environment*, 198, 496–509, <https://doi.org/10.1016/j.atmosenv.2018.10.040>, 2019.
- Thompson, A. M., Witte, J. C., Hudson, R. D., Guo, H., Herman, J. R., and Fujiwara, M.: Tropical tropospheric ozone and biomass burning, *Science*, 291, 2128–2132, <https://doi.org/10.1126/science.291.5511.2128>, 2001.
- 1280 Thompson, A. M., Witte, J. C., McPeters, R. D., Oltmans, S. J., Schmidlin, F. J., Logan, J. A., Fujiwara, M., Kirchhoff, V. W., Posny, F., Coetzee, G. J., et al.: Southern hemisphere additional Ozonesondes (SHADOZ) 1998–2000 tropical ozone climatology 1. Comparison with Total ozone mapping spectrometer (TOMS) and ground-based measurements, *Journal of Geophysical Research: Atmospheres*, 108, <https://doi.org/10.1029/2001JD000967>, 2003a.
- Thompson, A. M., Witte, J. C., Oltmans, S. J., Schmidlin, F. J., Logan, J. A., Fujiwara, M., Kirchhoff, V. W., Posny, F., Coetzee, G. J., Hoegger, B., et al.: Southern Hemisphere Additional Ozonesondes (SHADOZ) 1998–2000 tropical ozone climatology 2. Tropospheric variability and the zonal wave-one, *Journal of Geophysical Research: Atmospheres*, 108, <https://doi.org/10.1029/2002JD002241>, 2003b.
- 1285 Thompson, A. M., Stauffer, R. M., Wargan, K., Witte, J. C., Kollonige, D. E., and Ziemke, J. R.: Regional and Seasonal trends in tropical ozone from SHADOZ profiles: Reference for models and satellite products, *Journal of Geophysical Research: Atmospheres*, 126, e2021JD034691, <https://doi.org/10.1029/2021JD034691>, 2021.
- 1290 Thouret, V., Marengo, A., Logan, J. A., Nédélec, P., and Grouhel, C.: Comparisons of ozone measurements from the MOZAIC airborne program and the ozone sounding network at eight locations, *Journal of Geophysical Research: Atmospheres*, 103, 25 695–25 720, <https://doi.org/10.1029/98JD02243>, 1998.
- Thouret, V., Clark, H., Petzold, A., Nédélec, P., and Zahn, A.: IAGOS: Monitoring Atmospheric Composition for Air Quality and Climate by Passenger Aircraft, pp. 1–14, Singapore: Springer Nature Singapore, [https://doi.org/https://doi.org/10.1007/978-981-15-2527-8\\_57-1](https://doi.org/https://doi.org/10.1007/978-981-15-2527-8_57-1), 2022.
- 1295 van der A, R. J., Mijling, B., Ding, J., Koukouli, M. E., Liu, F., Li, Q., Mao, H., and Theys, N.: Cleaning up the air: effectiveness of air quality policy for SO<sub>2</sub> and NO<sub>x</sub> emissions in China, *Atmospheric Chemistry and Physics*, 17, 1775–1789, <https://doi.org/10.5194/acp-17-1775-2017>, 2017.
- van der Werf, G. R., Randerson, J. T., Giglio, L., Collatz, G. J., Kasibhatla, P. S., and Arellano Jr, A. F.: Interannual variability in global biomass burning emissions from 1997 to 2004, *Atmospheric Chemistry and Physics*, 6, 3423–3441, <https://doi.org/doi.org/10.5194/acp-6-3423-2006>, 2006.
- 1300 Van der Werf, G. R., Randerson, J. T., Giglio, L., Collatz, G., Mu, M., Kasibhatla, P. S., Morton, D. C., DeFries, R., Jin, Y. v., and van Leeuwen, T. T.: Global fire emissions and the contribution of deforestation, savanna, forest, agricultural, and peat fires (1997–2009), *Atmospheric chemistry and physics*, 10, 11 707–11 735, <https://doi.org/10.5194/acp-10-11707-2010>, 2010.
- 1305 Wang, T., Xue, L., Brimblecombe, P., Lam, Y. F., Li, L., and Zhang, L.: Ozone pollution in China: A review of concentrations, meteorological influences, chemical precursors, and effects, *Science of the Total Environment*, 575, 1582–1596, <https://doi.org/10.1016/j.scitotenv.2016.10.081>, 2017.
- Wild, O., Pochanart, P., and Akimoto, H.: Trans-Eurasian transport of ozone and its precursors, *Journal of Geophysical Research: Atmospheres*, 109, <https://doi.org/10.1029/2003JD004501>, 2004.
- 1310 Yamasoe, M. A., Sauvage, B., Thouret, V., Nédélec, P., Le Flochmoen, E., and Barret, B.: Analysis of tropospheric ozone and carbon monoxide profiles over South America based on MOZAIC/IAGOS database and model simulations, *Tellus B: Chemical and Physical Meteorology*, 67, 27 884, <https://doi.org/10.3402/tellusb.v67.27884>, 2015.



- 1315 Yarragunta, Y., Srivastava, S., Mitra, D., Le Flochmoën, E., Barret, B., Kumar, P., and Chandola, H.: Source attribution of carbon monoxide and ozone over the Indian subcontinent using MOZART-4 chemistry transport model, *Atmospheric Research*, 227, 165–177, <https://doi.org/10.1016/j.atmosres.2019.04.019>, 2019.
- Zhang, Y., Cooper, O. R., Gaudel, A., Thompson, A. M., Nédélec, P., Ogino, S.-Y., and West, J. J.: Tropospheric ozone change from 1980 to 2010 dominated by equatorward redistribution of emissions, *Nature Geoscience*, 9, 875–879, <https://doi.org/10.1038/ngeo2827>, 2016.
- Zhang, Y., West, J. J., Emmons, L. K., Flemming, J., Jonson, J. E., Lund, M. T., Sekiya, T., Sudo, K., Gaudel, A., Chang, K.-L., et al.: Contributions of world regions to the global tropospheric ozone burden change from 1980 to 2010, *Geophysical Research Letters*, 48, e2020GL089184, <https://doi.org/10.1029/2020GL089184>, 2021.
- 1320 Zheng, B., Chevallier, F., Ciais, P., Yin, Y., Deeter, M. N., Worden, H. M., Wang, Y., Zhang, Q., and He, K.: Rapid decline in carbon monoxide emissions and export from East Asia between years 2005 and 2016, *Environmental Research Letters*, 13, 044007, <https://doi.org/10.1088/1748-9326/aab2b3>, 2018a.
- Zheng, B., Chevallier, F., Ciais, P., Yin, Y., and Wang, Y.: On the role of the flaming to smoldering transition in the seasonal cycle of African 1325 fire emissions, *Geophysical Research Letters*, 45, 11–998, <https://doi.org/10.1029/2018GL079092>, 2018b.
- Zheng, B., Chevallier, F., Yin, Y., Ciais, P., Fortems-Cheiney, A., Deeter, M. N., Parker, R. J., Wang, Y., Worden, H. M., and Zhao, Y.: Global atmospheric carbon monoxide budget 2000–2017 inferred from multi-species atmospheric inversions, *Earth System Science Data*, 11, 1411–1436, <https://doi.org/10.5194/essd-11-1411-2019>, 2019.
- Ziemke, J., Chandra, S., Duncan, B., Schoeberl, M., Torres, O., Damon, M., and Bhartia, P.: Recent biomass burning in the tropics and related 1330 changes in tropospheric ozone, *Geophysical Research Letters*, 36, <https://doi.org/10.1029/2009GL039303>, 2009.
- Ziemke, J. R., Oman, L. D., Strode, S. A., Douglass, A. R., Olsen, M. A., McPeters, R. D., Bhartia, P. K., Froidevaux, L., Labow, G. J., Witte, J. C., et al.: Trends in global tropospheric ozone inferred from a composite record of TOMS/OMI/MLS/OMPS satellite measurements and the MERRA-2 GMI simulation, *Atmospheric Chemistry and Physics*, 19, 3257–3269, <https://doi.org/10.5194/acp-19-3257-2019>, 2019.